9

Interferometers

The idea of interferometric detection of GWs is in principle simple and elegant, and goes back to 1962, when it was first considered by two Russian theorists, M. Gertsenshtein and V. I. Pustovoit. Weber also considered it, and it was then pushed in the late 1960s by R. Forward, R. Weiss, R. Drever, and others. In practice, however, a large GW interferometer is an extremely complex instrument, with many degrees of freedom that must be kept under control with extraordinary accuracy. Thus, their development up to the present scale has required the building up of large collaborations, comparable in size to modern particle physics experiments, as well as more than 30 years of preparation. Following the general approach of this book, as outlined in the Preface, we will not discuss the interesting history of the development of this idea, referring the reader to the Further Reading section for reviews, and we will rather focus on the present understanding of these detectors. We will begin in Section 9.1 with the most naive setting, a simple Michelson interferometer, and we will then add up successive layers of complexity in Sections 9.2 and 9.3. Having defined the experimental set-up, we will be able to discuss the principal noise sources in Section 9.4. The existing detectors (LIGO, VIRGO, GEO600 and TAMA) are discussed in Section 9.5.1 while advanced ground-based detectors, as well as the space-borne alternative, are discussed in Section 9.5.2.

9.1 A simple Michelson interferometer

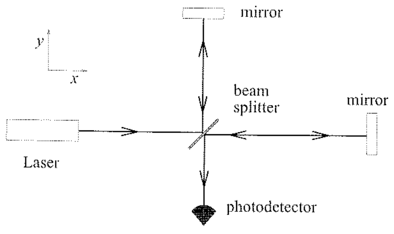

Fig. 9.1 The layout of a simple Michelson-type interferometer.

A Michelson interferometer, of the type used in the classical Michelson–Morley experiment in 1887 to show the non-existence of the ether, is an extraordinarily accurate instrument for measuring changes in the travel time of light in its arms. The simplest conceptual scheme (which is not exactly the one used historically by Michelson and Morley) is shown in Fig. 9.1. It consists of a monochromatic light source, which today is of course a laser, whose light is sent on a beam-splitter which separates the light, with equal probability amplitudes, into a beam traveling in one arms and a beam traveling in a second, orthogonal, arm. At the end of each arm we put totally reflecting mirrors. After traveling once back and forth, the two beams recombine at the beam-splitter, and part of the resulting beam goes to a photodetector, that measures its intensity (while a part goes back toward the laser). We denote by $\omega_{\rm L}$ the frequency of the laser (the subscript L distinguishes it from the frequency $\omega_{\rm gw}$ of the GWs that we want to detect), so $k_{\rm L} = \omega_{\rm L}/c$ and $\lambda_{\rm L} = 2\pi/k_{\rm L}$ are

the wavenumber and the wavelength of the laser light. It is convenient to use a complex notation for the electromagnetic field. Thus, a given spatial component of the electric field of the input laser light is written as

$$E_0 e^{-i\omega_{\rm L}t + i\mathbf{k}_{\rm L}\cdot\mathbf{x}}\,. \qquad (9.1)$$

We denote by L_x and L_y the length of the two arms, where we have oriented the x and y axis as shown in Fig. 9.1. Consider a photon that arrives at the beam-splitter, coming from the laser, at some initial time t_0.[1] The part of the electric field that goes into the x arm bounces on the mirror at a distance L_x and arrives back at the beam-splitter at a time $t = t_0 + 2L_x/c$, while the part that went through the y arm comes back at the beam-splitter at $t' = t_0 + 2L_y/c$. Thus, the beam that finally recombines at the beam-splitter at a given observation time t is the superposition of a beam that entered the beam-splitter at a time $t_0^{(x)} = t - 2L_x/c$, and then went through the x arm, and a beam that entered the beam-splitter at a *different* time $t_0^{(y)} = t - 2L_y/c$, and then went through the y arm. Setting the beam-splitter at $\mathbf{x} = 0$, the former beam has an initial phase $\exp\{-i\omega_{\rm L}t_0^{(x)}\} = \exp\{-i\omega_{\rm L}t + 2ik_{\rm L}L_x\}$, and the latter $\exp\{-i\omega_{\rm L}t_0^{(y)}\} = \exp\{-i\omega_{\rm L}t + 2ik_{\rm L}L_y\}$. The phase of the field is conserved during the free propagation, while the fields acquire overall factors from reflections and transmission at the mirrors.[2] So, the two electric fields that recombine at time t at the beam-splitter are given by

$$E_1 = -\frac{1}{2}E_0 e^{-i\omega_{\rm L}t + 2ik_{\rm L}L_x}\,. \qquad (9.2)$$

and

$$E_2 = +\frac{1}{2}E_0 e^{-i\omega_{\rm L}t + 2ik_{\rm L}L_y}\,. \qquad (9.3)$$

The total electric field is $E_{\rm out} = E_1 + E_2$. Writing $2L_x = (L_x + L_y) + (L_x - L_y)$ and $2L_x = (L_x + L_y) - (L_x - L_y)$, we see that

$$E_{\rm out} = -iE_0 e^{-i\omega_{\rm L}t + ik_{\rm L}(L_x + L_y)} \sin[k_{\rm L}(L_y - L_x)]\,, \qquad (9.4)$$

and the power measured by the photodetector is proportional to

$$|E_{\rm out}|^2 = E_0^2 \sin^2[k_{\rm L}(L_y - L_x)]\,. \qquad (9.5)$$

Therefore any variation in the length of a arm results in a corresponding variation of the power at the photodetector. We now discuss how to apply this general idea to GW detection. We saw in Section 1.3.3 that the interaction of a GW with a detector can be described in two different languages, i.e. either using the TT frame, or using the proper detector frame. It is quite instructive to understand the functioning of an interferometer in both ways, as we do in the next two subsections.

9.1.1 The interaction with GWs in the TT gauge

Recall from Section 1.3.3 that, in the TT gauge, the coordinates are marked by the position of freely falling objects so, even when a GW

---

[1] Observe that, until we discuss shot noise, in Section 9.4.1, there is really no need to introduce photons, and the whole discussion could be done purely classically, replacing the word "photon" by "wave-packet".

[2] As we will discuss in a more general setting in Section 9.2.1, the reflection off a 50–50 beam splitter can be modeled multiplying the amplitude of the incoming electric field by a factor $r = +1/\sqrt{2}$ for reflection from one side and $r = -1/\sqrt{2}$ for reflection from the other side, while the transmission multiplies it by $t = 1/\sqrt{2}$, and reflection at the perfectly reflecting mirrors at the end of each arm multiplies the amplitude by -1. Thus, overall one beam acquires a factor $(1/\sqrt{2}) \times (-1) \times (1/\sqrt{2}) = -1/2$ and the other a factor $+1/2$.

is passing, the coordinates of freely falling masses by definition do not change. Of course, the mirrors of a ground-based interferometer are not freely falling; rather, the Earth's gravity is compensated by the suspensions. However, as we already discussed in Section 1.3.3, these forces are static, compared to the frequency of the GWs that we are searching and, as far as the motion in the horizontal plane is concerned, the mirrors can be taken to be in free fall, i.e. they follow the geodesics of the time-dependent part of the gravitational field.[3]

Thus, in the TT gauge description, the coordinates of the mirrors and of the beam-splitter are not affected by the passage of the wave. We define the origin of the coordinate system as the location of the beam-splitter, while the position of the mirror which terminates the x arm defines the point with coordinates $(L_x, 0)$, and the position of the other mirror defines the point with coordinates $(0, L_y)$, and this remains true also when a GW is present.

In the TT gauge description, the physical effect of the GW is manifested in the fact that it affects the propagation of light between these fixed points. We assume for the moment that the GW has only the plus polarization, and comes from the z direction.[4] In the $z = 0$ plane of the interferometer we therefore have

$$h_+(t) = h_0 \cos \omega_{\rm gw} t\,, \tag{9.6}$$

and the space-time interval in the TT frame is given by

$$ds^2 = -c^2dt^2 + [1 + h_+(t)]dx^2 + [1 - h_+(t)]dy^2 + dz^2\,. \tag{9.7}$$

Photons travels along null geodesics, $ds^2 = 0$, so for the light in the x arm we have, to first order in h_0,

$$dx = \pm\, c dt \left[1 - \frac{1}{2} h_+(t)\right]\,, \tag{9.8}$$

where the plus sign holds for the travel from the beam-splitter to the mirror and the minus sign for the return trip. Consider a photon that leaves the beam-splitter at a time t_0. It reaches the mirror, at the fixed coordinate $x = L_x$, at a time t_1 obtained integrating eq. (9.8) with the plus sign,

$$L_x = c(t_1 - t_0) - \frac{c}{2}\int_{t_0}^{t_1} dt'\, h_+(t')\,. \tag{9.9}$$

Then the photon is reflected and reaches again the beam-splitter at a time t_2 obtained integrating eq. (9.8) with the minus sign, between $x = L_x$ and $x = 0$,

$$\int_{L_x}^{0} dx = -c\int_{t_1}^{t_2} dt' \left[1 - \frac{1}{2} h_+(t')\right]\,, \tag{9.10}$$

i.e.

$$L_x = c(t_2 - t_1) - \frac{c}{2}\int_{t_1}^{t_2} dt'\, h_+(t')\,. \tag{9.11}$$

---

[3] Of course, there will also be some non-static forces, such as those due to suspension thermal noise or, more generally, to the coupling with the environment, which will provide the background noise, and that will be discussed in Section 9.4.

[4] The response to GWs with arbitrary direction and polarization will be studied in Section 9.2.3.

Summing eqs. (9.9) and (9.11) we get

$$t_2 - t_0 = \frac{2L_x}{c} + \frac{1}{2}\int_{t_0}^{t_2} dt'\, h_+(t')\,. \tag{9.12}$$

For a given value of t_0, the time of arrival t_2 after a round trip in the x arm is therefore $t_0 + 2L_x/c$, plus a correction of order h_0. In the upper limit of the integral on the right-hand side we can replace t_2 by $t_0 + 2L_x/c$, since the integrand is already $O(h_0)$ and we are anyway neglecting terms $O(h_0^2)$, so we get

$$\begin{aligned} t_2 - t_0 &= \frac{2L_x}{c} + \frac{1}{2}\int_{t_0}^{t_0+2L_x/c} dt'\, h_0 \cos(\omega_{\rm gw} t') \\ &= \frac{2L_x}{c} + \frac{h_0}{2\omega_{\rm gw}} \left\{\sin[\omega_{\rm gw}(t_0 + 2L_x/c)] - \sin\omega_{\rm gw} t_0\right\}. \end{aligned} \tag{9.13}$$

Using the identity $\sin(\alpha + 2\beta) - \sin\alpha = 2\sin\beta\cos(\alpha+\beta)$, we can rewrite this as

$$t_2 - t_0 = \frac{2L_x}{c} + \frac{h_0 L_x}{c}\,\frac{\sin(\omega_{\rm gw} L_x/c)}{(\omega_{\rm gw} L_x/c)}\,\cos[\omega_{\rm gw}(t_0 + L_x/c)]\,. \tag{9.14}$$

Observe that the difference $t_2 - t_0$ is a function of the time t_0 at which the photon left the beam-splitter, because of the term $\cos[\omega_{\rm gw}(t_0 + L_x/c)]$. Using eq. (9.6), we can also rewrite the above result as

$$\boxed{t_2 - t_0 = \frac{2L_x}{c} + \frac{L_x}{c}\, h(t_0 + L_x/c)\,\frac{\sin(\omega_{\rm gw} L_x/c)}{(\omega_{\rm gw} L_x/c)}\,.} \tag{9.15}$$

The quantity $t_0 + L_x/c$ which appears in the argument of $h(t)$ is, to zeroth order in h_0, the value of time t_1 at which the photon touches the far mirror on the x arm. This result will be easily understood physically in the next subsection, thanks to the Newtonian intuition that we can use in the proper detector frame. The function

$${\rm sinc}\left(\frac{\omega_{\rm gw} L}{c}\right) \equiv \frac{\sin(\omega_{\rm gw} L/c)}{(\omega_{\rm gw} L/c)} \tag{9.16}$$

goes to one when $\omega_{\rm gw} L/c \to 0$. Therefore, when the period of the GW is large compared to L_x/c, the shift Δt in the travel time $t_2 - t_0$, with respect to the unperturbed value $2L_x/c$, is simply $h(t_1)L_x/c$. If $\omega_{\rm gw} L_x/c \gg 1$, Δt is suppressed. This is clearly understood physically: if $\omega_{\rm gw} L_x/c \gg 1$, during the travel time of the photon $h(t)$ changes sign many times, so it contributes sometimes positively and sometimes negatively to Δt, and these contributions partially cancel out. A plot of the function ${\rm sinc}(x)$ is shown in Fig. 9.2.

In the y arm the analysis is similar, but now the sign of $h(t)$ is reversed, as we see from eq. (9.7), so we now have

$$t_2 - t_0 = \frac{2L_y}{c} - \frac{L_y}{c}\, h(t_0 + L_y/c)\,\frac{\sin(\omega_{\rm gw} L_y/c)}{(\omega_{\rm gw} L_y/c)}\,. \tag{9.17}$$

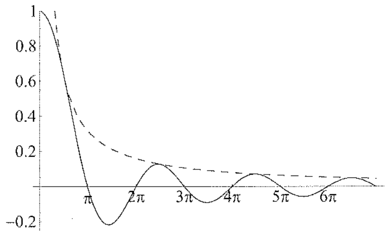

Fig. 9.2 The function $\mathrm{sinc}(x) = (1/x)\sin x$ (solid line) and, for comparison, the function $1/x$ (dashed line).

In practice we will be interested in the light that comes out of the beam-splitter at a given value of the observation time t, so it is useful to rewrite these relations holding fixed the value of the time $t_2 \equiv t$ at which we observe the light that has recombined at the beam-splitter, and computing the corresponding value of t_0. In order to come back at the beam-splitter at time t, the light that went through the x arm must have started its round-trip travel at a time $t_0^{(x)}$ obtained inverting eq. (9.15) to first order in h_0, which means that $h(t_0 + L_x/c)$ is replaced by $h(t - 2L_x/c + L_x/c) = h(t - L_x/c)$, so

$$t_0^{(x)} = t - \frac{2L_x}{c} - \frac{L_x}{c}\, h(t - L_x/c)\, \mathrm{sinc}\,(\omega_{\rm gw} L_x/c)\,, \tag{9.18}$$

and similarly the light that went through the y arm, in order to arrive back at the beam-splitter at the same time t, must have started its round-trip travel at a different time $t_0^{(y)}$ given by

$$t_0^{(y)} = t - \frac{2L_y}{c} + \frac{L_y}{c}\, h(t - L_y/c)\, \mathrm{sinc}\,(\omega_{\rm gw} L_y/c)\,. \tag{9.19}$$

Again, we use the fact that the phase of the field is conserved during the free propagation. Setting the origin of the coordinate system at the beam-splitter, and writing the electric field of the light as in eq. (9.1), we see that the light that is at the beam splitter ($\mathbf{x} = 0$) at time $t_0^{(x)}$ has a phase $\exp\{-i\omega_{\rm L} t_0^{(x)}\}$. The free propagation along the arm does not change this phase, while reflections and transmission at the mirrors give an overall factor ±1/2, see Note 2 on page 471, so[5]

$$\begin{aligned} E^{(x)}(t) &= -\frac{1}{2} E_0 e^{-i\omega_{\rm L} t_0^{(x)}} \\ &= -\frac{1}{2} E_0 e^{-i\omega_{\rm L}(t - 2L_x/c) + i\Delta\phi_x(t)}\,, \end{aligned} \tag{9.20}$$

where

$$\Delta\phi_x(t) = h_0 \frac{\omega_{\rm L} L_x}{c} \mathrm{sinc}\,(\omega_{\rm gw} L_x/c)\, \cos[\omega_{\rm gw}(t - L_x/c)]\,, \tag{9.21}$$

and similarly the field that went through the y arms, at time t has the form

$$\begin{aligned} E^{(y)}(t) &= +\frac{1}{2} E_0 e^{-i\omega_{\rm L} t_0^{(y)}} \\ &= +\frac{1}{2} E_0 e^{-i\omega_{\rm L}(t - 2L_y/c) + i\Delta\phi_y(t)}\,, \end{aligned} \tag{9.22}$$

where

$$\Delta\phi_y(t) = -h_0 \frac{\omega_{\rm L} L_y}{c} \mathrm{sinc}\,(\omega_{\rm gw} L_y/c) \cos[\omega_{\rm gw}(t - L_y/c)]\,. \tag{9.23}$$

In general, L_x and L_y will be made as close as possible,[6] in order to cancel many common noise in the two arms. Thus, in $\Delta\phi_x$ and $\Delta\phi_y$, which are already of order h_0, we simply replace L_x and L_y by $L = (L_x + L_y)/2$, while in the terms $t - 2L_x/c$ and $t - 2L_y/c$ we still take into account any small difference between L_x and L_y, writing $2L_x = 2L + (L_x - L_y)$ and $2L_y = 2L - (L_x - L_y)$. Then

$$E^{(x)}(t) = -\frac{1}{2} E_0 e^{-i\omega_{\rm L}(t - 2L/c) + i\phi_0 + i\Delta\phi_x(t)}\,, \tag{9.24}$$

$$E^{(y)}(t) = +\frac{1}{2} E_0 e^{-i\omega_{\rm L}(t - 2L/c) - i\phi_0 + i\Delta\phi_y(t)}\,, \tag{9.25}$$

where

$$\phi_0 = k_{\rm L}(L_x - L_y)\,, \tag{9.26}$$

$\Delta\phi_y = -\Delta\phi_x$, and

$$\begin{aligned} \Delta\phi_x(t) &= h_0\, k_{\rm L} L\, \mathrm{sinc}\,(\omega_{\rm gw} L/c)\, \cos[\omega_{\rm gw}(t - L/c)] \\ &\equiv |\Delta\phi_x| \cos(\omega_{\rm gw} t + \alpha)\,, \end{aligned} \tag{9.27}$$

with $\alpha = -\omega_{\rm gw} L/c$ a phase. The total phase difference induced by GWs in the Michelson interferometer is

$$\Delta\phi_{\rm Mich} \equiv \Delta\phi_x - \Delta\phi_y = 2\Delta\phi_x\,. \tag{9.28}$$

The total electric field at the output is

$$\begin{aligned} E_{\rm tot}(t) &= E^{(x)}(t) + E^{(y)}(t) \\ &= -iE_0 e^{-i\omega_{\rm L}(t - 2L/c)} \sin[\phi_0 + \Delta\phi_x(t)]\,. \end{aligned} \tag{9.29}$$

The phase ϕ_0 is a parameter that the experimenter can adjust, choosing the best working point for the interferometer, as we will discuss in Section 9.3.2, while $\Delta\phi_x(t)$ contains the effect of the GW. In the limit $\omega_{\rm gw} L/c \ll 1$, eq. (9.27) reduces to

$$\Delta\phi_x(t) \simeq h(t - L/c)\, k_L L\,. \tag{9.30}$$

Comparing with eq. (9.26) we see that, in this limit, the effect of the GW on the phase shift is formally equivalent to a change of $L_x - L_y$ given by

$$\frac{\Delta(L_x - L_y)}{L} \simeq h(t - L/c)\,. \tag{9.31}$$

The total power $P \sim |E_{\rm tot}|^2$ observed at the photodetector is modulated by the GW signal as

$$\begin{aligned} P &= P_0 \sin^2[\phi_0 + \Delta\phi_x(t)] \\ &= \frac{P_0}{2}\{1 - \cos[2\phi_0 + 2\Delta\phi_x(t)]\} \\ &= \frac{P_0}{2}\{1 - \cos[2\phi_0 + \Delta\phi_{\rm Mich}(t)]\}\,. \end{aligned} \tag{9.32}$$

Clearly, we want to have $\Delta\phi_{\rm Mich}$ as large as possible. For a GW of a given frequency $\omega_{\rm gw}$, we see from eq. (9.27) that the dependence on L is given by the factor $(\omega_{\rm L} L/c)\mathrm{sinc}\,(\omega_{\rm gw} L/c) = (\omega_{\rm L}/\omega_{\rm gw}) \sin(\omega_{\rm gw} L/c)$.

---

[5] The superscript (x) on $E^{(x)}(t)$ reminds us that this is the electric field of the light that went through the x-arm, and should not be confused with the x-component of the electric field vector. Here we are considering a given spatial component of the electric field.

[6] Except for a small asymmetry, the Schnupp asymmetry, that we will discuss in Section 9.3.2.

Thus the optimal length of the arms is given by $\omega_{\rm gw}L/c = \pi/2$, i.e. $L = \lambda_{\rm gw}/4$. In terms of $f_{\rm gw} = \omega_{\rm gw}/(2\pi)$, this gives

$$L \simeq 750\,{\rm km}\left(\frac{100\,{\rm Hz}}{f_{\rm gw}}\right). \tag{9.33}$$

For such a value of L, the time shift induced by the GW on the light has the same sign all along its round trip in a arm, so the effect adds up. For longer arms, the GW amplitude inverts its sign during the round trip, so past this moment it starts canceling the phase shift that the light already accumulated.[7] Arms of hundreds of kms are impossible to obtain in a ground-based interferometer, for practical and financial reasons. We will see in Section 9.2 how to "fold" this optimal pathlength of the light into an interferometers of manageable size.

It is useful to realize that the effect of the GW on the laser light is to generate sidebands in the light propagating in each of the two arms. Using eq. (9.27), and making use of the fact that $\Delta\phi_x$ is linear in h_0, we can expand $E^{(x)}(t)$ in eq. (9.24) to order h_0 as

$$\begin{aligned} E^{(x)}(t) &= -\frac{1}{2}E_0 e^{-i\omega_{\rm L}(t-2L/c)+i\phi_0}\left[1 + i|\Delta\phi_x|\,\cos(\omega_{\rm gw}t+\alpha)\right] \\ &= \frac{1}{2}E_0 e^{i\beta}\left[e^{-i\omega_{\rm L}t} + \frac{i}{2}|\Delta\phi_x|\,e^{i\alpha}e^{-i(\omega_{\rm L}-\omega_{\rm gw})t}\right. \\ &\qquad\left. +\frac{i}{2}|\Delta\phi_x|\,e^{-i\alpha}e^{-i(\omega_{\rm L}+\omega_{\rm gw})t}\right], \end{aligned} \tag{9.34}$$

with β an irrelevant constant phase. Thus, beside the original electromagnetic wave at a frequency $\omega_{\rm L}$ (the "carrier", in the language of radio engineering), we have two more electromagnetic waves, at the frequencies $\omega_{\rm L} \pm \omega_{\rm gw}$ (the "sidebands"). The modulus of the amplitude of the sidebands is $O(h_0)$ with respect to the carrier, and is given by $|\Delta\phi_x|/2$.

9.1.2 The interaction in the proper detector frame

It is instructive to compare the above results, obtained in the TT frame, with the description obtained using the language of the proper detector frame. Recall from Section 1.3.3 that the proper detector frame is the one implicitly used by the experimenter when he/she thinks about the apparatus. In particular, here coordinates are not marked by freely falling masses, as in the TT gauge, but rather are measured with a rigid ruler. We saw that in the proper detector frame the effect of the passage of a GW is a displacement of the test masses from their original position and, if these test masses are at a distance small compared to the reduced wavelength $\lambdabar_{\rm gw}$ of the GW, this displacement is determined by the equation of the geodesic deviation (1.95). At the same time, the space-time metric can be taken as flat, at least in a region of space small compared to the scale of variation of the gravitational wave, which is its reduced wavelength $\lambdabar_{\rm gw}$.[8]

---

[7] More precisely, for the value of L given in eq. (9.33), the time shift always keeps the same sign for a photon whose time of time of entry inside the cavity is properly synchronized with the phase of the GW. For larger values, there is at least a partial cancellation, no matter what is the relation between the phase of the GW and the time of entry of the photon.

[8] This is correct as far as the fast-varying part of the gravitational field is concerned, while the static gravitational field of the Earth is compensated by the mirror suspensions, and other effects related to the laboratory frame (Coriolis forces, etc.) are negligible because slowly varying, see the detailed discussion in Section 1.3.3.

Thus, the proper detector frame description has the advantage of being very intuitive, since in a first approximation we can use the language of flat space-time, and the interaction of the mirrors with GWs is described by the equation of the geodesic deviation, i.e. in terms of Newtonian forces, so we can use our Newtonian intuition. However it must be kept in mind that, contrary to the TT gauge description, which is exact, the proper-frame description is approximate, and is valid only if the test masses are at a distance small compared to the reduced wavelength $\lambdabar_{\rm gw}$ of the GW, see eq. (1.97). Since for a Michelson interferometer the distance between the beam-splitter and the end mirror of an arm is the arm-length L, the proper detector frame description assumes $L \ll \lambdabar_{\rm gw}$, that is,

$$\frac{\omega_{\rm gw}L}{c} \ll 1\,. \tag{9.35}$$

Thus, we cannot expect to recover the full TT gauge result (9.27), which is exact, but only its limit for small values of $\omega_{\rm gw}L/c$.

We first perform the computation in the proper detector frame to lowest-order in $\omega_{\rm gw}L/c$. In this limit the space-time metric is exactly flat, see eq. (1.86), while the effect of the GW on the test masses is given by the equation of the geodesic deviation, eq. (1.95). Thus, the situation is reversed compared to the TT gauge description. In the TT gauge, the position of the mirrors is not affected by GWs, while the propagation of light between the mirrors is affected. In the proper detector frame, the mirrors are affected by the GWs, while light propagation is not. We fix the origin of the coordinate system on the beam-splitter so, by definition, the beam-splitter does not move, and we consider as before a GW with only the plus polarization coming from the z direction, written as in eq. (9.6). The equation of the geodesic equation for the mirror on the x arm, described by coordinates (ξ_x, ξ_y), is then[9]

$$\ddot{\xi}_x = \frac{1}{2}\ddot{h}_+\xi_x\,, \tag{9.36}$$

while $\xi_y(t)$ remains zero at all times if $\xi_y(0) = \dot{\xi}_y(0) = 0$. Equation (9.36) can be solved perturbatively in h_0; to zeroth order we have $\xi_x = L_x$, so to $O(h_0)$ we get $\ddot{\xi}_x = (1/2)\ddot{h}_+L_x$, which has the solution

$$\xi_x(t) = L_x + \frac{h_0L_x}{2}\cos\omega_{\rm gw}t\,, \tag{9.37}$$

where we choose the integration constants so that the average value of ξ_x over one period of the GW is equal to L_x, and the average value of the velocity $\dot{\xi}_x$ vanishes.

Since space-time is flat, a photon that starts at the beam-splitter at time t_0, moving along the positive x axis, follows the trajectory $x(t) = c(t-t_0)$, so it reaches the mirror at a time t_1 given by $c(t_1-t_0) = \xi_x(t_1)$. This equation is easily solved for t_1, perturbatively in h_0. To zeroth order in h_0 we get the trivial result $t_1 = t_0 + (L_x/c)$. Inserting this into $\cos\omega_{\rm gw}t$ in eq. (9.37) (which is already multiplied by h_0), we get

$$c(t_1 - t_0) = L_x + \frac{h_0L_x}{2}\cos[\omega_{\rm gw}(t_0 + L_x/c)]\,. \tag{9.38}$$

---

[9] The fact that here appears the form of $h_{\mu\nu}$ in the TT gauge, even if we are working in the proper detector frame, is a consequence of the fact that the right-hand side of eq. (9.36) is really $-c^2R_{i0j0}\xi^j$, see eq. (1.93). Recall from Section 1.1 that, in linearized theory, the Riemann tensor is invariant under coordinate transformations, so we are free to compute it in the frame that we wish, and in particular we can use the form of $h_{\mu\nu}$ in the TT gauge.

The round-trip time is twice as large, so the photon gets back at the beam-splitter at a time t_2 given by

$$t_2 - t_0 = \frac{2L_x}{c} + \frac{h_0 L_x}{c}\cos[\omega_{\rm gw}(t_0 + L_x/c)]\,. \tag{9.39}$$

This coincide with the result that we got in the TT gauge, eq. (9.14), *except* that the function $\text{sinc}\,(\omega_{\rm gw}L/c) = [\sin(\omega_{\rm gw}L/c)]/[\omega_{\rm gw}L/c]$ has been replaced by one, which is the lowest-order term of its Taylor expansion. This is as expected, since the proper-frame computation just performed is valid only to lowest order in $\omega_{\rm gw}L/c$.

It is instructive to compute also the next term in the expansion in $\omega_{\rm gw}L/c$ in the proper detector frame, and verify that we correctly recover the next term in the expansion of $\text{sinc}\,(\omega_{\rm gw}L/c)$. In principle, we have two kinds of corrections. (1) Corrections to the equation of motion of the mirrors, since the geodesic equation that we have used is the first term in an expansion in $L/\lambda\!\!\!{}^-_{\rm gw} = \omega_{\rm gw}L/c$, as it is clear from the derivation leading from eq. (1.66) to eq. (1.71). (2) Correction to the propagation of the photons, since the space-time metric is no longer flat.

Actually, the former type of correction in our problem vanishes at next-to-leading order.[10] The first correction to the photon propagation can be computed using the metric (1.87). For the propagation along a trajectory with $y = z = 0$ (and therefore with $dy = dz = 0$), recalling that the Riemann tensor is antisymmetric in the first and second pair of indices, eq. (1.87) reduces to

$$ds^2 = -c^2dt^2(1 + R_{0101}x^2) + dx^2\,. \tag{9.40}$$

We can compute the Riemann tensor using the form of $h_{\mu\nu}$ in the TT gauge (compare with Note 9) which gives, for a wave with only the plus polarization,

$$\begin{aligned} R_{0101} &= -\frac{1}{2c^2}\,\ddot{h}_+ \\ &= \frac{\omega_{\rm gw}^2}{2c^2}\,h_0\cos\omega_{\rm gw}t\,, \end{aligned} \tag{9.41}$$

see eq. (1.94). Light propagation is obtained imposing $ds^2 = 0$ in eq. (9.40); then, to next-to-leading order, the position $x(t)$ of a photon propagating along the x arm is obtained integrating

$$dx = \pm c\,dt\left[1 + \frac{\omega_{\rm gw}^2}{4c^2}x^2(t)h_0\cos\omega_{\rm gw}t\right], \tag{9.42}$$

while the motion of the mirrors is still given by eq. (9.37).

Consider a photon that leaves the beam-splitter at time t_0 and propagates along the positive x direction. To lowest order in h_0 we have the trivial result $x(t) = c(t - t_0)$. Inserting this into the right-hand side of eq. (9.42) we find the solution to order h_0,

$$x(t) = c(t - t_0) + h_0\frac{c\,\omega_{\rm gw}^2}{4}\int_{t_0}^{t} dt'\,(t' - t_0)^2\cos\omega_{\rm gw}t'\,. \tag{9.43}$$

---

[10] This can be shown by observing that the geodesic equation (1.66) for a mirror moving non-relativistically is simply $\ddot{\xi}^i = -\Gamma^i_{00}(\xi)$. Expanding it to second order in ξ, with $\Gamma^i_{00}(\xi = 0) = 0$, we get

$$\ddot{\xi}^i = -\xi^j\partial_j\Gamma^i_{00} - \frac{1}{2}\xi^j\xi^k\partial_k\partial_j\Gamma^i_{00} + O(\xi^3),$$

where the derivatives of Γ^i_{00} are computed at $\xi = 0$. The first term gives the equation of motion that we already used. For a mirror along the x arm $\xi^i = (\xi_x, 0, 0)$, so the second term is proportional to $\partial_1(\partial_1\Gamma^1_{00})$. A plane wave propagating along the z direction is function only of t and z, and so its Riemann tensor, as well as $(\partial_1\Gamma^1_{00})$, is independent of x, and $\partial_1(\partial_1\Gamma^1_{00})$ vanishes.

Writing

$$\begin{aligned} \cos\omega_{\rm gw}t' &= \cos[\omega_{\rm gw}(t' - t_0) + \omega_{\rm gw}t_0] \\ &= \cos[\omega_{\rm gw}(t' - t_0)]\cos\omega_{\rm gw}t_0 - \sin[\omega_{\rm gw}(t' - t_0)]\sin\omega_{\rm gw}t_0\,, \end{aligned} \tag{9.44}$$

the integral over t' can be performed exactly. Consistently with the order to which we are working, we then expand the exact result to the first non-trivial order in $\omega_{\rm gw}(t - t_0)$ (which, in the final result, will correspond to the first non-trivial order in $\omega_{\rm gw}L/c$), and we get

$$x(t) \simeq c(t - t_0) + h_0\frac{c\,\omega_{\rm gw}^2}{12}(t - t_0)^3\cos\omega_{\rm gw}t_0\,. \tag{9.45}$$

The time t_1 at which the photon reaches the mirror is now obtained solving the equation $x(t_1) = \xi(t_1)$ iteratively in h_0. This gives

$$c(t_1 - t_0) = L_x + \frac{h_0L_x}{2}\cos[\omega_{\rm gw}(t_0 + L_x/c)] - h_0\frac{\omega_{\rm gw}^2}{12c^2}L_x^3\cos(\omega_{\rm gw}t_0)\,. \tag{9.46}$$

Observe that (writing $\epsilon \equiv \omega_{\rm gw}L_x/c$)

$$\begin{aligned} \cos[\omega_{\rm gw}(t_0 + L_x/c)] &= \cos(\omega_{\rm gw}t_0)\cos\epsilon - \sin(\omega_{\rm gw}t_0)\sin\epsilon \\ &= [1 + O(\epsilon^2)]\cos(\omega_{\rm gw}t_0) + O(\epsilon)\sin(\omega_{\rm gw}t_0)\,, \end{aligned} \tag{9.47}$$

so in the last term of eq. (9.46), which is already a factor $(\omega_{\rm gw}L_x/c)^2$ smaller than the second term, we can replace $\cos(\omega_{\rm gw}t_0)$ by $\cos[\omega_{\rm gw}(t_0 + L_x/c)]$, since the difference is of higher order in $\omega_{\rm gw}L_x/c$. Then we finally get

$$c(t_1 - t_0) = L_x + \frac{h_0L_x}{2}\cos[\omega_{\rm gw}(t_0 + L/c)]\left[1 - \frac{1}{6}\left(\frac{\omega_{\rm gw}L_x}{c}\right)^2\right]. \tag{9.48}$$

Writing similarly the equations for the round trip we find that, to this order in $\omega_{\rm gw}L_x/c$, the round-trip travel $t_2 - t_0$ is twice $t_1 - t_0$. In the last bracket we recognize the first two terms of the expansion

$$\frac{\sin x}{x} = 1 - \frac{x^2}{6} + O(x^4)\,. \tag{9.49}$$

We have therefore verified that the analysis in the proper detector frame correctly reproduces the leading and the next-to-leading terms of the TT gauge result given in eq. (9.15). It is also clear from this discussion that, while the description in the detector proper frame is more intuitive, since it allows us to think in terms of Newtonian forces acting on the mirrors, and of light propagating (in a first approximation) in the flat space-time of Newtonian physics, still the TT gauge description is much more powerful, since it allows us to get the exact closed form of the dependence on $\omega_{\rm gw}L_x/c$. In the detector proper frame the computation of still higher-order corrections becomes more and more involved and, without the hindsight from the TT gauge analysis, it would be difficult to imagine that the whole series resums to such a simple closed form.

9.2 Interferometers with Fabry–Perot cavities

We have seen in eq. (9.33) that, to measure GWs with frequencies of order of a few hundreds Hz, the optimal choice would be an arm-length L of several hundreds kms. For Earth-based interferometers this is in practice impossible (consider, among other things, that the arms of the interferometers must be enclosed in a very high vacuum system, as we will see in the Section 9.4). Taking into account technological and financial constraints, LIGO has arms of length $L = 4$ km and VIRGO of 3 km, while GEO600 has $L = 600$ m and TAMA has $L = 300$ m. The idea is therefore to "fold" the optical path of light, making it bounce back and forth many times in each arm, before recombining the two beams. A solution that was first considered is the so-called "delay line". In this case, in each arm the light beam goes back and forth between two mirrors along trajectories that do not superimpose, and which make different spots on the mirrors. However, to reach an effective path length of order 750 km out of arms of order 3–4 km we need $O(100)$ bounces. In the delay line scheme, this leads to unpractically large mirrors.[11] Thus, the solution which has been adopted in LIGO and VIRGO is that of transforming each arm into a Fabry–Perot cavity. In the next subsection we will discuss the principles of operation of a Fabry–Perot (FP) cavity, and in Section 9.2.2 we will discuss its interaction with a GW, and we will see how it improves on the simple Michelson scheme.

9.2.1 Electromagnetic fields in a FP cavity

Reflection and transmission coefficients

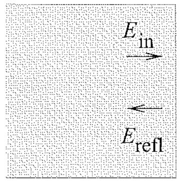

Fig. 9.3 The situation in which the incoming field comes from the denser medium.

First of all we recall from elementary electromagnetism that, at the interface between two media with different index of refraction, the relation between the incoming field $E_{\rm in}$, the reflected field $E_{\rm refl}$ and the transmitted field $E_{\rm t}$ can be written as

$$E_{\rm refl} = rE_{\rm in}\,, \qquad E_{\rm t} = tE_{\rm in}\,, \tag{9.50}$$

where r and t are called the reflection and transmission coefficients, respectively, and are in general complex numbers. We consider for the moment the transmission and reflection across a sharp boundary. At a sharp boundary there is no physical mechanism that can produce a phase shift, so in this limit r and t are real. More precisely, (r, t) are the reflection and transmission coefficients when $E_{\rm in}$ comes from the first medium, say the denser (from the left in Fig. 9.3). Similarly, we denote by r' and t' the reflection and transmission coefficients when $E_{\rm in}$ comes from the second medium, i.e. from the right in Fig. 9.4. Between these coefficients hold useful relations. In particular, since the energy associated to the electric field is proportional to $|E|^2$, and on a sharp boundary there are no losses and r, t are real, energy conservation requires

$$r^2 + t^2 = 1\,, \tag{9.51}$$

and ${r'}^2 + {t'}^2 = 1$.[12] Between (r, t) and (r', t') we have so-called reciprocity relations, which can be obtained as follows. Consider the arrangement shown in Fig. 9.5, in which the incoming electric field arrives from the left, and there is a gap of width d of a less dense medium between two layers of the more dense medium. We denote by $E_{\rm cav}$ and $E'_{\rm cav}$, respectively, the right-moving and left-moving electric fields in the gap, close to the first interface. Then, by definition of reflection and transmission coefficients, at the first interface we have the two relations

$$E_{\rm cav} = tE_{\rm in} + r'E'_{\rm cav}\,, \tag{9.52}$$

$$E_{\rm refl} = rE_{\rm in} + t'E'_{\rm cav}\,. \tag{9.53}$$

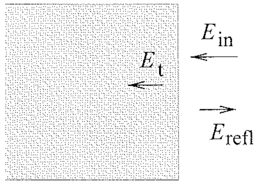

Fig. 9.4 The situation in which the incoming field comes from the rarer medium.

We now take the limit $d \to 0$. In this case $E_{\rm cav}$ and $E'_{\rm cav}$ are also the right and left-moving fields, respectively, at the second interface. Thus, we also have the relations

$$E_{\rm t} = t'E_{\rm cav}\,, \tag{9.54}$$

$$E'_{\rm cav} = r'E_{\rm cav}\,. \tag{9.55}$$

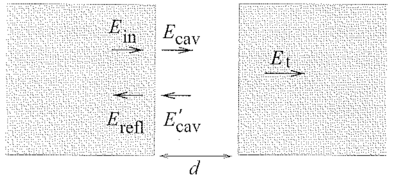

Fig. 9.5 A gap of a less dense medium between two layers of denser media.

On the other hand, if $d \to 0$, there is no gap, and we must have

$$E_{\rm t} = E_{\rm in}\,, \tag{9.56}$$

$$E_{\rm refl} = 0\,. \tag{9.57}$$

Combining the six relations (9.52)–(9.57) we find the two conditions

$$r' = -r\,, \tag{9.58}$$

$$tt' - rr' = 1\,. \tag{9.59}$$

Inserting eqs. (9.58) and (9.51) into eq. (9.59) we get $t' = t$. In conclusion, we have

$$\boxed{r' = -r\,, \qquad t' = t\,.} \tag{9.60}$$

For a perfectly reflecting mirror, reflection from the less dense to the more dense medium is associated to a factor $r' = -1$, while from the denser to the less dense medium we have $r = 1$.

Reflected, transmitted and interior field in a FP cavity

We can now apply the above results to the study of a Fabry–Perot cavity. A Fabry–Perot cavity consists of two parallel mirrors, that for the time being we assume plane and of infinite transverse extent. We consider a component $E_{\rm in}$ of the incoming electric field. Part of the incoming field is reflected and partly transmitted, see Fig. 9.6. The

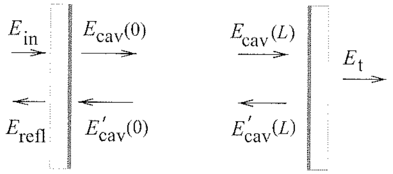

Fig. 9.6 A schematic Fabry–Perot cavity.

---

[11] Furthermore, this scheme turns out to be quite sensitive to the problem that some part of the light is scattered inside the interferometer off the nominal path, and this light interferes with the main beam.

[12] More precisely, the energy density is actually proportional to $\mathbf{E}\cdot\mathbf{D}$, where $\mathbf{D}$ is the displacement vector. If we define the coefficients r, t in terms of $\mathbf{E}$, we should then write $r^2 + t^2(n_1/n_2) = 1$. We can however simply reabsorb n into the definition of $\mathbf{E}$ to keep the equations in simpler forms such as eq. (9.51). In any case, the issue is irrelevant for a situation such as that shown in Fig. 9.6, where we are interested in the fields in the vacuum, on both sides of the mirror.

transmitted field $E_{\text{cav}}(0)$ propagates to the far mirror, where it is partly reflected and partly transmitted. The reflected part goes back to the first mirror, where again it is partly reflected and partly transmitted, and so on. The total reflected, interior and transmitted fields are therefore determined by the superposition of many beams, corresponding to the multiple bounces.

The light from the laser comes from the left in Fig. 9.6. The mirrors are set with their high-reflectivity coating on the interior of the cavity. Before reaching the high-reflectivity coating, light enters from the left face of the mirror and passes through the substrate, so in general it acquires a further complex phase shift, both from the substrate and from the coating, and can also suffer losses. A beam which enters the cavity and, after a number of round-trips, is reflected back, traverses once more this substrate, acquiring a further phase. The important point, however, is that these phase shifts are the same for all beams, independently of the number of bounces made inside the FP cavity, so they just give an overall phase factor, independent of the length L of the cavity, to the reflected (and transmitted) fields. This phase factor is compensated by the experimenter, moving the position of the mirrors until the interference pattern of the interferometer is on the desired working point (the dark fringe, as we will see), so we can simply forget about them.[13] We can therefore simply model the two mirrors of the FP cavity stating that, for the first mirror, we have real reflection and transmission coefficients r_1 and t_1 when the incoming field propagates from the interior of the mirror toward the cavity, and $r_1' = -r_1$ and $t_1' = t_1$ when it is going from the cavity toward the mirror. We then take into account the losses in the mirror writing

$$r_1^2 + t_1^2 = 1 - p_1\,, \tag{9.61}$$

where p_1 (typically of order of a few parts per million) represents the losses in the first mirror. We similarly introduce coefficients (r_2, t_2) and $(r_2' = -r_2, t_2' = t_2)$ for the second mirror, with $r_2^2 + t_2^2 = 1 - p_2$, so again a field that propagates from the cavity toward the mirror and is reflected back gets a factor $-r_2$.

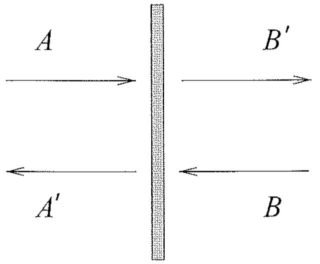

Fig. 9.7 A symmetric mirror, with a field A coming from the left and a field B incoming from the right.

Other modelizations of the mirrors are possible. In particular, one could treat the reflection and transmission from the two sides of the mirror symmetrically so that, if a field A is coming from the left, the reflected field is $A_R = z_R A$ and the transmitted field is $A_T = z_T A$, where z_R and z_T are the reflection and transmission coefficients, which now a priori can be complex because of the finite thickness of the mirror, and which satisfy $|z_R|^2 + |z_T|^2 = 1 - p$. Similarly, if a field B is coming from the right, the reflected field is $B_R = z_R B$ and the transmitted field is $B_T = z_T B$, with the same z_R, z_T. In the presence of both a field A coming from the left and a field B coming from the right, as in Fig. 9.7, we have

$$A' = z_R A + z_T B \tag{9.62}$$

$$B' = z_T A + z_R B\,. \tag{9.63}$$

Requiring the energy balance $|A'|^2 + |B'|^2 = (1-p)(|A|^2 + |B|^2)$, we get the condition Re $(z_R z_T^*) = 0$. A possible solution is $z_R = ir$, $z_T = t$, where r and t are real and satisfy $r^2 + t^2 = 1 - p$.

These different modelizations of the mirrors of a cavity of length L can however be compensated by a constant shift ΔL of some fraction of wavelength. For instance, with the modelization $r' = -r$, we will find below that a Fabry–Perot cavity resonates at $2k_{\text{L}}L = 2\pi n$, with n integer. Repeating the computation for $z_R = ir$, equal for both sides, one would rather find resonances at $2k_{\text{L}}L = 2\pi(n + 1/2)$. In practice, the experimenter tunes the position of the mirrors until he/she finds a resonance, and all that matters is the behavior around resonance, which is the same in the two cases, so the modelization chosen for the mirrors becomes irrelevant. Similarly, using $z_R = ir$ and $z_T = t$, instead of eq. (9.5) one would find $|E_{\text{out}}|^2 = E_0^2 \cos^2[k_{\text{L}}(L_y - L_x)]$, but again the experimenter simply adjusts the lengths L_x and L_y until he/she finds the desired working point, such as the dark fringe. For definiteness, we will always use the modelization leading to eq. (9.60).

We can now compute the reflected and transmitted fields, and the field inside the cavity, as follows. We choose the coordinates so that the left mirror is at $x = 0$ and the right mirror at $x = L$. From the laser we send light with an electric field of the form $E_0 \exp\{-i\omega_{\text{L}}t + ik_{\text{L}}x\}$. Let $t = t_0$ be the value of time at which a given wave-packet reaches the mirror, at $x = 0$. Thus, the corresponding electric field is simply

$$E_0 e^{-i\omega_{\text{L}} t_0}\,. \tag{9.64}$$

Part of this beam will be immediately reflected back from the mirror, with amplitude $+r_1$, giving rise to a reflected beam with field

$$E_{\text{refl}}^{(0)} = r_1 E_0 e^{-i\omega_{\text{L}} t_0}\,. \tag{9.65}$$

This field will interfere with a beam that was send toward the mirror *earlier*, which entered the cavity, was reflected back at the second mirror, and then was transmitted from the first mirror, see Fig. 9.8. In order to arrive back at the first mirror at the same time t_0, it must have entered the cavity at time $t_0 - 2L/c$. So, its initial amplitude when it entered the mirror for the first time, arriving from the laser, was $E_0 e^{-i\omega_{\text{L}}(t_0 - 2L/c)}$, that is $E_0 e^{-i\omega_{\text{L}} t_0} e^{2ik_{\text{L}}L}$. After transmission from the first mirror it gets a factor t_1, reflection at the second mirror gives a factor $-r_2$ and finally transmission from the first mirror gives again t_1. Thus, at time t_0 the total reflected field gets also a contribution

$$E_{\text{refl}}^{(1)} = \left[-t_1^2 r_2\, e^{2ik_{\text{L}}L}\right] E_0 e^{-i\omega_{\text{L}} t_0}\,. \tag{9.66}$$

This beam has a relative amplitude $-r_2 t_1^2\, e^{2ik_{\text{L}}L}$ compared to the incoming laser field given in eq. (9.64).[14] Then, we have the field that entered the cavity at time $t_0 - 4L/c$, and went twice back and forth in the cavity. It comes out at time t_0 with an amplitude

$$E_{\text{refl}}^{(2)} = \left[-r_1 r_2^2 t_1^2\, e^{4ik_{\text{L}}L}\right] E_0 e^{-i\omega_{\text{L}} t_0}\,. \tag{9.67}$$

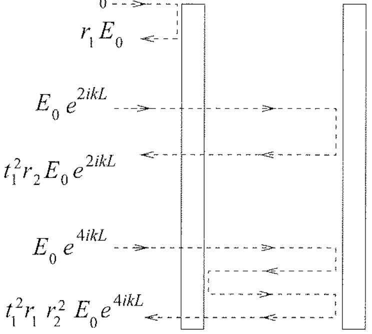

Fig. 9.8 The building up of the reflected field from the interference of the directly reflected beams and of beams that entered the cavity at earlier times and made a number of bounces inside the cavity. For clarity, the various path have been drawn as if they were spatially separated.

[13] Multiple reflections inside the substrate can be suppressed by using anti-reflection coatings, but are really eliminated only by giving to the external face of the mirror a wedge-shaped form, so after a few bounces the photon is simply lost, rather than reentering the main beam with a different phase (which would result in noise). It should however be observed that all these couplings of the phase of the light to the geometry of the optics (such as multiple reflections, phase shifts at the coatings, etc.) are channels from which noise can enter.

[14] This result is often colloquially explained stating that the field has acquired a phase $e^{2ik_{\text{L}}L}$ from the free propagation, and the factors $-r_2 t_1^2$ from its various transmissions and reflection. This is misleading. Of course, a wave does not acquire any phase factor from its free propagation. Photons in free space propagate along a trajectory $x(t) = x_0 + c(t - t_0)$, so $x(t) - ct = x_0 - ct_0$ is a constant, and the phase factor $k_{\text{L}}x - \omega_{\text{L}}t = k_{\text{L}}(x - ct)$ is also constant along the free propagation. In flat space-time, multiplicative factors and phases are acquired by the amplitude only when there is interaction with matter, i.e. at reflection and transmission from the mirrors, and in our case this gives the factor $-r_2 t_1^2$. The factor $e^{2ik_{\text{L}}L}$ relative to eq. (9.64) is there because the beam that we are considering entered the cavity *earlier*, at a time $t_0 - 2L/c$, and spent a time $2L/c$ going back and forth in the cavity. Thus, this second beam already had from the start a phase different by a factor $e^{2ik_{\text{L}}L}$, compared to the field (9.64) that arrives at time t_0 directly from the laser.

More generally, the field that entered the cavity at time $t_0 - n(2L/c)$ and performed n round trips comes out at time t_0 with an amplitude

$$E^{(n)}_{\rm refl} = \left[-r_1^{n-1} r_2^n t_1^2\, e^{2nik_{\rm L}L}\right] E_0 e^{-i\omega_{\rm L}t_0}\,. \tag{9.68}$$

The total reflected field is therefore given by

$$\begin{aligned} E_{\rm refl} &= E_0 e^{-i\omega_{\rm L}t_0}\left[r_1 - t_1^2 \sum_{n=1}^{\infty} r_1^{n-1} r_2^n e^{2nik_{\rm L}L}\right] \\ &= E_0 e^{-i\omega_{\rm L}t_0}\left[r_1 - t_1^2 r_2 e^{2ik_{\rm L}L} \sum_{m=0}^{\infty} \left(r_1 r_2 e^{2ik_{\rm L}L}\right)^m\right] \\ &= E_0 e^{-i\omega_{\rm L}t_0}\left[r_1 - t_1^2 r_2 \frac{e^{2ik_{\rm L}L}}{1 - r_1 r_2 e^{2ik_{\rm L}L}}\right], \end{aligned} \tag{9.69}$$

or, using $t_1^2 = 1 - p_1 - r_1^2$,

$$\boxed{E_{\rm refl} = E_0 e^{-i\omega_{\rm L}t_0}\, \frac{r_1 - r_2(1-p_1)e^{2ik_{\rm L}L}}{1 - r_1 r_2 e^{2ik_{\rm L}L}}\,.} \tag{9.70}$$

The transmitted field is computed similarly,

$$\begin{aligned} E_{\rm t} &= E_0 e^{-i\omega_{\rm L}t_0}\; t_1 t_2 \sum_{n=0}^{\infty} (r_1 r_2)^n e^{ik_{\rm L}L(2n+1)} \\ &= E_0 e^{-i\omega_{\rm L}t_0}\; \frac{t_1 t_2 e^{ik_{\rm L}L}}{1 - r_1 r_2 e^{2ik_{\rm L}L}}\,. \end{aligned} \tag{9.71}$$

The field inside the cavity, at the left mirror ($x = 0$), again at time t_0, is

$$\begin{aligned} E_{\rm cav}(0) &= E_0 e^{-i\omega_{\rm L}t_0}\; t_1 \sum_{n=0}^{\infty} (r_1 r_2)^n e^{2nik_{\rm L}L} \\ &= E_0 e^{-i\omega_{\rm L}t_0}\; \frac{t_1}{1 - r_1 r_2 e^{2ik_{\rm L}L}}\,, \end{aligned} \tag{9.72}$$

and for the field inside the cavity, at the other mirror, at time t_0, we have $E_{\rm cav}(L) = e^{ik_{\rm L}L} E_{\rm cav}(0)$. The same results can been obtained also in the following way, which is maybe less vivid physically, but will be easier to generalize to the situation in which GWs are present. We consider the total reflected, transmitted and cavity fields as shown in Fig. 9.6. Then, just as in eqs. (9.52) and (9.53), using $r_1' = -r_1$ and $t_1' = t_1$, at the first mirror we have

$$E_{\rm cav}(0) = t_1 E_{\rm in} - r_1 E'_{\rm cav}(0)\,, \tag{9.73}$$

$$E_{\rm refl} = r_1 E_{\rm in} + t_1 E'_{\rm cav}(0)\,. \tag{9.74}$$

Similarly, at the second mirror we have

$$E_{\rm t} = t_2 E_{\rm cav}(L)\,, \tag{9.75}$$

$$E'_{\rm cav}(L) = -r_2 E_{\rm cav}(L)\,. \tag{9.76}$$

Finally, since the solution inside the cavity is given by plane waves, the field $E_{\rm cav}(t,x)$, which represent a right-moving wave, is proportional to $\exp\{-i(\omega_{\rm L}t - k_{\rm L}x)\}$, while $E'_{\rm cav}(t,x)$, which represent a left-moving wave, is proportional to $\exp\{-i(\omega_{\rm L}t + k_{\rm L}x)\}$. Thus the cavity fields at $x = L$ and at $x = 0$, at equal value of time, are related by

$$E_{\rm cav}(L) = e^{ik_{\rm L}L} E_{\rm cav}(0)\,, \tag{9.77}$$

$$E'_{\rm cav}(L) = e^{-ik_{\rm L}L} E'_{\rm cav}(0)\,. \tag{9.78}$$

Then we have six equations, eqs. (9.73)–(9.78), that we can solve for the six quantities $E_{\rm refl}, E_{\rm t}, E_{\rm cav}(0), E_{\rm cav}(L), E'_{\rm cav}(0), E'_{\rm cav}(L)$, in terms of $E_{\rm in} = E_0 e^{-i\omega_{\rm L}t}$. With straightforward algebra we get back the solution found above. For instance, combining eqs. (9.76), (9.77) and (9.78) we get

$$E'_{\rm cav}(0) = -r_2 e^{2ik_{\rm L}L} E_{\rm cav}(0)\,. \tag{9.79}$$

Substituting this into eq. (9.73) we get

$$E_{\rm cav}(0) = t_1 E_{\rm in} + r_1 r_2 e^{2ik_{\rm L}L} E_{\rm cav}(0)\,, \tag{9.80}$$

from which the solution (9.72) for $E_{\rm cav}(0)$ follows, and similarly we get $E_{\rm refl}$ and $E_{\rm t}$.

Resonant FP cavities

We see that the reflected, transmitted and interior fields are all proportional to the factor $1/[1 - r_1 r_2 e^{2ik_{\rm L}L}]$. When $2k_{\rm L}L = 2\pi n$, with $n = 0, \pm 1, \pm 2, \ldots$, this factor becomes $1/(1 - r_1 r_2)$ and, if the reflection coefficients r_1 and r_2 are close to one, this is large. We therefore have a set of resonances. Physically this means that, for $2k_{\rm L}L = 2\pi n$, the various beams that bounce back and forth interfere constructively, so the field inside the cavity raises to a very large value. Correspondingly, the transmitted field also gets large. As for the reflected field, for assessing its strength we must also take into account the dependence on $k_{\rm L}L$ of the numerator, which describes the interference between the field that is reflected after having entered the cavity and made one or more round trips, and the field that is immediately reflected. We first consider the power $P_t \sim |E_{\rm t}|^2$ of the transmitted field (or, equivalently, of the interior field, $E_{\rm cav}$, since $|E_{\rm t}|$ and $|E_{\rm cav}|$ differ just by a constant factor t_2). From eq. (9.71),

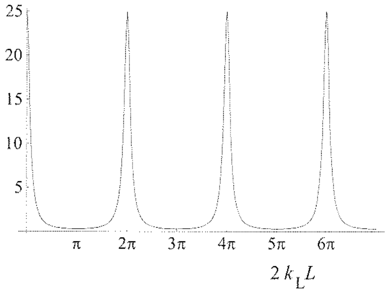

Fig. 9.9 $|E_{\rm t}|^2$, in units of $(E_0 t_1 t_2)^2$, as a function of $2k_{\rm L}L$, for $r_1 r_2 = 0.8$.

$$|E_{\rm t}|^2 = E_0^2\, \frac{t_1^2 t_2^2}{1 + (r_1 r_2)^2 - 2 r_1 r_2 \cos 2k_{\rm L}L}\,. \tag{9.81}$$

This is plotted, as a function of $2k_{\rm L}L$, in Fig. 9.9. Writing $k_{\rm L} = \omega_{\rm L}/c$, the distance between the maxima is

$$\Delta\omega_{\rm L} = \frac{\pi c}{L}\,. \tag{9.82}$$

This is called the *free spectral range* of the cavity. Expanding the denominator in eq. (9.81) to quadratic order around a resonance, we find that the full width of the peaks at half maximum is

$$\delta\omega_L = \frac{c}{L}\,\frac{1 - r_1 r_2}{\sqrt{r_1 r_2}}\,. \tag{9.83}$$

The *finesse* $\mathcal{F}$ of the cavity is defined as the ratio of the free spectral range to the full width at half maximum, $\mathcal{F} \equiv \Delta\omega_{\rm L}/\delta\omega_L$, so

$$\mathcal{F} = \frac{\pi\sqrt{r_1 r_2}}{1 - r_1 r_2}\,. \tag{9.84}$$

To understand the physical meaning of these results it is useful to compute the *storage time*, i.e. the average time spent by a photon inside the cavity. For simplicity we take $r_2 = 1$, so each photon has an amplitude probability $A(n)$ of making n round trips, and finally comes out from the first mirror. Recall that the number density of photons is proportional to the modulus squared of the electric field, so the factors $-r_1$ and $-r_2$ acquired at the reflections from the mirrors are the quantum-mechanical probability amplitudes, while their squared modulus is a probability. Thus, the amplitude for performing n round-trips and then coming out from the first mirror is given by $A(n) = t_1^2(-1)^n(-r_1)^{n-1} = \text{constant} \times r_1^n$, since each reflection at the far mirror has a probability amplitude -1 and at the first mirror $(-r_1)$. Thus, if a photon enters the cavity, the probability that it comes out after n round-trips is

$$p(n) = \frac{r_1^{2n}}{\sum_{n=1}^{\infty} r_1^{2n}}\,, \tag{9.85}$$

where the denominator normalizes the total probability to one. The average number of round-trips is therefore

$$\sum_{n=1}^{\infty} n\,p(n) = \frac{1}{1 - r_1^2}\,. \tag{9.86}$$

Since each round-trip lasts for a time $2L/c$, the storage time of the cavity, i.e. the average time spent inside by a photon, is

$$\tau_s = \frac{2L}{c}\,\frac{1}{1 - r_1^2}\,. \tag{9.87}$$

If r_1 is close to one we can write $1 - r_1^2 = (1 - r_1)(1 + r_1) \simeq 2(1 - r_1)$, and we can express the storage time in terms of the finesse, as

$$\tau_s \simeq \frac{L}{c}\,\frac{\mathcal{F}}{\pi}\,. \tag{9.88}$$

We see that, in the limit of high finesse, light is trapped in the FP cavity for a long time. If we illuminate the cavity and then we suddenly shut off the laser at $t = 0$, light will still continue to come out from the cavity for a long time. According to eq. (9.85), the intensity of the light coming out after n round trips is proportional to $r_1^{2n} = \exp\{n \log r_1^2\}$. For r_1 close to one, $\log r_1^2 = \log[1 - (1 - r_1^2)] \simeq -(1 - r_1^2)$. Therefore the intensity of light decreases with n as $\exp\{-n(1 - r_1^2)\}$. Since the light that performs n round trips comes out at time $t = (2L/c)n$, for r_1 close to one and $r_2 = 1$ the intensity of the reflected light decreases with time as $\exp\{-t(c/2L)(1 - r_1^2)\} = \exp\{-t/\tau_s\}$, with τ_s given in eq. (9.87), confirming the interpretation of τ_s as a storage time.

We consider now the reflected field. We write $E_{\rm refl} = |E_{\rm refl}|e^{-i\omega_{\rm L}t}e^{i\phi}$, and we find from eq. (9.70) that the phase ϕ can be written as $\phi = \phi_1 - \phi_2$, where

$$\tan\phi_1 = -\frac{r_2(1 - p_1)\sin(2k_{\rm L}L)}{r_1 - r_2(1 - p_1)\cos(2k_{\rm L}L)}\,, \tag{9.89}$$

$$\tan\phi_2 = -\frac{r_1 r_2 \sin(2k_{\rm L}L)}{1 - r_1 r_2\cos(2k_{\rm L}L)}\,. \tag{9.90}$$

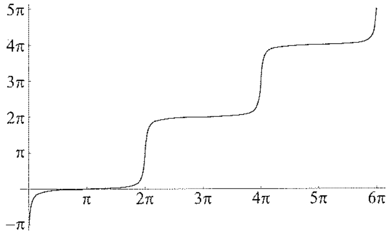

Fig. 9.10 The phase ϕ of the reflected field, as a function of $2k_{\rm L}L$, setting $r_1 = 0.9$, $r_2 = 1$, $p_1 = 0$. We have defined ϕ so that it is a continuous function of $2k_{\rm L}L$, rather than reporting it always to the interval $[0, 2\pi]$.

A plot of ϕ as a function of $2k_{\rm L}L$ is shown in Fig. 9.10. Two aspects of this graph are interesting. First, away from the resonances (which, as we have seen, are at $2k_{\rm L}L = 2\pi n$), ϕ is almost flat as a function of $2k_{\rm L}L$, and is basically equal to zero (mod 2π). So, here the phase of the reflected light is insensitive to changes in the length L of the cavity or of the frequency of the laser light. However, close to the resonances this dependence suddenly becomes very sharp. Writing $2k_{\rm L}L = 2\pi n + \epsilon$ and expanding for small ϵ, eqs. (9.89) and (9.90) give (setting for simplicity $r_2 = 1$ and $p_1 = 0$ and neglecting $O(\epsilon^2)$) $\partial\phi/\partial\epsilon = (1 + r_1)/(1 - r_1)$ or, taking r_1 close to one,

$$\boxed{\frac{\partial\phi}{\partial\epsilon} \simeq \frac{2\mathcal{F}}{\pi}\,.} \tag{9.91}$$

We can compare this with the result (9.2) for one arm of a simple Michelson interferometer which, in the present notation, reads $\phi = \epsilon$. When r_1 is close to one, the sensitivity of a FP cavity to changes in $2k_{\rm L}L$ is enhanced by the large factor $(2/\pi)\mathcal{F}$, compared to the arm of a Michelson interferometer.

The result for generic values of r_1, r_2 (but still such that $\mathcal{F} \gg 1$) can be conveniently written observing that, for large $\mathcal{F}$, eq. (9.84) can be inverted to give

$$r_1 r_2 = 1 - \frac{\pi}{\mathcal{F}} + O\left(\frac{\pi^2}{\mathcal{F}^2}\right)\,. \tag{9.92}$$

We define p from

$$(1 - p_1)r_2^2 = (1 - p)\,, \tag{9.93}$$

and we introduce the *coupling rate* σ,

$$\boxed{\sigma = \frac{p\mathcal{F}}{\pi}\,.} \tag{9.94}$$

From the condition $r_1^2 = 1 - p_1^2 - t_1^2 < 1 - p_1$ it follows that $r_1^2 r_2^2 < 1 - p$ and for small p (typical values in VIRGO and LIGO are $p \sim 2 \times 10^{-5}$)

we have $r_1 r_2 < 1 - (p/2)$. Using eq. (9.92) we then obtain

$$1 - \frac{\pi}{\mathcal{F}} < 1 - \frac{p}{2}, \tag{9.95}$$

which, in terms of σ, gives $\sigma < 2$. Since of course $\sigma > 0$, we have

$$0 < \sigma < 2. \tag{9.96}$$

Writing $2k_{\rm L}L = 2\pi n + \epsilon$ and expanding for small ϵ, eqs. (9.89) and (9.90) become $\tan\phi_1 = (\mathcal{F}\epsilon/\pi)/(1-\sigma)$ and $\tan\phi_2 = -\mathcal{F}\epsilon/\pi$, so $\phi_2 = -\pi + \arctan(\mathcal{F}\epsilon/\pi)$. For $\phi = \phi_1 - \phi_2$ we get

$$\boxed{\phi = \pi + \arctan\left[\frac{\mathcal{F}\epsilon}{\pi}\frac{1}{1-\sigma}\right] + \arctan\left[\frac{\mathcal{F}\epsilon}{\pi}\right].} \tag{9.97}$$

When $\sigma > 1$ this is rewritten more conveniently as

$$\phi = \arctan\left[\frac{\mathcal{F}\epsilon}{\pi}\frac{1}{\sigma-1}\right] + \arctan\left[\frac{\mathcal{F}\epsilon}{\pi}\right]. \tag{9.98}$$

Observe from eq. (9.70) that, at the resonances, the reflected electric field is

$$E_{\rm refl} = E_0 e^{-i\omega_{\rm L}t_0}\,\frac{r_1 - r_2(1-p_1)}{1 - r_1 r_2}. \tag{9.99}$$

In particular, if $r_1 = r_2(1-p_1)$, at resonance there is no reflected light from the cavity. Physically, what happens is that the light that is immediately reflected back interferes destructively with the light that is reflected after one or more round trips in the cavity.[15] This situation is called the *optimal (or critical) cavity coupling*. Of course, it is optimal from the point of view of the transmitted field since, except for the losses, all incident light finally leaks out from the second mirror. For the arms of a GW interferometer, we will see that we are interested in the reflected signal and therefore we do not want this situation. If $r_1 > r_2(1-p_1)$ the cavity is undercoupled, while for $r_1 < r_2(1-p_1)$ the cavity is overcoupled. In terms of the coupling rate, using the definition (9.94) and neglecting $O(\pi^2/\mathcal{F}^2)$ in eq. (9.92), we have

$$\frac{r_1 - r_2(1-p_1)}{1 - r_1 r_2} = \frac{\sigma - 1}{r_2}, \tag{9.100}$$

so optimal coupling corresponds to $\sigma = 1$, while for $0 < \sigma < 1$ the cavity is overcoupled, and for $1 < \sigma < 2$ the cavity is undercoupled. Observe that Fig. 9.10 refers to an overcoupled cavity. For undercoupled cavities, instead, the region where the phase of the reflected field is very sensitive to changes in $2k_{\rm L}L$ becomes smaller and smaller, and disappears completely when $\sigma \to 2$. A comparison of ϕ, as a function of ϵ, for $\sigma < 1$ and for $\sigma > 1$ is shown in Fig. 9.11. Clearly, the sensitivity to a change of $2k_{\rm L}L$ is higher for an overcoupled cavity. For the arms of VIRGO and LIGO, the losses are such that $p \sim 2 \times 10^{-5}$ and the finesse is $\mathcal{F} \simeq 50$ for VIRGO and $\mathcal{F} \simeq 200$ for LIGO, so we have $\sigma \sim 3 \times 10^{-4}$ for VIRGO and $\sigma \sim 10^{-3}$ for LIGO. Therefore these cavities are well overcoupled.

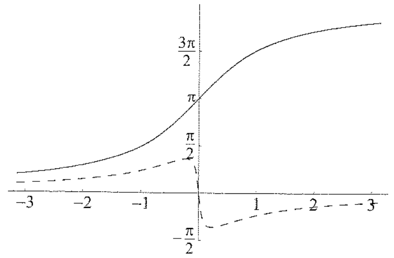

Fig. 9.11 The phase ϕ of the reflected field, as a function of $\epsilon = 2k_{\rm L}L - 2\pi n$, for an overcoupled cavity with $\sigma = 0.05$ (solid line) and for an undercoupled cavity with $\sigma = 1.05$ (dashed line).

---

[15] This at first sight can be surprising. If for instance $r_1 = 0.99$, almost all the incoming light is reflected back immediately and is not so intuitive that the total reflected field can be zero. What happens is that the small amount of light that enters the cavity eventually builds up a sufficiently strong interior cavity field, and the part of it that finally leaks back from the first mirror has a large enough amplitude, and the appropriate phase, to cancel the promptly reflected field.

9.2.2 Interaction of a FP cavity with GWs

We have seen that the effective storage time of light, which in the arm of a Michelson interferometer is $2L/c$, becomes $(L/c)\mathcal{F}/\pi$ in a Fabry–Perot cavity, i.e. is enhanced by a factor $\mathcal{F}/(2\pi)$, and the sensitivity to a phase shift is enhanced by a factor $(2/\pi)\mathcal{F}$. Since we finally measure a phase shift, we can expect that the same response to GWs of a Michelson interferometer with arm-length of hundreds of kms, as would be optimal for GWs with frequency $f_{\rm gw} = O(10^2)$ Hz, should be obtained replacing the arms by Fabry–Perot cavities with a length of a few kms, and a finesse $\mathcal{F} = O(10^2)$. Thus, our next approximation toward a realistic GW interferometer is as in Fig. 9.12. In this section we study the response of a FP interferometer to GWs, and we will see that the above expectation is indeed correct.

We want to compute how the reflected field of a FP cavity is affected by an incoming GW. We consider a FP cavity oriented along the x axis and a GW with only the plus polarization propagating along z, as in eq. (9.6). We begin with a description in the proper detector frame. As we saw in Section 9.1.2, in this frame we can easily obtain the result to lowest order in $\omega_{\rm gw}L/c$ by making use of the fact that, even in the presence of GWs, light propagates along the geodesics of flat spacetime, while the mirrors are shaken by a force exerted by GWs, so that their motion is given in eq. (9.37). Therefore the length L of the cavity changes as

$$\Delta L_x(t) = \frac{Lh_0}{2}\cos\omega_{\rm gw}t. \tag{9.101}$$

This induces a change $\Delta\phi_x$ in the phase ϕ_x of the field reflected from the cavity along the x arm, which is obtained from eq. (9.91), i.e. from $\Delta\phi_x = (2\mathcal{F}/\pi)\epsilon$, setting $\epsilon = 2k_{\rm L}\Delta L$,

$$\begin{aligned}\Delta\phi_x &\simeq \frac{4\mathcal{F}}{\pi}\,k_{\rm L}\Delta L \\ &= \frac{2\mathcal{F}}{\pi}\,k_{\rm L}Lh_0\cos\omega_{\rm gw}t.\end{aligned} \tag{9.102}$$

The phase shift of a FP cavity along the y arm is obtained reversing the sign of h_0 (see eq. (9.7)), so the total phase shift in the Fabry–Perot interferometer of Fig. 9.12 is $\Delta\phi_{\rm FP} = \Delta\phi_x - \Delta\phi_y = 2\Delta\phi_x$. We write $\Delta\phi_{\rm FP}(t) = |\Delta\phi_{\rm FP}|\cos\omega_{\rm gw}t$, so

$$|\Delta\phi_{\rm FP}| = \frac{4\mathcal{F}}{\pi}\,k_{\rm L}Lh_0. \tag{9.103}$$

This is the change of phase that would be induced in a Michelson interferometer with arm-length $(2/\pi)\mathcal{F}L$. Similar to what happens in a Michelson interferometer, we expect that, when the storage time τ_s given in eq. (9.88) becomes comparable to the period of the GW, the sensitivity degrades because we are summing over contributions with both positive and negative sign, so the above result is really the lowest order in an expansion in $\omega_{\rm gw}\tau_s$. To compute the result for $\omega_{\rm gw}\tau_s$ generic, we

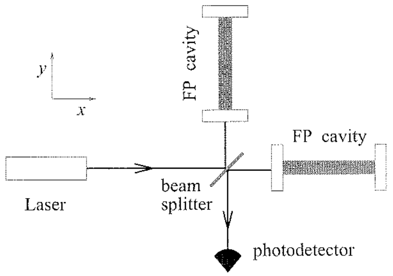

Fig. 9.12 The layout of an interferometer with Fabry–Perot cavities.

already know from our discussion in Section 9.1.2 that we cannot work in the proper detector frame, and we must rather switch to a TT gauge description.

First, it is useful to observe that, for a FP cavity, we can repeat without any modification the derivation done in eq. (9.34) for an arm of a Michelson interferometer, and we again conclude that, if a GW induces a phase shift $\Delta\phi_x(t) = |\Delta\phi_x| \cos\omega_{\rm gw}t$ in the field reflected from a cavity along the x axis, this produces in the reflected field sidebands with frequencies $\omega_{\rm L} \pm \omega_{\rm gw}$ and an amplitude, relative to the carrier, whose modulus is $|\Delta\phi_x|/2$ in each sideband. Thus, to compute the phase shift $|\Delta\phi_x|$ of the reflected field, to all order in $\omega_{\rm gw}\tau_s$, we can compute in the TT gauge the amplitude of the sidebands of the reflected field. This can be done generalizing the computation of pages 483–485 as follows.

Consider the electric field coming on the first mirror of the cavity from the laser, as in Fig. 9.8. This incoming field is monochromatic, and oscillates as $e^{-i\omega_{\rm L}t}$. When it enters the cavity and bounces once back and forth, besides acquiring the usual transmission and reflection coefficients, when a GW is present it also acquires a phase modulation, so that when it comes back to the first mirror it consists of the carrier at frequency $\omega_{\rm L}$ plus the two sidebands at $\omega_{\rm L} \pm \omega_{\rm gw}$. These three monochromatic fields are partly reflected, with the usual coefficient $-r_1$, and can make one more round trip in the cavity, and so on. So, we need to know how a generic field with carrier plus sidebands is modified by a round trip. We therefore consider a right-moving electromagnetic field which, at the left mirror, has the time-dependence

$$A(t) = A_0 e^{-i\omega_{\rm L}t} + \frac{1}{2}h_0 A_1 e^{-i(\omega_{\rm L}-\omega_{\rm gw})t} + \frac{1}{2}h_0 A_2 e^{-i(\omega_{\rm L}+\omega_{\rm gw})t}\,, \qquad (9.104)$$

while we denote by $B(t)$ the right-moving field at the end of the round trip,

$$B(t) = B_0 e^{-i\omega_{\rm L}t} + \frac{1}{2}h_0 B_1 e^{-i(\omega_{\rm L}-\omega_{\rm gw})t} + \frac{1}{2}h_0 B_2 e^{-i(\omega_{\rm L}+\omega_{\rm gw})t}\,. \qquad (9.105)$$

If we denote by t the time at which the field terminates its round-trip, the time t_0 at which it started is given by (compare with eq. (9.18))

$$t_0 = t - \frac{2L}{c} - \frac{L}{c}\, h_0 \cos[\omega_{\rm gw}(t - L/c)] \,{\rm sinc}\,(\omega_{\rm gw}L/c)\,. \qquad (9.106)$$

Since during free propagation the phase is unchanged, we must have (apart from the reflection coefficients at the mirrors that we will add separately) $B(t) = A(t_0)$,[16] that is

$$B(t) = A_0 e^{-i\omega_{\rm L}t_0} + \frac{1}{2}h_0 A_1 e^{-i(\omega_{\rm L}-\omega_{\rm gw})t_0} + \frac{1}{2}h_0 A_2 e^{-i(\omega_{\rm L}+\omega_{\rm gw})t_0}\,. \qquad (9.107)$$

Using eq. (9.106) and developing to first order in h_0,

$$\begin{aligned} e^{-i\omega_{\rm L}t_0} &= e^{-i\omega_{\rm L}(t-2L/c)} \qquad (9.108)\\ &\quad + \frac{1}{2}h_0\, ik_{\rm L}L \,{\rm sinc}\,(\omega_{\rm gw}L/c) e^{i(2\omega_{\rm L}-\omega_{\rm gw})L/c}\, e^{-i(\omega_{\rm L}-\omega_{\rm gw})t}\\ &\quad + \frac{1}{2}h_0\, ik_{\rm L}L \,{\rm sinc}\,(\omega_{\rm gw}L/c) e^{i(2\omega_{\rm L}+\omega_{\rm gw})L/c}\, e^{-i(\omega_{\rm L}+\omega_{\rm gw})t}\,. \end{aligned}$$

---

[16] Recall that the superposition of carrier and sidebands given in eqs. (9.104) and (9.105) derives from the expansion of a phase factor, see eqs. (9.24) and (9.34).

Again to order h_0, we can simply replace the terms $h_0 e^{-i(\omega_{\rm L}\pm\omega_{\rm gw})t_0}$ in eq. (9.107) by $h_0 e^{-i(\omega_{\rm L}\pm\omega_{\rm gw})(t-2L/c)}$. Collecting terms with the same time dependence in eq. (9.107) and comparing with eq. (9.105) we get a matrix relation $B_i = X_{ij}A_j$ (with $i = 0, 1, 2$), where

$$\mathbf{X} = \begin{pmatrix} X_{00} & 0 & 0 \\ X_{10} & X_{11} & 0 \\ X_{20} & 0 & X_{22} \end{pmatrix}. \qquad (9.109)$$

The diagonal elements describe the free propagation of the carrier and of the sidebands, while the X_{10} and X_{20} term describe the fact that a round-trip of the carrier produces further contributions to the sidebands. Using eq. (9.108), the explicit expression of the matrix elements is

$$\begin{aligned} X_{00} &= e^{2i\omega_{\rm L}L/c}\,,\\ X_{11} &= e^{2i(\omega_{\rm L}-\omega_{\rm gw})L/c}\,,\\ X_{22} &= e^{2i(\omega_{\rm L}+\omega_{\rm gw})L/c}\,. \qquad (9.110)\\ X_{10} &= ik_{\rm L}L \,{\rm sinc}\,(\omega_{\rm gw}L/c) e^{i(2\omega_{\rm L}-\omega_{\rm gw})L/c}\,,\\ X_{20} &= ik_{\rm L}L \,{\rm sinc}\,(\omega_{\rm gw}L/c) e^{i(2\omega_{\rm L}+\omega_{\rm gw})L/c}\,. \end{aligned}$$

For a Fabry–Perot cavity along the y axis the same expressions hold, inverting the sign of h_0 (see eq. (9.7)) or, equivalently, inverting the sign of X_{10} and of X_{20}.

This result allows us to generalize eq. (9.80) to the case when GWs are present, simply replacing the factors $e^{2ik_{\rm L}L}$ with the matrix $\mathbf{X}$. Thus, we can write the fields $\mathcal{B} = (B_0, B_1, B_2)$ inside the cavity, at $x = 0$, in matrix form as

$$\mathcal{B} = t_1\mathcal{A}_{\rm in} + r_1 r_2 \mathbf{X}\mathcal{B}\,, \qquad (9.111)$$

where $\mathcal{A}_{\rm in} = (E_0, 0, 0)$. The solution is

$$\mathcal{B} = (\mathbf{1} - r_1 r_2\mathbf{X})^{-1} t_1 \mathcal{A}_{\rm in}\,. \qquad (9.112)$$

This is the right-moving field at the first mirror (the equivalent of what we denoted by $E_{\rm cav}(0)$ in the absence of GWs, see Fig. 9.6). The left-moving field ($E'_{\rm cav}(0)$ in Fig. 9.6) in the absence of GWs is obtained from $E_{\rm cav}(0)$ using eq. (9.79). In the presence of GWs, we have seen that the factor $e^{2ik_{\rm L}L}$ is replaced by the matrix $\mathbf{X}$, acting on the vector space of the amplitude of the carrier and of the sidebands, so the left-moving field is now

$$\mathcal{B}' = -r_2\mathbf{X}\mathcal{B}\,, \qquad (9.113)$$

and the total reflected field, which includes also the promptly reflected part, is given by

$$\begin{aligned} \mathcal{A}_{\rm refl} &= r_1\mathcal{A}_{\rm in} - t_1 r_2 \mathbf{X}\mathcal{B}\\ &= [r_1 - r_2(1 - p_1)\mathbf{X}](\mathbf{1} - r_1 r_2 \mathbf{X})^{-1}\mathcal{A}_{\rm in}\,, \qquad (9.114) \end{aligned}$$

which replaces eq. (9.70). Setting $\mathcal{A}_{\rm in} = (1, 0, 0)$, we can now compute $\mathcal{A}_{\rm refl} \equiv (\mathcal{A}_0, \mathcal{A}_1, \mathcal{A}_2)$. According to eq. (9.34), and taking into account the factor $h_0/2$ in the definition (9.104), the phase shift $|\Delta\phi_x|$ in a single Fabry–Perot cavity along the x axis, is given by

$$\frac{1}{2}|\Delta\phi_x| = \frac{1}{2}h_0\left|\frac{\mathcal{A}_1}{\mathcal{A}_0}\right| . \tag{9.115}$$

We are interested in particular in the situation when the FP cavity is locked on resonance, so $e^{2ik_L L} = 1$. In this case, with straightforward matrix algebra (easily performed with the help of any symbolic manipulation program) we get

$$\frac{\mathcal{A}_1}{\mathcal{A}_0} = X_{10}\, e^{2i\omega_{\rm gw}L/c}\, \frac{r_2(1-p) - r_1^2 r_2}{(e^{2i\omega_{\rm gw}L/c} - r_1 r_2)[r_2(1-p) - r_1]} , \tag{9.116}$$

so

$$\begin{aligned} |\Delta\phi_x| &= h_0 k_L L\, {\rm sinc}\,(\omega_{\rm gw}L/c)\, \frac{r_2(1-r_1^2-p)}{[r_2(1-p)-r_1]}\, \frac{1}{|e^{2i\omega_{\rm gw}L/c} - r_1 r_2|} \\ &= h_0 k_L L\, {\rm sinc}\,(\omega_{\rm gw}L/c)\, \frac{r_2(1-r_1^2-p)}{[r_2(1-p)-r_1]} \\ &\quad \times \frac{1}{[1+(r_1r_2)^2 - 2r_1r_2\cos(2\omega_{\rm gw}L/c)]^{1/2}} . \end{aligned} \tag{9.117}$$

If we set $p = 0$ and $r_2 = 1$ (e.g. the present value for VIRGO is $r_2 \simeq 0.99995$) and we take r_1 close to one, the first fraction becomes simply $1 + r_1 \simeq 2$. So, we write

$$\frac{r_2(1-r_1^2-p)}{[r_2(1-p)-r_1]} = 2[1+\epsilon(r_1, r_2, p)] , \tag{9.118}$$

where, in the typical experimental situation, $\epsilon(r_1, r_2, p) \ll 1$. Then

$$|\Delta\phi_x| = h_0\, 2k_L L\, [1+\epsilon(r_1, r_2, p)] \frac{{\rm sinc}\,(\omega_{\rm gw}L/c)}{[1+(r_1r_2)^2 - 2r_1r_2\cos(2\omega_{\rm gw}L/c)]^{1/2}} . \tag{9.119}$$

The dependence on $\omega_{\rm gw}L/c$ can be simplified observing that we want to have $\mathcal{F}L/c$ comparable to the wavelength of the GW, so $\mathcal{F}\omega_{\rm gw}L/c = O(1)$. However, we achieve this by using a large value of $\mathcal{F}$, so $\omega_{\rm gw}L/c$ is much smaller than one in the region where the interferometer operates. For instance, if $f_{\rm gw} = 100$ Hz and $L = 4$ km, $\omega_{\rm gw}L/c \sim 10^{-2}$. We can therefore replace ${\rm sinc}\,(\omega_{\rm gw}L/c) \simeq 1$ in the numerator, and we expand $\cos(2\omega_{\rm gw}L/c)$ in the denominator. Then we get

$$\begin{aligned} |\Delta\phi_x| &\simeq h_0\, 2k_{\rm L}L\, \frac{1+\epsilon(r_1, r_2, p)}{1 - r_1 r_2}\, \frac{1}{[1 + \frac{r_1 r_2}{(1-r_1r_2)^2}(2\omega_{\rm gw}L/c)^2]^{1/2}} \\ &\simeq h_0\, 2k_{\rm L}L\, \frac{\mathcal{F}}{\pi}\, \frac{1}{[1+(4\pi f_{\rm gw}\tau_s)^2]^{1/2}} , \end{aligned} \tag{9.120}$$

where, in the last line, we wrote the result in terms of the finesse $\mathcal{F}$, given in eq. (9.84), and of the storage time τ_s of the cavity, given in eq. (9.87), and we neglected in the numerator terms that are small when

$r_2, r_1 \to 1$. The phase shift of a FP cavity along the y arm is obtained changing the sign of h_0, so $\Delta\phi_y = -\Delta\phi_x$, and the difference between them is $\Delta\phi_{\rm FP} = \Delta\phi_x - \Delta\phi_y = 2\Delta\phi_x$.

We rewrite the result introducing the so-called *pole frequency*,

$$\boxed{f_p \equiv \frac{1}{4\pi\tau_s} ,} \tag{9.121}$$

or, from eq. (9.88),

$$f_p \simeq \frac{c}{4\mathcal{F}L} . \tag{9.122}$$

For initial LIGO, $L = 4$ km and $\mathcal{F} \simeq 200$ this gives $f_p \simeq 90$ Hz. For VIRGO, $L = 3$ km and $\mathcal{F} \simeq 50$, so $f_p \simeq 500$ Hz. The phase shift in a Fabry–Perot interferometer can then be written as

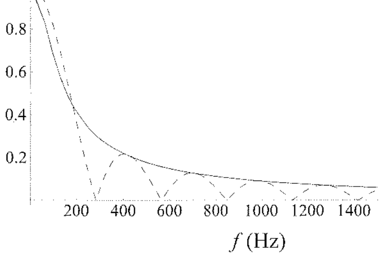

Fig. 9.13 A plot of the function $[1+(f/f_p)^2]^{-1/2}$, (solid line), compared to the function $|{\rm sinc}\,(f/f_p)|$ (dashed line). We have taken $f_p = 90$ Hz.

$$\boxed{|\Delta\phi_{\rm FP}| \simeq h_0\, \frac{4\mathcal{F}}{\pi}\, k_{\rm L}L\, \frac{1}{\sqrt{1+(f_{\rm gw}/f_p)^2}} .} \tag{9.123}$$

For $f_{\rm gw} \ll f_p$ we recover the result found in the proper detector frame, eq. (9.103), as expected.[17] At $f_{\rm gw} \gg f_p$, eq. (9.123) shows that the sensitivity degrades linearly with $f_{\rm gw}$. This formula holds as long as $\omega_{\rm gw}L/c \ll 1$, i.e

$$\begin{aligned} f_{\rm gw} &\ll \frac{c}{2\pi L} \\ &\simeq 12\ {\rm kHz}\left(\frac{4\,{\rm km}}{L}\right) . \end{aligned} \tag{9.124}$$

Above this frequency the factor ${\rm sinc}\,(\omega_{\rm gw}L/c)$ in eq. (9.119) can no longer be approximated by one, and cuts the response further, reflecting the fact that in each round-trip the GW changes sign.

In Fig. 9.13 we show the function $1/[1+(f_{\rm gw}/f_p)^2]^{1/2}$, and we compare it with the function $|{\rm sinc}\,(f/f_p)|$, which is the corresponding quantity for a Michelson interferometer whose length $L_{\rm Mich} = (2/\pi)\mathcal{F}L$ is chosen so that, in the limit $f_{\rm gw} \to 0$, its response function is the same as a FP cavity of length L and finesse $\mathcal{F}$.

It is useful to write eq. (9.123) in the form

$$|\Delta\phi_{\rm FP}| = h_0 T_{\rm FP}(f) , \tag{9.125}$$

where (writing $k_{\rm L} = 2\pi/\lambda_{\rm L}$)

$$\boxed{T_{\rm FP}(f) \simeq \frac{8\mathcal{F}L}{\lambda_{\rm L}}\, \frac{1}{\sqrt{1+(f_{\rm gw}/f_p)^2}} ,} \tag{9.126}$$

is the transfer function of an interferometer with Fabry–Perot cavities.

---

[17] Recall that eq. (9.91), and therefore eq. (9.103), were obtained in the limit $r_2 = 1$, $p = 0$ and r_1 close to one. If we keep r_1 generic, still setting $r_2 = 1$ and $p = 0$, in eq. (9.91) the overall factor of 2 is replaced by $1 + r_1$, and the same result is obtained from eq. (9.117).

9.2.3 Angular sensitivity and pattern functions

Until now we have restricted ourselves to a GW with plus polarization, propagating along the z axis. We now compute the response of an interferometer to GWs with arbitrary direction and polarization. As discussed in Section 7.2, this is encoded in the pattern functions $F_+(\theta,\phi)$ and $F_\times(\theta,\phi)$. We first consider the limit $\omega_{\rm gw}L/c \ll 1$. In this case we can use the proper detector frame, so the motion of the mirrors is governed by the geodesic equation,

$$\ddot{\xi}^i = \frac{1}{2}\ddot{h}_{ij}\xi^j\,. \tag{9.127}$$

For the mirror located at $\xi^j = (L,0,0)$, we are interested in its displacement along the x direction, which is given by

$$\ddot{\xi}_x = \frac{1}{2}\ddot{h}_{xx}L\,. \tag{9.128}$$

This equation governs the change in the length of the x-arm of a Michelson interferometer, as well as the change in the length of a FP cavity lying along the x axis. For the mirror located at $\xi^j = (0,L,0)$, we are rather interested in its displacement along the y direction, which is given by

$$\ddot{\xi}_y = \frac{1}{2}\ddot{h}_{yy}L\,. \tag{9.129}$$

The relative phase shift between the x and y arms is therefore driven by $(1/2)(\ddot{h}_{xx} - \ddot{h}_{yy})$. When the wave comes from the z direction we have $h_{xx} = h_+$ and $h_{xx} = -h_+$, so $(1/2)(h_{xx} - h_{yy}) = h_+$, but in the most general situation we must replace h_+ by $(1/2)(h_{xx} - h_{yy})$ in the computations of the phase shift in a Michelson or in a FP interferometer performed in the previous sections. In other words, the detector tensor (defined in eq. (7.1)) for an interferometer with arms along the $\hat{\mathbf{x}}$ and $\hat{\mathbf{y}}$ directions is

$$D_{ij} = \frac{1}{2}(\hat{\mathbf{x}}_i\hat{\mathbf{x}}_j - \hat{\mathbf{y}}_i\hat{\mathbf{y}}_j)\,. \tag{9.130}$$

We compute h_{xx} and h_{yy} in terms of $h_+, h_\times$ for a wave coming from arbitrary direction. The computation is similar to that performed for resonant bars on page 425. The geometry is illustrated in Fig. 9.14: we have a frame (x,y,z) such that the arms of the interferometer are along the x and y axes. We introduce a second reference frame (x',y',z') such that the propagation direction of the GW coincides with the z' axis. With respect to the (x,y,z) frame, the z' axis has polar angles θ and ϕ, defined as in the figure.[18]

The polarizations h_+ and $h_\times$ are defined with respect to the (x',y') axes, so in the (x',y',z') frame the GW has the form

$$h'_{ij} = \begin{pmatrix} h_+ & h_\times & 0 \\ h_\times & -h_+ & 0 \\ 0 & 0 & 0 \end{pmatrix}_{ij}\,. \tag{9.131}$$

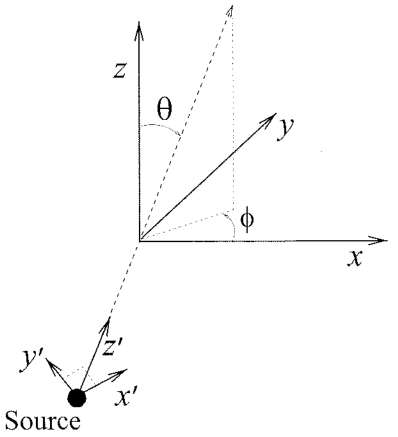

Fig. 9.14 The geometry used in the computation of the pattern functions. The arms of the interferometer are along the x and y axes.

---

[18] When comparing with the calculation for resonant bars on page 425, observe that here we define θ as the angle from the z axis, rather than from the x axis.

The rotation that brings the (x',y',z') frame onto the (x,y,z) frame is given by a rotation by an angle θ around the y axis followed by a rotation by an angle ϕ around the z axis, i.e.

$$\mathcal{R} = \begin{pmatrix} \cos\phi & \sin\phi & 0 \\ -\sin\phi & \cos\phi & 0 \\ 0 & 0 & 1 \end{pmatrix} \begin{pmatrix} \cos\theta & 0 & \sin\theta \\ 0 & 1 & 0 \\ -\sin\theta & 0 & \cos\theta \end{pmatrix}\,. \tag{9.132}$$

The GW in the (x,y,z) frame is then given by the transformation law of a tensor with two indices, $h_{ij} = \mathcal{R}_{ik}\mathcal{R}_{jl}h'_{kl}$. From this we obtain

$$h_{xx} = h_+(\cos^2\theta\cos^2\phi - \sin^2\phi) + 2h_\times\cos\theta\sin\phi\cos\phi\,, \tag{9.133}$$

$$h_{yy} = h_+(\cos^2\theta\sin^2\phi - \cos^2\phi) - 2h_\times\cos\theta\sin\phi\cos\phi\,, \tag{9.134}$$

so

$$\frac{1}{2}(h_{xx} - h_{yy}) = \frac{1}{2}h_+(1+\cos^2\theta)\cos 2\phi + h_\times\cos\theta\sin 2\phi\,, \tag{9.135}$$

and therefore

$$\boxed{\begin{aligned} F_+(\theta,\phi) &= \frac{1}{2}(1+\cos^2\theta)\cos 2\phi\,, \\ F_\times(\theta,\phi) &= \cos\theta\sin 2\phi\,. \end{aligned}} \tag{9.136}$$

We see that GW interferometers have blind directions. For instance, for a GW with plus polarization, the direction with $\phi = \pi/4$ is blind, since $F_+ = 0$. This is due to the fact that this wave produces the same displacement in the x and in the y arm, so the differential phase shift vanishes. If we change the definition of the axes with respect to which the polarizations h_+ and $h_\times$ are defined, rotating them by an angle ϕ in the (x',y') plane, the pattern functions transform as in eq. (7.30).

Equation (9.136) has been obtained in the limit $\omega_{\rm gw}L/c \ll 1$. To compute the pattern functions for $\omega_{\rm gw}L/c$ generic we must perform the computation in the TT gauge, so we should repeat the computation leading to eq. (9.15) for a GW coming from arbitrary direction. Consider the arm of a simple Michelson interferometers, with the beam splitter at $x=0$ and the far mirror at $x = L_x$ (or a FP cavity with mirrors at $x=0$ and $x = L_x$). Then eq. (9.9) is replaced by

$$L_x = c(t_1 - t_0) - \frac{c}{2}\int_{t_0}^{t_1} dt'\,h_{xx}(t',\mathbf{x})\,. \tag{9.137}$$

If we denote by $\hat{\mathbf{n}}$ the propagation direction of the GW, we have $h_{xx}(t) = h_{xx}\cos[\omega_{\rm gw}(t - \hat{\mathbf{n}}\cdot\mathbf{x}/c)]$, and we must evaluate $\mathbf{x}$ on the trajectory $\mathbf{x}(t)$ of the photon, so along the x arm we have

$$h_{xx}(t) = h_{xx}\cos\left[\omega_{\rm gw}\left(t - \frac{n_x x(t)}{c}\right)\right]\,, \tag{9.138}$$

which replaces eq. (9.6). To lowest order in h_{xx} the trajectory of a photon is just the unperturbed one, so inside the cosine we can set $x(t) = c(t - t_0)$, while $\hat{\mathbf{n}}$ can be written in terms of the angles θ, ϕ as $\hat{\mathbf{n}} = (\sin\theta\cos\phi, \sin\theta\sin\phi, \cos\theta)$. Therefore, beside the dependence on (θ, ϕ) in h_{xx} and h_{yy}, that we already computed in eqs. (9.133) and (9.134), there is also an angular dependence through the term n_x in eq. (9.138), and a similar term n_y for the y arm. In particular, eq. (9.137) becomes

$$\begin{aligned} L_x = c(t_1 - t_0) - \frac{c}{2}\, h_{xx} \int_{t_0}^{t_1} dt' \\ \times \cos\left[(1 - \sin\theta\cos\phi)\omega_{\rm gw} t' + \omega_{\rm gw} t_0 \sin\theta\cos\phi\right] . \end{aligned} \tag{9.139}$$

The return trip can be treated similarly, with the unperturbed photon trajectory given now by $x(t) = L - c(t - t_1)$, so eq. (9.11) is replaced by

$$\begin{aligned} L_x = c(t_2 - t_1) - \frac{c}{2}\, h_{xx} \int_{t_1}^{t_2} dt' \\ \times \cos\left[(1 + \sin\theta\cos\phi)\omega_{\rm gw} t' - \omega_{\rm gw}(t_1 + L/c)\, \sin\theta\cos\phi\right] . \end{aligned} \tag{9.140}$$

Summing the two equations we get

$$\begin{aligned} t_2 = t_0 + \frac{2L_x}{c} + \frac{1}{2} h_{xx} \int_{t_0}^{t_0 + L_x/c} dt' \cos[\omega_- t' + \phi_0] \\ + \frac{1}{2} h_{xx} \int_{t_0 + L_x/c}^{t_0 + 2L_x/c} dt' \cos[\omega_+ t' - \phi_2] , \end{aligned} \tag{9.141}$$

where we introduced the short-hand notation

$$\omega_\pm = \omega_{\rm gw}(1 \pm \sin\theta\cos\phi) , \tag{9.142}$$

$$\phi_0 = \omega_{\rm gw} t_0\, \sin\theta\cos\phi , \tag{9.143}$$

$$\phi_2 = \omega_{\rm gw} t_2\, \sin\theta\cos\phi , \tag{9.144}$$

and in the limits of the integral, as well as in ϕ_2, we can use $t_1 = t_0 + L_x/c$ and $t_2 = t_0 + 2L_x/c$. For the y arm we have similar expressions, with L_y replacing L_x and $n_y = \sin\theta\sin\phi$ replacing $n_x = \sin\theta\cos\phi$.

It is now in principle straightforward to perform the integrals and compute how $t_2 - t_0$ depends on the propagation direction of the GW. Carrying out the integrals, however, we see that all terms which depend on θ, ϕ are multiplied by the factor $\omega_{\rm gw} L_x/c$. For instance, θ and ϕ enter in terms such as

$$\text{sinc}\left[\frac{\omega_{\rm gw} L_x}{2c}(1 \pm \sin\theta\cos\phi)\right] . \tag{9.145}$$

For a FP interferometer we saw that $\omega_{\rm gw} L_x/c$ is small, typically $O(10^{-2})$ in LIGO and VIRGO, and therefore the function sinc in eq. (9.145) is essentially unity, and its dependence on θ and ϕ is negligible, at least as long as the condition (9.124) is satisfied. Then, we can neglect the dependence on the GW direction in the travel time $t_2 - t_0$ and the only angular dependence comes from h_{xx} and h_{yy}, as computed in eqs. (9.133) and (9.134), so for the pattern function we can use, to a very good approximation, the expressions given in eq. (9.136).

9.3 Toward a real GW interferometer

In this section we discuss a number of issues that are more technical, but are important for understanding how a real interferometer works.

9.3.1 Diffraction and Gaussian beams

Until now we have considered idealized FP cavities with mirrors of infinite transverse extent, so we could neglect any dependence of the electric field on the transverse coordinates. For a cavity along the x axis, we have then treated the interior electric field as a plane wave, with a dependence on x, t of the form $\exp\{-i\omega_L(t \pm x/c)\}$, and no dependence on the transverse coordinates $\mathbf{x}_\perp = (y, z)$. Of course, in practice the mirrors have a finite extent, and the beam has a profile in the transverse direction.

A beam of finite transverse extent is subject to diffraction. If, at some point in space, a photon of wavelength $\lambda_{\rm L}$ (and therefore longitudinal momentum $p = \hbar/\lambdabar_L$) is localized within a transverse width $\Delta\mathbf{x}_\perp = a$, by the Heisenberg principle it has an uncertainty on the transverse momentum $\Delta p_\perp \sim \hbar/a$, so the beam will widen, filling a cone of angle $\Delta\theta = \Delta p_\perp/p \sim \lambdabar_L/a$. After traveling a longitudinal distance x the beam has become larger, in the transverse direction, by $x\Delta\theta \sim x\lambdabar_L/a$. As long as $x\lambdabar_L/a \ll a$ we are in the regime of *Fresnel diffraction*, and the broadening of the beam is negligible. When $x\lambdabar_L/a \gg a$, or, in terms of $k_L = 1/\lambdabar_L$,

$$x \gg k_{\rm L} a^2 , \tag{9.146}$$

we are in the regime of *Fraunhofer diffraction*, and the beam has become much broader than its original size. For interferometers such as LIGO and VIRGO, the wavelength of the laser is typically

$$\lambda_{\rm L} \simeq 1\,\mu m . \tag{9.147}$$

The border between these regimes is at $a = (x\lambdabar)^{1/2}$ which, for $x = 4$ km and $\lambda_{\rm L} = 1\,\mu$m, gives $a \simeq 2.5$ cm. This means that, for a laser beam whose initial width is smaller that 2.5 cm, the broadening of the beam becomes important already after a single one-way trip through the cavity. Furthermore for cavities with a finesse $O(100)$, as we need for GW detection, the beam is supposed to perform $O(100)$ round trips and, if the mirrors were flat, at each one-way trip the beam would widen further, as illustrated in Fig. 9.15, and would be finally dispersed on a region of transverse size larger than the mirrors.

Thus, it is clear that diffraction effects are important, and the naive scheme of a narrow beam (as typically obtained from a laser) bouncing between two flat mirrors cannot work. As a first step, we must understand in more detail the propagation of a beam of finite transverse extent over large distances. The tool that we need is the *paraxial propagator*, that we introduce in the next subsection.

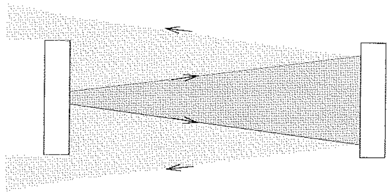

Fig. 9.15 The widening of a beam due to diffraction as it bounces between two flat mirrors.

The paraxial propagator

A given spatial component of the electric field, propagating in the vacuum, obeys the equation

$$\left[-\frac{1}{c^2}\frac{\partial^2}{\partial t^2}+\boldsymbol{\nabla}^2\right]E(t,\mathbf{x})=0\,. \tag{9.148}$$

We take a single monochromatic component, which we write in complex notation as $E(t,\mathbf{x})=E(\mathbf{x})e^{-i\omega_{\rm L}t}$, so $E(\mathbf{x})$ satisfies

$$[\boldsymbol{\nabla}^2+k_{\rm L}^2]E(\mathbf{x})=0\,. \tag{9.149}$$

We want to compute the propagation across a long distance in the x direction, so x is the longitudinal coordinate and $\mathbf{x}_\perp=(y,z)$ are the transverse coordinate, and we search for solutions of the form

$$E(\mathbf{x})=\mathcal{E}(x;y,z)e^{ik_{\rm L}x}\,, \tag{9.150}$$

where $\mathcal{E}(x;y,z)$ is a slowly varying function of x, in the sense that

$$|\partial_x\mathcal{E}|\ll k_{\rm L}|\mathcal{E}|\,. \tag{9.151}$$

Therefore $E(t,\mathbf{x})=\mathcal{E}(x;y,z)\exp\{-i\omega_{\rm L}t+ik_{\rm L}x\}$ is in a first approximation a plane wave, with a slower dependence on x, which manifests itself only on scales $x\gg\lambda_{\rm L}$. Plugging the ansatz (9.150) into eq. (9.149) we get

$$\boldsymbol{\nabla}_\perp^2\mathcal{E}+2ik_{\rm L}\partial_x\mathcal{E}+\partial_x^2\mathcal{E}=0\,, \tag{9.152}$$

where $\boldsymbol{\nabla}_\perp^2=\partial_y^2+\partial_z^2$. Because of the condition (9.151), we can neglect $\partial_x^2\mathcal{E}$ with respect to $k_{\rm L}\partial_x\mathcal{E}$, so in this approximation we write

$$\boldsymbol{\nabla}_\perp^2\mathcal{E}+2ik_{\rm L}\partial_x\mathcal{E}=0\,. \tag{9.153}$$

We now perform the Fourier transform with respect to the transverse variables,

$$\mathcal{E}(x;y,z)=\int\frac{dp_y}{2\pi}\frac{dp_z}{2\pi}\,\tilde{\mathcal{E}}(x;p_y,p_z)\,e^{ip_yy+ip_zz}\,. \tag{9.154}$$

In terms of $\tilde{\mathcal{E}}(x;p_y,p_z)$, eq. (9.153) reads

$$-(p_y^2+p_z^2)\tilde{\mathcal{E}}(x;p_y,p_z)+2ik_{\rm L}\partial_x\tilde{\mathcal{E}}(x;p_y,p_z)=0\,. \tag{9.155}$$

The x dependence can be integrated, and we get

$$\tilde{\mathcal{E}}(x;p_y,p_z)=\tilde{\mathcal{E}}(x=0;p_y,p_z)\exp\left\{-i\frac{p_y^2+p_z^2}{2k_{\rm L}}\,x\right\}\,. \tag{9.156}$$

Then eq. (9.154) becomes

$$\begin{aligned}\mathcal{E}(x;y,z)&=\int\frac{dp_y}{2\pi}\frac{dp_z}{2\pi}\,\tilde{\mathcal{E}}(x=0;p_y,p_z)\,e^{ip_yy+ip_zz-i\frac{p_y^2+p_z^2}{2k_{\rm L}}\,x}\\
&=\int\frac{dp_y}{2\pi}\frac{dp_z}{2\pi}\left[\int dy'dz'\,\tilde{\mathcal{E}}(x=0;y',z')e^{-ip_yy'+ip_zz'}\right]\\
&\quad\times e^{ip_yy+ip_zz-i\frac{p_y^2+p_z^2}{2k_{\rm L}}\,x}\\
&=\int dy'dz'\,\tilde{\mathcal{E}}(x=0;y',z')\\
&\quad\times\int\frac{dp_y}{2\pi}\frac{dp_z}{2\pi}\,e^{ip_y(y-y')+ip_z(z-z')-i\frac{p_y^2+p_z^2}{2k_{\rm L}}\,x}\,.\end{aligned} \tag{9.157}$$

The integrals over dp_y and dp_z are Fresnel integrals, that we already met in eq. (4.365), so we finally get

$$\boxed{\mathcal{E}(x;y,z)=\int dy'dz'\,G(x;y-y',z-z')\,\tilde{\mathcal{E}}(x=0;y',z')\,,} \tag{9.158}$$

where

$$\boxed{G(x;y-y',z-z')=\frac{-ik_{\rm L}}{2\pi x}\,\exp\left\{i\frac{k_{\rm L}}{2x}\left[(y-y')^2+(z-z')^2\right]\right\}} \tag{9.159}$$

is called the paraxial propagator. Equations (9.158) and (9.159) allow us to compute the field at x generic, once we have its value on a transverse surface $x=0$.

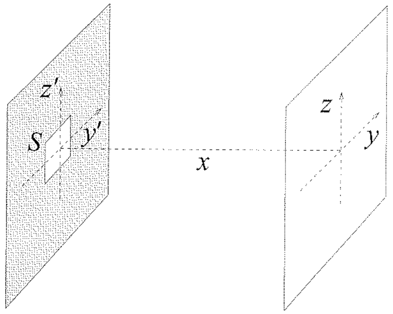

Fig. 9.16 An aperture S on a opaque screen. The plane of the opaque screen is parametrized by coordinates (y',z'). The image is observed on a screen at a distance x, parametrized by coordinates (y,z).

Fraunhofer diffraction

As a first application, we consider a plane wave of infinite transverse extent that arrives on an aperture S on a plane opaque screen and we compute the image on another screen at a large distance x, and at transverse coordinates (y,z), see Fig. 9.16. Then, at $x=0$, we have $\tilde{\mathcal{E}}(x=0;y',z')=\tilde{\mathcal{E}}_0$ if (y',z') are inside the aperture S, and zero otherwise, so

$$\begin{aligned}E(x,y,z)&=\frac{-ik_{\rm L}}{2\pi x}\,\tilde{\mathcal{E}}_0\,e^{ik_{\rm L}x}\int_S dy'dz'\,\exp\left\{i\frac{k_{\rm L}}{2x}[(y-y')^2+(z-z')^2]\right\}\\
&=\frac{-ik_{\rm L}}{2\pi x}\,\tilde{\mathcal{E}}_0\exp\left\{ik_{\rm L}\left[x+\frac{y^2+z^2}{2x}\right]\right\}\\
&\quad\times\int_S dy'dz'\,\exp\left\{-i\frac{k_{\rm L}}{x}(yy'+zz')+i\frac{k_{\rm L}}{x}({y'}^2+{z'}^2)\right\}\,.\end{aligned} \tag{9.160}$$

Fraunhofer diffraction is defined by the condition (9.146), where a is the size of the aperture. In this limit, we can neglect the term $k_{\rm L}({y'}^2+{z'}^2)/x$ in the exponential. Furthermore we observe that, if $y^2+z^2\ll x^2$, the term $x+(y^2+z^2)/2x$ in the first exponential is just the first-order expansion of the distance $r = (x^2 + y^2 + z^2)^{1/2}$ from the observation point to the center of the aperture, since

$$\begin{aligned}(x^2 + y^2 + z^2)^{1/2} &= x\left(1 + \frac{y^2 + z^2}{x^2}\right)^{1/2}\\ &\simeq x\left(1 + \frac{y^2 + z^2}{2x^2}\right). \qquad (9.161)\end{aligned}$$

Similarly, to lowest order we can replace $1/x$ with $1/r$ in eq. (9.160). Then we get the well-known formula for the Fraunhofer diffraction by an aperture,

$$\boxed{E(x, y, z) = \frac{-i\tilde{\mathcal{E}}_0 k_{\rm L}}{2\pi} \frac{e^{ik_{\rm L}r}}{r} \int_S dy'dz'\, e^{-ik_{\rm L}(yy'+zz')/r}\,.} \qquad (9.162)$$

Consider for example a circular aperture of radius a. In this case the integral can be performed exactly in terms of the Bessel function J_1. Writing $y = \rho\cos\varphi, z = \rho\sin\varphi$, and similarly $y' = \rho'\cos\varphi', z' = \rho'\sin\varphi'$, we get

$$\begin{aligned}\int_S dy'dz'\, e^{-ik_{\rm L}(yy'+zz')/r} &= \int_0^a \rho' d\rho' \int_0^{2\pi} d\varphi'\, e^{-i(k_{\rm L}/r)\rho\rho'\cos(\varphi-\varphi')}\\ &= 2\pi \int_0^a \rho' d\rho'\, J_0(k_{\rm L}\rho\rho'/r)\\ &= \frac{2\pi a r}{k_{\rm L}\rho} J_1(k_{\rm L}\rho a/r)\,. \qquad (9.163)\end{aligned}$$

Writing $\rho/r = \sin\theta$ and recalling that $\lim_{u\to 0} J_1(u)/u = 1/2$, we see that the intensity of light, which is proportional to the squared modulus of the electric field, is distributed in the scattering angle θ as[19]

$$I(\theta) = I(0)\left[\frac{2J_1(k_{\rm L}a\sin\theta)}{k_{\rm L}a\sin\theta}\right]^2, \qquad (9.164)$$

A plot of the function $2J_1(x)/x$ is shown in Fig. 9.17. $I(\theta)$ has its first zero at $k_{\rm L}a\sin\theta \simeq 3.8$. Taking this as an estimate of the angular width $\Delta\theta$ of the beam we get (for $\lambda \ll a$) $\Delta\theta \simeq 3.8\lambda/a$, which is consistent with the uncertainty principle bound, but does not saturate it.

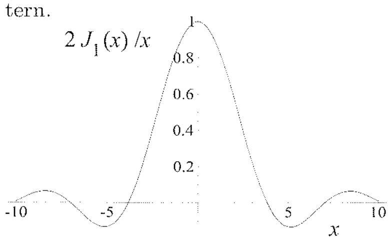

Fig. 9.17 The function $2J_1(x)/x$.

Propagation of Gaussian beams

Consider now a beam that, at $x = 0$, has a Gaussian profile in the transverse direction,

$$\mathcal{E}(x = 0; y, z) = \mathcal{E}_0 e^{-(y^2+z^2)/w_0^2}\,. \qquad (9.165)$$

Its profile at x generic can be computed by inserting this initial value into eqs. (9.158) and (9.159). The resulting integrals can be computed exactly, without resorting to the Fraunhofer approximation, using

$$\int_{-\infty}^{\infty} e^{-(1+ia^2)y^2} = \frac{\sqrt{\pi}}{(1+a^2)^{1/4}} \exp\left\{-\frac{i}{2}\arctan a\right\}, \qquad (9.166)$$

---

[19] This result was first derived by Airy in the 19th century, and this intensity distribution is known as the Airy pattern.

where a is a real constant. The result, written in terms of $E(x, y, z) = e^{ik_{\rm L}x}\mathcal{E}(x; y, z)$, is

$$\boxed{\begin{aligned}E(x, y, z) = &\frac{\mathcal{E}_0}{\sqrt{1 + x^2/b^2}}\, e^{-(y^2+z^2)/w^2(x)}\\ &\times \exp\left\{ik_{\rm L}\left[x + \frac{y^2+z^2}{2R(x)}\right] - i\arctan(x/b)\right\},\end{aligned}} \qquad (9.167)$$

where the *Rayleigh range* b is defined by

$$b = \frac{1}{2}k_{\rm L}w_0^2\,, \qquad (9.168)$$

the width $w(x)$ is given by

$$w(x) = w_0\sqrt{1 + x^2/b^2}\,, \qquad (9.169)$$

and the curvature radius $R(x)$ is

$$R(x) = x + \frac{b^2}{x}\,. \qquad (9.170)$$

This shows that a beam which at $x = 0$ has a Gaussian profile, remains Gaussian at all x, with a x-dependent width given by eq. (9.169). Observe that, since w_0 is the initial transverse size, b given in eq. (9.168) is the parameter that separates the Fresnel regime (at $x \ll b$) from the Fraunhofer regime (at $x \gg b$), compare with eq. (9.146). In agreement with the discussion above eq. (9.146), at $|x| \ll b$ we find that there is no appreciable widening of the beam, while at $|x| \gg b$ the width increases linearly, $w(x) \simeq w_0|x|/b$, as demanded by the uncertainty principle. Using the definition (9.168) of the Rayleigh range b, we get

$$w(x) \simeq \frac{|x|\lambda_{\rm L}}{\pi w_0}\,, \qquad (|x| \gg b)\,. \qquad (9.171)$$

Actually Gaussian beams saturate the uncertainty principle, i.e. they have the minimum possible spreading.

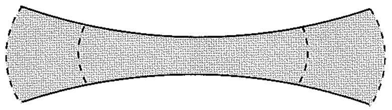

Fig. 9.18 A surface of constant intensity of the Gaussian beam (solid line) and surfaces of constant phase (dashed lines).

The term $\arctan(x/b)$ in eq. (9.167) is called the Gouy phase, and is an extra phase factor compared to the plane wave propagation. The surfaces of constant phase are obtained requiring that

$$k_{\rm L}\left[x + \frac{y^2+z^2}{2R(x)}\right] - \arctan(x/b)$$

be constant. For a typical GW interferometer, with $\lambda_{\rm L} = 1\,\mu$m and w_0 of order of a few cm, b is of order of several hundred meters. Thus, if we want to compute the surfaces of constant phase in a region close to a point on the optical axis, i.e. in a region with coordinates ($x = x_0 + \delta x, y = \delta y, z = \delta z$), with $\delta x, \delta y, \delta z$ of the order of a few cm, we can neglect the variation of $R(x)$ and of the Gouy phase, so at a given x_0 we simply have the condition

$$\delta x + \frac{\delta y^2 + \delta z^2}{2R(x_0)} = \text{constant}. \tag{9.172}$$

This equation describes a portion of spherical surface with radius $R(x_0)$, as we can check immediately by expanding the equation $x^2+y^2+z^2 = R^2$ around $x = R + \delta x, y = \delta y, z = \delta z$. Therefore the wavefronts of a Gaussian beam are spherical to an excellent approximation (as long as the transverse distances are much smaller than $b = O(10^2)$ m), and $R(x)$ is their curvature radius. The shape of the beam is therefore as shown in Fig. 9.18.[20] The characteristic length w_0, which determines the transverse size at $x = 0$, is called the *waist* of the beam.

When the beam bounces many times between two mirrors, we want to avoid that at each trip it widens further, as in Fig. 9.15. This can be obtained shaping the mirrors so that their surfaces match exactly surfaces of constant phase of the beam. For Gaussian beams we have seen that the wavefronts are spherical, so we must use spherical mirrors. When the expanding wavefront of a Gaussian beam reaches a spherical mirror located at a position x_0 and with radius of curvature $R(x_0)$, its direction of propagation is reversed, and the beam is focused back and converges toward the waist at $x = 0$, before re-expanding again for $x < 0$. If we have another spherical mirror at $x = -x_0$ the beam bounces back and forth between them, and at each reflection its wavefronts are forced to converge back toward the waist, as shown in Fig. 9.19, so the beam does not increment its transverse size at each bounce.

Gaussian beams have two advantages over other shapes. First, they have the minimum spreading compatible with the uncertainty principle. Second, their wavefronts are spherical, and mirrors with a spherical shape are easy to manufacture. For these reasons, they are the choice used in present GW interferometers. Thus, we can replace the scheme given in Fig. 9.12 with the more realistic scheme of Fig. 9.20. Alternatively, rather than using two spherical mirrors with the waist in the middle of the cavity, we can put a flat mirror in the position of the waist and, at a distance L, a spherical mirror with curvature radius $R = L + b^2/L$. Presently, the former option is used in LIGO and the latter in VIRGO. With the waist of the beam chosen in the middle of the cavity, the value of $w(x)$ at the position of the mirrors $x = \pm L/2$ is given by

$$w^2(\pm L/2) = w_0^2 + \frac{\bar{\lambda}_L^2 L^2}{w_0^2}. \tag{9.173}$$

In order to be able to use mirrors of manageable size, we want to have $w(\pm L/2)$ small. Minimizing eq. (9.173) with respect to w_0 we find the optimal value of the waist,

$$w_0^{\text{optimal}} = (\bar{\lambda}_L L)^{1/2}. \tag{9.174}$$

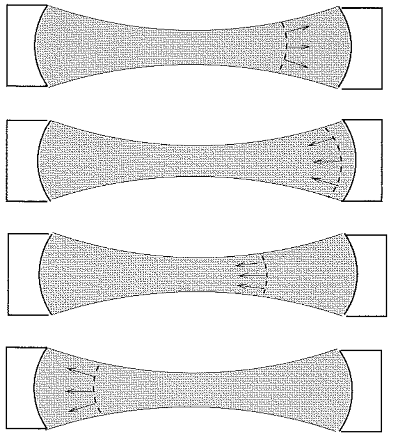

Fig. 9.19 A wavefront (dashed lines) that propagates toward a spherical mirror is reflected back and focused toward the waist. After passing the waist it expands again toward the other mirror.

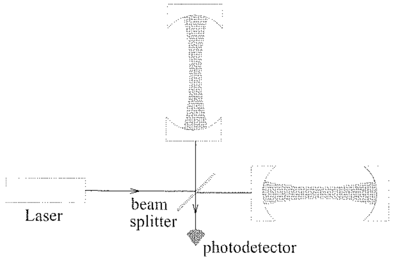

Fig. 9.20 The scheme of an interferometer with Fabry–Perot cavities, with Gaussian beams and spherical mirrors.

[20] The solution (9.167) holds also at $x < 0$; in this case both the term $k_L x$ and $R(x)$ in the exponential change sign, and the radius of curvature is as shown in the figure.

For arms of length $L = 4$ km and a wavelength of the laser light $\lambda_L \simeq 1.0\,\mu$m this gives $w_0 \simeq 2.5$ cm, to which corresponds a value $w(L/2) = (2\bar{\lambda}_L L)^{1/2} \simeq 3.6$ cm. A suitable mirror radius for such a beam can therefore be $O(10)$ cm.[21] Observe that, since the waist w_0 is much larger than the wavelength $\bar{\lambda}_L$, the paraxial approximation that we have used is well justified.

The Gaussian beams that we have considered are by definition solutions of the paraxial evolution equation (9.153), since we obtained them evolving an initial condition on the surface $x = 0$ with the paraxial propagator. Of course, we can also verify this by direct substitution in the equation. Actually, the Gaussian beam is just one of many possible solutions. As can be checked by direct substitution into eq. (9.153), there is a complete orthonormal set of solutions called the *Hermite–Gauss modes*, given by

$$u_{mn}(x,y,z) = \frac{c_{mn}}{\sqrt{1+x^2/b^2}}\, e^{-(y^2+z^2)/w^2(x)}\, H_m\!\left(\frac{y\sqrt{2}}{w(x)}\right) H_n\!\left(\frac{z\sqrt{2}}{w(x)}\right) \times \exp\left\{ik_L\left[x + \frac{y^2+z^2}{2R(x)}\right] - i(m+n+1)\arctan(x/b)\right\}, \tag{9.175}$$

where c_{mn} are normalization constants and $H_n(\xi)$ are the Hermite polynomials, defined by

$$H_n(\xi) = e^{\xi^2}\left(-\frac{d}{d\xi}\right)^n e^{-\xi^2}. \tag{9.176}$$

In particular, $H_0(\xi) = 1$, $H_1(\xi) = 2\xi$, and $H_2(\xi) = 4\xi^2 - 2$. For these modes, both the electric and magnetic fields are transverse to the propagation direction, just as plane wave in free space, so they are also denoted as TEM$_{mn}$ modes. Comparing with eq. (9.167) we see that the Gaussian beam is just the mode TEM$_{00}$. In Figs. 9.21–9.23 we show the intensity $|u_{mn}|^2$ of the modes TEM$_{00}$, TEM$_{01}$ and TEM$_{11}$. Alternatively, one can use as a basis the so-called Laguerre–Gauss modes LG$_{mn}$, which are written in terms of Laguerre polynomials. The fundamental mode LG$_{00}$ is again the Gaussian beam.

Since the Gouy phase for the mode TEM$_{mn}$ is $(m+n+1)\arctan(x/b)$, see eq. (9.175), the resonance condition in a FP cavity depends on (m,n). The laser emits predominantly in the TEM$_{00}$ mode, with a contamination typically less than 10% from higher modes (mostly TEM$_{01}$ and TEM$_{10}$). To eliminate these residual higher modes, which would not be resonant and would just produce noise, before sending it to the beam splitter the laser beam is sent into a Fabry–Perot cavity operated in transmission, called the *mode-cleaner*. Since the Gouy phase for the mode TEM$_{mn}$ depends on (m,n), we can choose the length of the mode cleaner so that only the $(0,0)$ mode is in resonance and is efficiently transmitted.

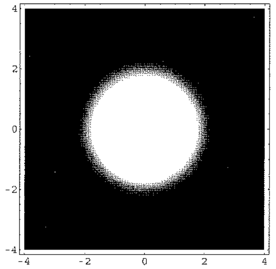

Fig. 9.21 The intensity of the mode TEM$_{00}$ as a function of the transverse variables (y,z), at a given x. (in units such that $w(x) = \sqrt{2}$).

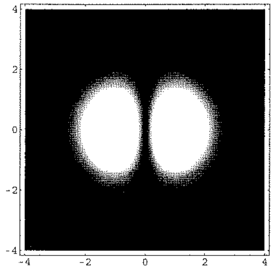

Fig. 9.22 The same as Fig. 9.21, for the mode TEM$_{01}$.

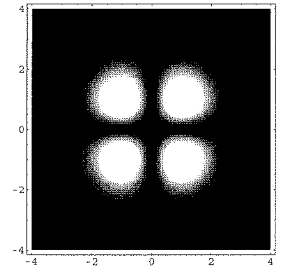

Fig. 9.23 The same as Fig. 9.21, for the mode TEM$_{11}$.

[21] A small spot allows us to keep down the mirror size. However, it also results in large intensity gradients, in region of high intensity of the electromagnetic field, inducing thermal deformations of the mirrors that must be compensated. An alternative possibility, that has been studied for advanced interferometers, is the use of so-called "mesa beams", i.e. beams with a flat profile, which average more effectively over these thermoelastic fluctuations, see Bondarescu and Thorne (2006).

9.3.2 Detection at the dark fringe

Michelson interferometer

We have seen that the passage of a GW in an interferometer, whether of the simple Michelson type or with Fabry–Perot cavities in the arms, produces a phase shift $\Delta\phi_{\rm gw}(t)$. We now ask how to extract this phase from the output of the detector. The issue, as we will discuss in this section, is quite non-trivial. The origin of the problem can be seen as follows. We consider first for simplicity a Michelson interferometer. We saw in eq. (9.32) that the power at its output is given by $P(\phi) = P_0 \sin^2\phi$ where $\phi = \phi_0 + \Delta\phi_{\rm gw}(t)$, and ϕ_0 is a phase that can be adjusted at will by the experimenter. A plot of $P(\phi)/P_0$ is shown in Fig. 9.24. Naively, one might think from this figure that the best working point for the interferometer is at $\phi_0 = \pi/4$, since there the derivative $\partial P/\partial\phi_0$ is maximum, and the sensitivity to a small displacement $\phi_0 \to \phi_0 + \Delta\phi_{\rm gw}(t)$ due to the passage of a GW is highest. Unfortunately, such a strategy would be doomed to failure. In fact, at this working point we are also very sensitive to fluctuations in the power P_0 of the laser. Since all that we measure is the power $P = P_0 \sin^2\phi$ at the photodetector, it is impossible to tell whether a given variation in the measured power is due a variation $\phi_0 \to \phi_0 + \Delta\phi_{\rm gw}(t)$ induced by the passage of a GW, or to a variation $P_0 \to P_0 + \Delta P_0(t)$ due to a fluctuation in the laser power. In particular, a GW with frequency $f_{\rm gw} = O(10^2\text{–}10^3)$ Hz induces variations in the power P with a frequency $f = 2f_{\rm gw}$, which therefore must be compared with the power fluctuations of the laser in the same frequency range. With present lasers, the latter turns out to be much larger than the signal that we expect from GWs.

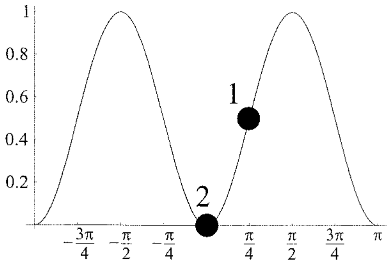

Fig. 9.24 The power $P(\phi)/P_0$. The naive working point is marked as 1, and the dark fringe as 2.

From a more general point of view, whenever we are looking for very small effects a sound experimental strategy is to build a *null instrument*, that is an instrument that, when the signal is absent, records a zero output. This makes the instrument insensitive to calibration uncertainties that would otherwise overwhelm the tiny signal that we are searching. A prototype of a null instrument is the Dicke radiometer that we discussed in Note 74 on page 412. At the naive operation point marked as 1 in Fig. 9.24, the interferometer is not a null instrument. Even in the absence of a GW, the photodetector measures a large power. In this state, small variations in the power due to GWs should be read against this large DC contribution, and would be overwhelmed by its fluctuations.

This suggests that the best working point should be the dark fringe, marked as the point 2 in Fig. 9.24. There the output in the absence of GWs is zero, and we are insensitive to fluctuations in the laser power. Unfortunately, at the dark fringe not only $P = 0$, but even $\partial P/\partial\phi = 0$. Since $\Delta\phi_{\rm gw} = O(h)$, this means that at the dark fringe the change in the output power induced by GWs is $\Delta P = O(h^2)$. Given that we expect GWs with amplitude h at most $O(10^{-21})$, an effect quadratic in h is of course invisible. So, apparently the choice is between operation points where the response of the interferometer is linear in h, but we have a large DC contribution whose fluctuations overwhelm the signal, and an operation point where we have no DC contribution, but no sensitivity to GWs either.

There is however a very elegant way out of this dilemma. The idea is to apply a *phase modulation* to the input laser light.[22] This can be obtained by passing the incident beam through a Pockels cell, which is a crystal or a block of dielectric material whose index of refraction depends on an applied electric field, $E_{\rm appl} = |E_{\rm appl}| \cos\Omega_{\rm mod}t$. The speed of the response that can be obtained with appropriate materials is quite high, and the index of refraction oscillates with the frequency $f_{\rm mod} = \Omega_{\rm mod}/(2\pi)$, for values of $f_{\rm mod}$ up to tens of MHz. Passing through a material with a time-varying index of refraction, the laser beam acquires a time-varying phase, so the beam which reaches the beam-splitter has the form

$$E_{\rm in} = E_0 e^{-i(\omega_{\rm L}t + \Gamma \sin\Omega_{\rm mod}t)}, \tag{9.177}$$

where Γ is called the modulation index, or the modulation depth. This expression can be expanded in Fourier modes as

$$E_{\rm in} = E_0[J_0(\Gamma)e^{-i\omega_{\rm L}t} + J_1(\Gamma)e^{-i(\omega_{\rm L}+\Omega_{\rm mod})t} - J_1(\Gamma)e^{-i(\omega_{\rm L}-\Omega_{\rm mod})t} + \ldots], \tag{9.178}$$

where J_n are Bessel functions and the dots denote terms with frequencies $\omega_{\rm L} \pm n\Omega_{\rm mod}$, with $n = 2, 3, \ldots$. For $\Gamma \ll 1$ this expression can be simplified using $J_0(\Gamma) \simeq 1 - (\Gamma^2/4)$ and $J_1(\Gamma) \simeq \Gamma/2$. (In the limit $\Gamma \ll 1$ this expansion is obtained more simply expanding directly eq. (9.177) in powers of Γ). Therefore, the effect of the phase modulation is to generate sidebands.[23] For small Γ, higher sidebands are suppressed by higher powers of Γ, so we will limit ourselves to the carrier, which has frequency $\omega_{\rm L}$ and wavenumber $k_{\rm L} = \omega_{\rm L}/c$, and to the first two sidebands, with frequencies

$$\omega_{\pm} = \omega_{\rm L} \pm \Omega_{\rm mod}, \tag{9.179}$$

and wavenumbers

$$k_{\pm} = \frac{\omega_{\pm}}{c} = 2\pi\left(\frac{1}{\lambda_{\rm L}} \pm \frac{1}{\lambda_{\rm mod}}\right). \tag{9.180}$$

Consider now what happens to the carrier and to the sidebands in a Michelson interferometer with arms of length L_x and L_y. For the carrier the incoming electric field has amplitude $E_0 J_0(\Gamma)$ so, from the discussion in Section 9.1, the electric field at the output of the interferometer is

$$(E_{\rm out})_c = \frac{1}{2}(r_1 e^{2ik_{\rm L}L_x} - r_2 e^{2ik_{\rm L}L_y})\, E_0 J_0(\Gamma) e^{-i\omega_{\rm L}t}, \tag{9.181}$$

where r_1, r_2 are the reflectivities of the two end-mirrors. Taking perfectly reflecting mirrors, $r_1 = r_2 = -1$, we have

$$\begin{aligned}(E_{\rm out})_c &= -iE_0 J_0(\Gamma)\, e^{-i\omega_{\rm L}t + ik_{\rm L}(L_x+L_y)} \sin[k_{\rm L}(L_x - L_y)] \qquad (9.182)\\ &= -iE_0 J_0(\Gamma)\, e^{-i\omega_{\rm L}t + ik_{\rm L}(L_x+L_y)} \sin\left[2\pi\frac{L_x - L_y}{\lambda_L}\right],\end{aligned}$$

[22] Another possible solution would be to control so well the laser fluctuations, that a detection scheme of the type discussed above becomes possible (typically at a working point which is slightly displaced from the dark fringe). This solution is under investigation for Advanced LIGO.

[23] For $\lambda_{\rm L} = 1\,\mu$m we have $\omega_{\rm L}/(2\pi) \simeq 300$ THz, while typically $\Omega_{\rm mod}/(2\pi) \simeq 30$ MHz, so $\Omega_{\rm mod} \ll \omega_{\rm L}$.

compare with eq. (9.4). For the sidebands the calculation is the same, but of course now $k_{\rm L}$ is replaced by $k_\pm$ and $\omega_{\rm L}$ by $\omega_\pm$, and the amplitude of the incident field is $\pm J_1(\Gamma)E_0$. Thus, writing $L_x - L_y = \Delta L$, the electric field of the sidebands at the output is

$$\begin{aligned}(E_{\rm out})_\pm &= \mp iE_0 J_1(\Gamma)\, e^{-i\omega_\pm t + ik_\pm(L_x+L_y)} \sin(k_\pm \Delta L) \qquad (9.183)\\ &= \mp iE_0 J_1(\Gamma)\, e^{-i\omega_\pm t + ik_\pm(L_x+L_y)} \sin\left[2\pi\left(\frac{\Delta L}{\lambda_{\rm L}} \pm \frac{\Delta L}{\lambda_{\rm mod}}\right)\right].\end{aligned}$$

Now comes the crucial point. If we take $L_x = L_y$, both the carrier and the sidebands are on the dark fringe, $(E_{\rm out})_c = (E_{\rm out})_\pm = 0$. However, instead of choosing $L_x = L_y$, we can set $L_x - L_y$ equal to an integer number of laser wavelengths, i.e. $\Delta L = n\lambda_{\rm L}$. Then, as far as the carrier is concerned, we are still on the dark fringe, while the sidebands are no longer on the dark fringe. Rather,

$$(E_{\rm out})_\pm = -iE_0 J_1(\Gamma)\, e^{-i\omega_\pm t + ik_\pm(L_x+L_y)} \sin(2\pi\Delta L/\lambda_{\rm mod})\,. \qquad (9.184)$$

This choice of asymmetric arms is called the *Schnupp asymmetry*. Consider now what happens when a GW arrives, taking for simplicity a plus polarization with optimal direction, and $\omega_{\rm gw}L/c \ll 1$. Then eq. (9.31) gives $L_x \to L_x + hL_x/2$ and $L_y \to L_y - hL_y/2$, so

$$(L_x - L_y) \to (L_x - L_y) + L\,h(t)\,, \qquad (9.185)$$

where $L = (L_x + L_y)/2$ and, to lowest order in $\omega_{\rm gw}L/c$, we could replace $h(t - L_x/c)$ and $h(t - L_y/c)$ by $h(t)$. Then we see from eq. (9.182) that the electric field of the carrier is shifted from the value $(E_{\rm out})_c = 0$ on the dark fringe to the value

$$(E_{\rm out})_c = -iE_0 J_0(\Gamma)\, e^{-i\omega_{\rm L} t + 2ik_{\rm L}L}\, k_{\rm L} L h(t)\,. \qquad (9.186)$$

This is linear in h and, if this were the total electric field, the power $|(E_{\rm out})_c|^2$ would be quadratic in h, as we saw above. However, now we also have the field of the sidebands, and the total electric field is

$$(E_{\rm out})_{\rm tot} = (E_{\rm out})_c + (E_{\rm out})_+ + (E_{\rm out})_-\,. \qquad (9.187)$$

From eq. (9.184), in the absence of GW we have

$$\begin{aligned}(E_{\rm out})_+ + (E_{\rm out})_- = -2iE_0 J_1(\Gamma)\, e^{-i\omega_{\rm L} t + 2ik_{\rm L}L} \qquad (9.188)\\ \times \sin(2\pi\Delta L/\lambda_{\rm mod})\, \cos(\Omega_{\rm mod}t - \alpha)\,,\end{aligned}$$

where $\alpha = 4\pi L/\lambda_{\rm mod}$ is a phase. In the presence of GWs this is modified by the fact that $\Delta L \to [1 + O(h)]\Delta L$. However, here we can neglect the term $O(h)$ because, as we will see below, it is the term $O(1)$ that combines with the carrier, giving a term proportional to h in $|(E_{\rm out})_{\rm tot}|^2$ that will encode the GW signal.[24] Thus, the total electric field at the output, in the presence of GWs, is

$$\begin{aligned}(E_{\rm out})_{\rm tot} = -iE_0 e^{-i\omega_{\rm L} t + 2ik_{\rm L}L}[J_0(\Gamma)k_{\rm L}Lh(t) \qquad (9.189)\\ +2J_1(\Gamma)\, \sin(2\pi\Delta L/\lambda_{\rm mod})\, \cos(\Omega_{\rm mod}t - \alpha)]\,.\end{aligned}$$

---

[24] Furthermore, the term $O(h)$ is multiplied here by ΔL, and $\Delta L \ll L$.

When we compute $|(E_{\rm out})_{\rm tot}|^2$ we therefore have three terms. (1) The squared modulus of the first term, which is $O(h^2)$, and therefore unobservable. (2) The squared modulus of the second, which is independent of h, and proportional to

$$\cos^2(\Omega_{\rm mod}t - \alpha) = \frac{1}{2}[1 + \cos(2\Omega_{\rm mod}t - 2\alpha)]\,. \qquad (9.190)$$

Therefore it is the sum of a DC term and a term which oscillates with a frequency $2\Omega_{\rm mod}$. (3) Finally we have the mixed term, i.e. the beatings between the carrier and the sidebands, which is

$$4E_0^2 J_0(\Gamma)J_1(\Gamma)k_{\rm L}Lh(t)\sin(2\pi\Delta L/\lambda_{\rm mod})\, \cos(\Omega_{\rm mod}t - \alpha)\,. \qquad (9.191)$$

This term is linear in h and oscillates with a frequency $\Omega_{\rm mod}$.[25] Therefore in the output we have a term linear in h, even if the carrier is on the dark fringe. This term can be extracted from the total output $|(E_{\rm out})_{\rm tot}|^2$ using a mixer, which is a non-linear device which takes at its input two voltages, and produces an output voltage proportional to the product of the two input voltages. Then, we can multiply the voltage produced by $|(E_{\rm out})_{\rm tot}|^2$ in the photodetector by a voltage $V_{\rm osc}\cos(\Omega_{\rm mod}t - \alpha)$. The time-averaged output of the mixer selects the part of $|(E_{\rm out})_{\rm tot}|^2$ which oscillates as $\cos(\Omega_{\rm mod}t - \alpha)$, while the DC part and the part oscillating as $\cos(2\Omega_{\rm mod}t - 2\alpha)$ average to zero. The result (9.191) can be optimized choosing $\Delta L/\lambda_{\rm mod} = m + 1/4$, with m any integer.

In this way we have an output which is linear in h, and is insensitive to the power fluctuations of the carrier, which is on the dark fringe. In principle, we are still sensitive to power fluctuations of the laser because the sidebands are not on the dark fringe. However, apart from the fact that the electric field of the sidebands is smaller since it is $O(\Gamma)$, the crucial point is that now the signal has been encoded in a term which oscillates as $\cos(\Omega_{\rm mod}t - \alpha)$, so it must no longer compete with the fluctuations of the laser at a frequency $f_{\rm gw}$ of the GWs that we are searching, but rather with the fluctuations of the laser at a frequency $f_{\rm mod}$ which is much higher, typically 30 MHz. The power fluctuations of the laser is an example of a $1/f$ noise (see page 339), and at high frequencies it is small. In conclusion, we have achieved two results with this technique: (1) We are using the interferometer as a null instrument, since when $h = 0$ the output of the mixer, i.e. the term in the output power oscillating as $\cos(\Omega_{\rm mod}t - \alpha)$, vanishes. (2) The signal is linear in the GW amplitude and is encoded into a high-frequency term, so that it must now compete with much smaller $1/f$ noise.

Interferometers with Fabry–Perot cavities

We now discuss how to apply this technique to an interferometer with Fabry–Perot cavities in the arms. In this case we consider two FP cavities both with the same length L, and the Schnupp asymmetry consists in the fact that the distances of their respective input mirrors (i.e. the mirror first encountered by the beam) from the beam-splitter are l_x and l_y respectively, with $l_x \neq l_y$.

---

[25] More precisely, since $h(t)$ is proportional to $\cos\omega_{\rm gw}t$, it oscillates at frequencies $\Omega_{\rm mod} \pm \omega_{\rm gw}$. Since $f_{\rm mod} = O(10)$ MHz and $f_{\rm gw} < O(1)$ kHz, $\omega_{\rm gw} \ll \Omega_{\rm mod}$.

The field at the output of the photodetector can be computed using eq. (9.70), which states that, as far as the reflected field is concerned, for light with wavenumber k a FP cavity is equivalent to a mirror with a reflectivity

$$\mathcal{R}(k) = \frac{r_1 - r_2(1-p_1)e^{2ikL}}{1 - r_1 r_2 e^{2ikL}} \,. \tag{9.192}$$

Again we modulate the laser light with a Pockels cell, so the light incident on the beam-splitter is composed of a carrier at the laser frequency $\omega_{\rm L}$ and two sidebands at $\omega_{\rm L} \pm \Omega_{\rm mod}$. We choose the cavity length L so that the carrier is resonant. The modulation frequency $f_{\rm mod} = \Omega_{\rm mod}/2\pi$ is much larger than the width of the resonances of the FP cavities. For instance, for $L = 4$ km and $\mathcal{F} = 200$, eqs. (9.82) and (9.83) give a width at half maximum $\delta f = O(200)$ Hz, while the modulation frequency is in the MHz region. Therefore, the modulation frequency $\Omega_{\rm mod}$ can be chosen so that the sidebands are not resonant, and fall roughly in between resonant peaks. From eqs. (9.99) and (9.100) we see that, for an overcoupled cavity, setting $r_2 = 1$, at the resonance $\mathcal{R} = -(1-\sigma)$, so the phase $\phi \equiv \arg(\mathcal{R})$ is equal to π. In contrast, for a generic value of $2kL$ far from the resonance (using $r_2 = 1$ and $\sigma \ll 1$), eq. (9.192) gives $\mathcal{R} = 1 + O(\sigma^2)$, so in particular $\arg(\mathcal{R}) = 0$ (mod 2π), as we see also from Fig. 9.11. Thus, as far as the reflected field is concerned, a FP cavity is equivalent to a mirror with a reflectivity $\mathcal{R}$ which is different for the carrier and for the sidebands,

$$\mathcal{R}(k) \simeq \begin{cases} -(1-\sigma) & \text{(if } k = k_{\rm L}) \\ +1 & \text{(if } k \text{ is not close to } k_{\rm L}). \end{cases} \tag{9.193}$$

The total electric field at the photodetector is the superposition of the field that propagates in the x arm for a length l_x, and is then reflected by the Fabry–Perot cavity with a reflection coefficient $\mathcal{R}_x$, and of the field that propagates in the y arm for a length l_y, and is then reflected by the Fabry–Perot cavity, with a reflection coefficient $\mathcal{R}_y$. In the absence of GWs we have $\mathcal{R}_x = \mathcal{R}_y = \mathcal{R}$, with the appropriate value of $\mathcal{R}$ depending on whether we consider the carrier or the sidebands. Then, as in eq. (9.181), the field at the output is

$$\begin{aligned} E_{\rm out} &= \frac{1}{2}(\mathcal{R}_x e^{2ikl_x} - \mathcal{R}_y e^{2ikl_y})\, E_{\rm in} e^{-i\omega t} \\ &= i\mathcal{R} E_{\rm in} e^{-i\omega t + 2ikl} \sin(k\Delta l)\,, \end{aligned} \tag{9.194}$$

where $2l = l_x + l_y$, $\Delta l = l_x - l_y$, and (k, ω) are equal to $(k_{\rm L}, \omega_{\rm L})$ for the carrier and to $(k_\pm, \omega_\pm)$ for the sidebands. Thus, for the carrier we have

$$(E_{\rm out})_c = -i(1-\sigma)E_0 J_0(\Gamma) e^{-i\omega_{\rm L} t + 2ik_{\rm L} l} \sin(2\pi\Delta l/\lambda_{\rm L})\,, \tag{9.195}$$

and for the sidebands

$$(E_{\rm out})_\pm = \pm i E_0 J_1(\Gamma)\, e^{-i\omega_\pm t + 2ik_\pm l} \sin\left[2\pi\left(\frac{\Delta l}{\lambda_{\rm L}} \pm \frac{\Delta l}{\lambda_{\rm mod}}\right)\right]. \tag{9.196}$$

Just as we did for the Michelson interferometer, we choose as working point the dark fringe of the carrier, that is we choose l_x and l_y so that the Schnupp asymmetry Δl is equal to an integer times $\lambda_{\rm L}$, and also $\Delta l/\lambda_{\rm mod} = m + 1/4$ for some integer m, so that $\sin(2\pi\Delta l/\lambda_{\rm mod}) = 1$. Thus, in the absence of GWs, $(E_{\rm out})_c = 0$ while

$$(E_{\rm out})_+ + (E_{\rm out})_- = 2iE_0 J_1(\Gamma)\, e^{-i\omega_{\rm L} t + 2ik_{\rm L} l} \cos(\Omega_{\rm mod} t - \alpha)\,, \tag{9.197}$$

with $\alpha = 4\pi l/\lambda_{\rm mod}$. Consider now what happens in the presence of a GW, as usual with optimal orientation and $\omega_{\rm gw} L/c \ll 1$. The effect of the GW is to change the reflectivities $\mathcal{R}_x$ and $\mathcal{R}_y$ of the Fabry–Perot cavities. Consider first the carrier. The passage of the GW induces a phase shift $\Delta\phi_x$ in the reflected field given in eq. (9.102), so we get (for $\sigma \ll 1$)

$$\mathcal{R}_x(k_{\rm L}) = -(1-\sigma)e^{i\Delta\phi_x}\,, \tag{9.198}$$

with

$$\Delta\phi_x = \frac{2\mathcal{F}}{\pi}\, k_{\rm L} L h(t)\,. \tag{9.199}$$

For the cavity along the y arm we have an opposite phase shift, $\Delta\phi_y = -\Delta\phi_x$, so $\mathcal{R}_y(k_{\rm L}) = -(1-\sigma)e^{-i\Delta\phi_x}$. Then eq. (9.194) gives

$$\begin{aligned} (E_{\rm out})_c &= -\frac{1}{2}(1-\sigma)(e^{i\Delta\phi_x} e^{2ik_{\rm L} l_x} - e^{-i\Delta\phi_x} e^{2ik_{\rm L} l_y}) E_{\rm in} e^{-i\omega_{\rm L} t} \\ &= -i(1-\sigma)E_0 J_0(\Gamma) e^{-i\omega_{\rm L} t + 2ik_{\rm L} l} \sin\left[2\pi\frac{\Delta l}{\lambda_{\rm L}} + \Delta\phi_x\right] . \end{aligned} \tag{9.200}$$

On the dark fringe $\Delta l/\lambda_{\rm L} = n$ and $\sin\left[2\pi\frac{\Delta l}{\lambda_{\rm L}} + \Delta\phi_x\right] = \sin(\Delta\phi_x) \simeq \Delta\phi_x$. Thus, in the presence of a GW the electric field of the carrier at the photodetector shifts from the value $(E_{\rm out})_c = 0$ to the value

$$(E_{\rm out})_c = -i(1-\sigma)E_0 J_0(\Gamma) e^{-i\omega_{\rm L} t + 2ik_{\rm L} l}\, \frac{2\mathcal{F}}{\pi}\, k_{\rm L} L h(t)\,. \tag{9.201}$$

As we already saw for the Michelson interferometer, the modification of the electric field of the sidebands due to the GWs is negligible, since it gives a corrections $1 + O(h)$, but it is the term $O(1)$ which, beating against the term $O(h)$ in the carrier, gives a term linear in h in the output. In conclusion, we can write the total (carrier plus sidebands) electric field at the output as

$$\begin{aligned} (E_{\rm out})_{\rm tot} &= -2iE_0 e^{-i\omega_{\rm L} t + 2ik_{\rm L} l} \\ &\quad \times \left[(1-\sigma)J_0(\Gamma)\frac{\mathcal{F}}{\pi}\, k_{\rm L} L h(t) - J_1(\Gamma)\cos(\Omega_{\rm mod} t - \alpha)\right] . \end{aligned} \tag{9.202}$$

The situation is now the same that we already discussed for a Michelson interferometer: taking the modulus squared, the term which oscillates as $\cos(\Omega_{\rm mod} t - \alpha)$ is linear in h and is demodulated with a mixer. We therefore have an output that is linear in $h(t)$ even if the carrier is on the dark fringe, and is encoded in a term which oscillates at the frequency $\Omega_{\rm mod}$, so $1/f$ noise such as laser power fluctuations are small. This procedure is a special case of the Pound–Drever–Hall locking, see Section 9.3.4.

9.3.3 Basic optical layout

We can now complete the description of a realistic GW interferometer. One further improvement with respect to the scheme that we have discussed is the *power recycling*. The basic observation is that, since we have chosen as working point the dark fringe for the carrier, in the absence of GWs no light at all emerges from the beam-splitter in the direction of the photodetector, at the carrier frequency. This means that all the light at frequency ω_L that circulates in the arms is eventually reflected by the beam-splitter back toward the laser and, in this sense, is wasted. When we discuss the noise sources in the next section, and in particular the shot noise, we will see that we want to have the highest possible laser intensity circulating in the arms. However, the power of a continuous (and very stable) laser is currently limited to $O(10)$ watts, which could become $O(100)$ W in the near future. To increase the power circulating in the interferometer, the idea is to "recycle" the light that comes back toward the laser, placing a mirror (the power-recycling mirror) that reflects the light back toward the beam-splitter. As far as the light reflected toward the laser is concerned, we can model the whole interferometer as an equivalent mirror, with a reflectivity that accounts for the total reflected field. The addition of the power-recycling mirror between the laser and the beam-splitter creates a new Fabry–Perot cavity, made of the power-recycling mirror and the "equivalent interferometer mirror". If this cavity is arranged so that it is resonant for the input laser light, the total intensity of the light that circulates in the interferometer is enhanced. Indeed, in this way a gain of $O(100)$ can be obtained (the maximum gain that can be reached is inversely proportional to the losses inside the interferometer), so the power circulating between the power-recycling mirror and the beam splitter raises to about 1 kW. Inside the Fabry–Perot cavities in the arms, this power increases further because it is resonant, and in initial LIGO and VIRGO it reaches a value of order 15 kW.

A second feature of a real interferometer is an output mode cleaner. Even if the initial beam has been accurately prepared in the TEM_{00} mode thanks to the input mode cleaner, various imperfections in the mirrors, as well as misalignments, regenerate higher modes inside the interferometer. These higher modes are not on the dark fringe, and therefore simply produce a noise that lower the contrast at the output. The output mode cleaner, placed between the beam-splitter and the photodetectors, filters out these higher modes, enhancing the contrast and therefore the sensitivity.

Putting together all these elements, we arrive at the optical layout shown in Fig. 9.25 where, for definiteness, we have used the parameters of VIRGO. The laser, a continuous Nd:Yag with wavelength $\lambda_L = 1.064\,\mu$m, provides 20 W of power. The laser beam passes through an electro-optic modulator, i.e. a Pockels cell, which generates sidebands at $\Omega_{\rm mod}/(2\pi) = 6.2$ MHz. The beam is then passed through the input mode cleaner. This is a long cavity with very high finesse, and a triangular shape that forbids reflection back toward the laser. The beam that comes out of the input mode cleaner is very nearly a TEM_{00} mode, both in the carrier and in the sidebands. It is transmitted through the power recycling mirror and enters the interferometer. The Schnupp asymmetry is realized choosing $l_x \simeq 6.4$ m and $l_y \simeq 5.5$ m for the distances between the beam splitter and the input mirrors of the two Fabry–Perot cavities. After going back and forth in the Fabry–Perot cavities, with a length of 3 km and a finesse $\mathcal{F} = 50$, the beams are recombined on the beam-splitter. Since we work on the dark fringe, at the beam-splitter the carrier is entirely reflected back toward the laser, and then finds the power-recycling mirror, that sends it back to the interferometer. When the carrier is displaced from the dark fringe, for instance because of the passage of a GW, the beating between the carrier and the sidebands goes toward the photodetector. It first passes through the output mode cleaner, a single crystal of 3.6 cm, where again makes a triangular path, and then goes to an array of photodetectors, and it is finally demodulated and detected.[26]

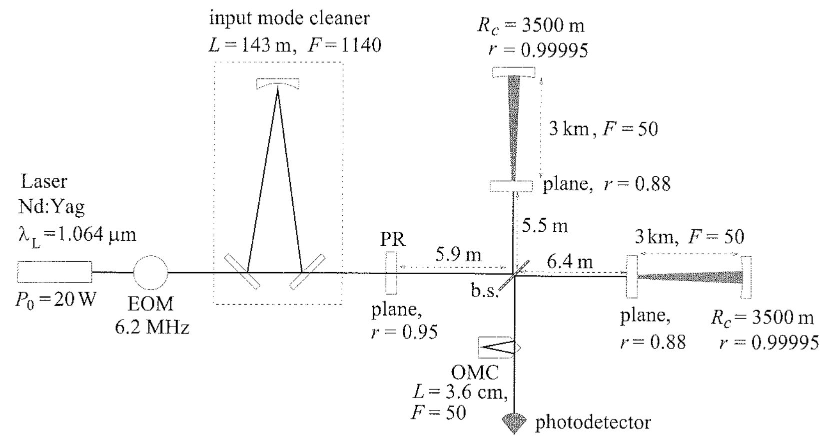

Fig. 9.25 The basic layout of a GW interferometer. EOM = Electro-optic modulator (Pockels cell); PR = power recycling mirror; OMC = output mode cleaner; b.s. = beam splitter. The curvature radius R_c and reflectivity r of the various mirrors are indicated. For definiteness, we used the values for the initial VIRGO interferometer.

9.3.4 Controls and locking

This section is slightly technical, but is meant to give at least a flavor of the problems that must be overcome to turn the beautiful theoretical idea of a GW interferometer into a working instrument.

The scheme that we have discussed above reaches its high sensitivity because the laser light is resonant in the Fabry–Perot cavities. On resonance, a FP cavity is extremely sensitive to changes in its length L, but as soon as we move away from the resonance, it becomes "dead", and the phase of the reflected field loses essentially any dependence on

[26] Figure 9.25 is still somewhat simplified. For instance, there are also lenses that are used to match the laser beam into the mode cleaner. A Faraday isolator is used to protect the laser from back-tracking light from the interferometer. A mode-matching telescope is used to blow the input laser beam, which has an initial transverse size of just a few millimeters, to the waist appropriate for the Fabry–Perot cavities which, as we have seen, is rather of order 2–3 cm. Further mirrors are used to pick up signals that are needed for control purposes.

L, see Fig. 9.10. This means that the mirrors of the FP cavity must be hold still, and in the right position, so that $k_{\rm L}L = \pi n$ for some integer n. To estimate the precision needed we observe from eq. (9.81) that the half-width of the resonance peak, as a function of L at fixed $k_{\rm L}$, is reached if L shifts from the value that fulfills the resonance condition to a value $L + \delta L$, with

$$\delta L = \frac{\lambda_{\rm L}}{4\mathcal{F}} . \tag{9.203}$$

(Compare with eqs. (9.83) and (9.84), where we computed the full width at half maximum in $\omega_{\rm L}$, at fixed L.) With a finesse $\mathcal{F} = O(200)$ this means that we need to keep the length L of the Fabry–Perot cavities fixed, within a precision better than $\delta L \sim 10^{-3}\lambda_{\rm L}$. Similarly, the power-recycling technique that we have discussed allows us to gain a factor $O(100)$ in laser power, but again the power-recycling mirror must be located in a precise position, in order to satisfy the resonance condition in the power-recycling cavity, i.e. in the cavity made by the power-recycling mirror and the equivalent interferometer mirror. Again, this must hold to a precision much smaller than $\lambda_{\rm L}$. Finally, our detection scheme requires that the interferometer be on the dark fringe, again within a small fraction of wavelength. Typically, a value $\delta L \sim (10^{-6}\text{–}10^{-4})\lambda_{\rm L}$ is required for good performances. With $\lambda_{\rm L} = 1\,\mu$m, this means that the relative position of the mirrors must be kept fixed, at a distance L of order a few kms, within a precision

$$\delta L \sim (10^{-12}\text{–}10^{-10})\,\text{m}, \tag{9.204}$$

which is less than the size of an atom! Last but not least, all these lengths are measured with respect to $\lambda_{\rm L}$, so we also need a laser whose frequency is stabilized to great precision. At first sight, the idea of controlling the length of a 4-km cavity down to an accuracy of 10^{-10} m might seem preposterous. Indeed, it is here that a large part of the complexity of GW interferometers resides. However, by now this is routinely achieved in the large GW interferometers, and it is quite interesting to understand how this is possible.

First of all, one could make the possibly naive remark that a mirror does not have a smooth surface down to 10^{-10} m, since at this level we resolve the individual atoms, and even more so at 10^{-12} m; thus, one might object that the notion of the length L of the cavity is not even well defined down to these scales. However, we must keep in mind that the laser beam at the mirror locations has a transverse size of a few centimeters. This means that what the laser beams actually senses is the position of the surface of the mirror, *averaged over a macroscopic scale*, of order a few cms. Thus, the individual atomic fluctuations cancel out, at least to a first approximation[27] and, in this averaged sense, the notion of the length L of the cavity *is* well defined, even down to such small scales. This is a simple but fundamental point to keep in mind to understand the statement that interferometers (or, as we saw in Chapter 8, resonant bars) are finally able to detect displacements which are much smaller than the size of a nucleus.

[27] Of course, any imperfection in the mirrors will create noise, such as scattered light in the interferometer, so their micro-roughness cannot exceed too much the figure $O(10^{-10})$ m found above. The mirrors of LIGO and VIRGO are polished so that their rms micro-roughness is about 0.5Å, that is 50 times larger than 10^{-10} m.

Another simple but important conceptual point is that, actually, we do not need to know the value of the length L of a FP cavity down to a precision 10^{-10} m. All that we need, in order to have a FP cavity which works properly, is that it is on one of its resonances, i.e. $2k_{\rm L}L = 2\pi n$, or $L = \lambda_{\rm L}n/2$, for some integer n. Since $2L/\lambda_{\rm L} = O(10^{10})$, the corresponding value of n is very large, but we do not need to know it. All that we want is that the FP cavity be on some resonance, corresponding to some unspecified value of n, and does not move away from it by more than $\delta L \sim 10^{-4}\lambda_{\rm L}$. Once the two FP cavities in the arms are resonant, we must arrange their relative position so that the interferometer is on some dark fringe. Again, we do not need to know on which one.

So, what we need is to "trap", or lock, each FP cavity in some of its resonances, and to lock the interferometer on some dark fringe. The general strategy is the one common to all *feedback control systems*. In general terms, this consists of a sensor and an actuator. The sensor detects the value of the quantity of interest and produces an error signal, which measures the difference between the actual and the desired value. The actuator then provides a feedback, which corrects the error, driving the observed value closer to the desired one.

For a FP cavity, the error signal is obtained using the Pound–Drever–Hall locking scheme. This is a widely used technique, originally invented for stabilizing the wavelength of a laser, using as a reference the length L of a Fabry–Perot cavity. Suppose that we have a FP cavity whose length is fixed, to a sufficiently good precision. The wavelength of any laser has in general fluctuations, and if we want to stabilize it a simple idea is to shine it on a FP cavity of the appropriate length L, chosen so that the desired value of λ_L is resonant, and look at the transmitted light. As shown in Fig. 9.9, we have a series of narrow peaks as a function of $\lambda_{\rm L}$. If the wavelength of the laser has a slight mismatch with respect to the resonant value, we are just slightly displaced from the peak, so the transmitted intensity is lower. We could then use this as an error signal, and correct for this error with a feedback mechanism. This scheme however has two drawbacks. First, from the fact that the power decreases we cannot tell in which direction the wavelength fluctuated, and therefore we do not know the sign of the correction to be applied. Second, we cannot disentangle wavelength fluctuations from intrinsic power fluctuations of the laser.

The solution is to use modulated light, so the electric field entering the FP cavity has the form (9.178), with the carrier at the resonant frequency. Upon reflection, taking $\sigma \ll 1$, we see from eq. (9.193) that the carrier takes a minus sign while the sidebands get a plus sign. Using the fact that $J_0(-\Gamma) = J_0(\Gamma)$ and $J_1(-\Gamma) = -J_1(\Gamma)$, we see that this still has the form of modulated light, with modulation index $-\Gamma$. Thus the reflected power is simply $|E_0|^2$, i.e. it contains a DC term and no term at the modulation frequency $\Omega_{\rm mod}$. In this sense, we have a null instrument: the signal that we use, which is the part oscillating as $\Omega_{\rm mod}$, vanishes in the absence of perturbations. Suppose now that a fluctuation changes the wavelength $\lambda_{\rm L}$ of the laser, with respect to the length L

of the cavity. The carrier, which is on resonance, is very sensitive to this perturbation, while the sidebands, which are far from resonance, are completely insensitive, see Fig. 9.10. Thus the reflected field of the carrier is multiplied by a factor $\exp\{i\Delta\phi\}$, while the sidebands are unchanged. In the power $|E_{\rm refl}|^2$, the beating between the carrier and the sidebands now produces a term oscillating at a frequency $\Omega_{\rm mod}$ and linear in $\Delta\phi$, which can be demodulated with a mixer. This is a way to obtain an error signal which, at least close to the resonance, is linear in the deviation $\Delta\phi$. We can therefore use it to lock the laser wavelength to the length L of the cavity.

If we assume for a moment that the laser frequency is already sufficiently stable (we will come back below to this point) and the cavity is not rigid, as in a GW interferometer, we can turn the argument around, using $\lambda_{\rm L}$ as our standard of length, and lock the cavity length L to the wavelength $\lambda_{\rm L}$ of the laser. We now realize that the detection scheme on the dark fringe that we discussed in Section 9.3.2 is nothing but a variant of this Pound–Drever–Hall locking scheme. In the original Pound–Drever–Hall method the need for a signal linear in $\Delta\phi$ arises because we want to know the sign of $\Delta\phi$ in order to correct for it in the proper direction, while in the detection scheme for GWs it arises first of all from the fact that the shift $\Delta\phi$ is $O(h)$, and a quantity $O(h^2)$ would be undetectably small. Observe that, even if the interferometer is always on the dark fringe, the information on the value of h can then be read from the fact that we know the feedback that we had to apply to keep it there.

For the control of the interferometer, one generally collects all the beams that come out from it (including the little light that comes out in transmission from the end-mirrors of the arms) and uses all the information contained in this modulated light to perform a Pound–Drever–Hall locking of the three FP cavities of the interferometer (the two arms and the power-recycling cavity). Actually, if we had a laser sufficiently stable in frequency, we could use as GW detector a single arm with a FP cavity, and the sensitivity of the detector would degrade only by a factor of two (given that, for optimal orientation, the contribution of the GWs in the two arms is summed up). However, lasers of the required stability do not exist. So, the above procedure can be seen as locking first the laser to the length of the FP cavity in one arm, and then using the laser wavelength so stabilized, to lock the second arm cavity to it, so we are really measuring the displacement in one arm in units of the length of the other arm. More precisely, we lock the laser to the common mode, where the two arms move symmetrically, and we detect GWs in the differential mode, where the two arms move anti-symmetrically.

The Pound–Drever–Hall locking ensures that all the FP cavities are operating on resonance. Then, we must ensure that the two beams combine at the output of the interferometer so that they are on the dark fringe. This is done using as error signal the one generated by the Schnupp asymmetry. We discussed it on page 506, considering the phase shift $\Delta\phi$ induced by a GW, but the same argument can be repeated for the phase shift induced by the noise. Again, using modulated light and asymmetric arm lengths, we get a signal linear in $\Delta\phi$ at the frequency $\Omega_{\rm mod}$, that we can use as error signal. This technique is called Schnupp locking.

Experimentally, once the interferometer is at its working point, it is not so difficult to keep it there for very long time. The most difficult part is the so-called lock acquisition, i.e. bringing the instrument from the free state down to a controlled state. In the absence of controls, the mirrors are typically swinging with an amplitude of a few microns, therefore a factor $O(10^4)$ larger than what we can tolerate, and have typical speeds of a few microns per second, so they are sweeping across many resonances. Thus the control system must be fast enough to "grab" a mirror when it passes close to a resonance, and keep it there, using magnetic actuators. Moreover, we have stringent conditions on the alignment of the mirrors; for instance the input mirrors of the Fabry–Perot cavities must be aligned within $\delta\theta < O(10^{-8})$ rad. Such efficient control systems have by now been developed by the collaborations running the large GW interferometers, and locking and correct alignment are by now obtained quite routinely.

9.4 Noise sources

Having defined the experimental setup, we can now investigate the sensitivity that can be obtained. The sensitivity at which a GW interferometer must aim, to have good chances of detection, is extremely ambitious. We saw in Chapter 7 that the GW amplitude that can be detected depends crucially on the kind of signal (burst, periodic, coalescence or stochastic) that we are searching. As a first benchmark, we can consider a burst that releases in GWs an energy of 10^{-2} solar masses, taking place in the Virgo cluster of galaxies. As we saw on page 365, this gives a GW amplitude on Earth of just $h_0 \sim 10^{-21}$. As we have seen in this chapter, the corresponding displacement of the mirror of the interferometer is $\Delta L = (1/2)h_0 L$ (for $\omega_{\rm gw}L/c \ll 1$), so for $L = 4$ km, we have

$$\Delta L \sim 2 \times 10^{-18}\,\text{m}\,, \qquad (9.205)$$

which is smaller that the size of a nucleus by a factor 10^3! Impressive as it might be, this figure is however somewhat misleading because, as we have repeatedly emphasized, we must not forget that this is a coherent displacement of all the atoms of a macroscopic body such as a mirror. A better figure is given by the corresponding phase shift, which for a simple Michelson interferometer is $\Delta\phi_{\rm Mich} = (4\pi/\lambda_{\rm L})\,h_0 L$, see eqs. (9.27) and (9.28). Setting $\lambda_{\rm L} = 1\,\mu$m gives $\Delta\phi_{\rm Mich} \sim 5 \times 10^{-11}$ rad. We have seen however that for an interferometer with Fabry–Perot cavities we gain a factor $2\mathcal{F}/\pi$ in $\Delta\phi$, see eq. (9.102). For $\mathcal{F} = 200$ this is a factor $\simeq 130$, which means that we aim at measuring a phase shift

$$\Delta\phi_{\rm FP} \sim 10^{-8}\,\text{rad}\,. \qquad (9.206)$$

In the following subsections we examine the dominant noise sources, to see what sensitivity can be reached. The sensitivity is conveniently expressed in terms of the strain sensitivity $S_n^{1/2}(f)$, with dimensions $\text{Hz}^{-1/2}$. From its value we can then obtain the sensitivity to all type of signals, such as bursts, periodic signals, etc., as discussed in Chapter 7.

9.4.1 Shot noise

The first source of noise that we consider is the shot noise of the laser. This originates from the fact that the laser light comes in discrete quanta, the photons. Let N_γ be the number of photons that arrives on the photodetector in an observation time T. Then the average power measured at the photodetector during this observation time is

$$P = \frac{1}{T} N_\gamma \hbar\omega_{\rm L} \,. \tag{9.207}$$

When we measure the average output power, we are actually counting the number of photons that arrived in a time T. Whenever we count a number of *discrete* independent events the set of outcomes follows the Poisson distribution,

$$p(N;\bar{N}) = \frac{1}{N!}\bar{N}^N e^{-\bar{N}} \,, \tag{9.208}$$

where $\bar{N}$ is the average value of N. Since this is the probability distribution when we count a number of independent events, it is also known as the *counting statistics*. For large N the Poisson distribution becomes a Gaussian, with standard deviation equal to $\sqrt{N}$. Therefore, the fluctuation in the number of photons is given by

$$\Delta N_\gamma = \sqrt{N_\gamma} \,. \tag{9.209}$$

It is worth stressing that this is a fundamental limitation due to the corpuscular nature of light. This produces a fluctuation in the observed power given by

$$\begin{aligned}(\Delta P)_{\rm shot} &= \frac{1}{T} N_\gamma^{1/2} \hbar\omega_{\rm L} \\ &= \left(\frac{\hbar\omega_{\rm L}}{T} P\right)^{1/2} \,, \end{aligned} \tag{9.210}$$

where in the second line we eliminated $N_\gamma^{1/2}$ using eq. (9.207). We want to compare this result with the power fluctuations induced by a GW.

To make the setting simpler, we first consider a Michelson interferometer, with no Fabry–Perot cavities in the arms. We neglect the modulation of the laser light and for the moment we work at a generic point ϕ_0. Then, according to eq. (9.32), in the absence of GWs the output power P is related to the input power P_0 by $P = P_0 \sin^2\phi_0$, so eq. (9.210) becomes

$$(\Delta P)_{\rm shot} = \left(\frac{\hbar\omega_{\rm L}}{T} P_0\right)^{1/2} |\sin\phi_0| \,. \tag{9.211}$$

On the other hand, again from eq. (9.32), the variation in power due to a GW is

$$(\Delta P)_{\rm GW} = \frac{P_0}{2} |\sin 2\phi_0|\, (\Delta\phi)_{\rm Mich} \,. \tag{9.212}$$

We consider a periodic GW with frequency f, with only the plus polarization and coming from optimal orientation, and at first we take for simplicity $2\pi f L/c \ll 1$. According to eqs. (9.21) and (9.28), the amplitude of the phase shift $\Delta\phi_{\rm Mich}$ is then

$$|\Delta\phi_{\rm Mich}| = \frac{4\pi L}{\lambda_{\rm L}} h_0 \,, \tag{9.213}$$

so the power fluctuations induced by this GW have an amplitude

$$(\Delta P)_{\rm GW} = \frac{P_0}{2} |\sin 2\phi_0|\, \frac{4\pi L}{\lambda_{\rm L}} h_0 \,. \tag{9.214}$$

The signal-to-noise ratio (defined, as in Chapter 7 to be linear in the amplitude h_0 of the GW) for this periodic GW, when the only source of noise is the shot noise, is then

$$\begin{aligned}\frac{S}{N} &= \frac{(\Delta P)_{\rm GW}}{(\Delta P)_{\rm shot}} \\ &= \left(\frac{P_0 T}{\hbar\omega_{\rm L}}\right)^{1/2} \frac{4\pi L}{\lambda_{\rm L}} h_0 |\cos\phi_0| \,. \end{aligned} \tag{9.215}$$

For definiteness, we compute the shot noise at the naive working point where $\cos\phi_0 = 1/\sqrt{2}$ (the point 1 in Fig. 9.24),[28] so

$$\frac{S}{N} = \left(\frac{P_0 T}{2\hbar\omega_{\rm L}}\right)^{1/2} \frac{4\pi L}{\lambda_{\rm L}} h_0 \,. \tag{9.216}$$

On the other hand, we see from eq. (7.129) that, for a periodic GW of frequency f, coming from optimal direction and observed for a time T, the signal-to-noise ratio is written in terms of the strain sensitivity $S_n^{1/2}(f)$ as

$$\frac{S}{N} = \left[\frac{T}{S_n(f)}\right]^{1/2} h_0 \,. \tag{9.217}$$

Comparing eqs. (9.216) and (9.217) we see that $T^{1/2}$ and h_0 cancel, and we get the strain sensitivity due to the shot noise,

$$S_n^{1/2}(f)\Big|_{\rm shot} = \frac{\lambda_{\rm L}}{4\pi L}\left(\frac{2\hbar\omega_{\rm L}}{P_0}\right)^{1/2} \,. \tag{9.218}$$

For an interferometer with Fabry–Perot cavities, the result can be obtained replacing $|\Delta\phi_{\rm Mich}|$ in eq. (9.213) by $|\Delta\phi_{\rm FP}|$. For an interferometer with power recycling, the input laser power P_0 in eq. (9.220) must be replaced with the power circulating in the recycling cavity, so $P_0 \to CP_0$, where C is the factor gained with power recycling (typically $C = O(50-100)$ with present detectors, so that $CP_0 = O(1)$ kW). We

[28] Actually, eq. (9.215) is maximized when $\phi_0 = 0$, i.e. on the dark fringe. Thus, even in the absence of phase modulation, the dark fringe would be the optimal working point, if the only noise were the shot noise. However, this comes out because both the GW signal and the shot noise vanish at the dark fringe, with a finite ratio which optimizes S/N. Since there are other noise, such as test mass movements, that do not vanish at the dark fringe, in the absence of phase modulation the dark fringe is not an acceptable working point.

also take into account the efficiency of the photodetector, which reduces the effective power used to extract electrons at the photodiode by a factor η (a typical value can be $\eta = 0.93$), so $P_0 \to \eta P_0$.

Furthermore, we do not want to limit ourselves to the static limit, but we take into account the dependence on the GW frequency. Thus we use eq. (9.123) for $|\Delta\phi_{\rm FP}|$, and eq. (9.217) is replaced by

$$\frac{S}{N} = \left(\frac{\eta C P_0 T}{2\hbar\omega_{\rm L}}\right)^{1/2} \frac{8\mathcal{F}L}{\lambda_{\rm L}}\, h_0\, \frac{1}{\sqrt{1+(f/f_p)^2}}\,, \tag{9.219}$$

and (writing $\omega_{\rm L} = 2\pi c/\lambda_{\rm L}$) eq. (9.218) becomes

$$\boxed{S_n^{1/2}(f)\Big|_{\rm shot} = \frac{1}{8\mathcal{F}L}\left(\frac{4\pi\hbar\lambda_{\rm L} c}{\eta P_{\rm bs}}\right)^{1/2} \sqrt{1+(f/f_p)^2}\,,} \tag{9.220}$$

where $P_{\rm bs} \equiv CP_0$ is the power on the beam-splitter after recycling.

An instructive way to rephrase the above computation is as follows. According to eq. (9.32), the variation in the output power of a Michelson interferometer induced by a GW, choosing as working point $\phi_0 = \pi/4$, is $\Delta P = P_0\, \Delta\phi_{\rm Mich}/2$. Since all we measure is the power at the photodetector, the power fluctuation eq. (9.210) has the same effect as a phase shift $\Delta\phi_{\rm Mich}$ induced by a GW, with

$$\frac{1}{2} P_0\, \Delta\phi_{\rm Mich} = \frac{1}{T} N_\gamma^{1/2} \hbar\omega_{\rm L}\,. \tag{9.221}$$

On the other hand, at $\phi_0 = \pi/4$, we have $P = P_0/2$, so $P_0 = 2P = 2N_\gamma \hbar\omega_{\rm L}/T$, which, inserted in eq. (9.221), gives

$$\Delta\phi_{\rm Mich} = \frac{1}{\sqrt{N_\gamma}}\,. \tag{9.222}$$

This is the rms value of the equivalent phase shift. To compute its spectral density $S_{\Delta\phi}(f)$ we proceed as follows. Let $A(t)$ be any random variable, such that

$$\langle A(t)A(t')\rangle = A_0 \delta(t-t')\,. \tag{9.223}$$

This is the case of shot noise, since there is no correlation between the fluctuations of photon number at different times. As we saw in eq. (7.16), the (single-sided) spectral density $S_A(f)$ of any quantity A is in general defined from

$$\langle A(t)A(t')\rangle = \frac{1}{2}\int_{-\infty}^{\infty} df\, S_A(f) e^{-i2\pi f(t-t')}\,. \tag{9.224}$$

When eq. (9.223) holds, we see that $S_A(f)$ is independent of f, and has the value $S_A = 2A_0$ (as we already saw below eq. (8.122)). On the other hand, setting $t = t'$ in eq. (9.223), we get $\langle A^2(t)\rangle = A_0\delta(0) =$ $(1/2)S_A\delta(0)$. If we do not have an instantaneous resolution in time, but rather we perform a coarse graining over an observation time T, the Dirac delta must be replaced by its regularized version (with unit area), defined by $\delta(t) = 1/T$ if $-T/2 < t < T/2$ and $\delta(t) = 0$ if $|t| > T/2$, so $\delta(0) = 1/T$. Therefore

$$\langle A^2(t)\rangle = \frac{1}{2T} S_A\,. \tag{9.225}$$

Thus the strain sensitivity $S_A^{1/2}$ can be obtained from the rms value of A, $\langle A^2(t)\rangle^{1/2}$, multiplying it by $(2T)^{1/2}$. In particular the spectral density of the phase shift, $S_{\Delta\phi}$, is given by

$$\begin{aligned} S_{\Delta\phi}^{1/2} &= \sqrt{\frac{2T}{N_\gamma}} \\ &= \sqrt{\frac{2\hbar\omega_{\rm L}}{P}}\,. \end{aligned} \tag{9.226}$$

To pass from the spectral density of $\Delta\phi$ to the spectral density of the noise $n(t)$, which is the quantity to be compared with the GW signal $h(t)$, we use eq. (9.125), i.e. we divide by the transfer function (9.126). (In the language explained at the beginning of Chapter 7, dividing by the transfer function we are referring the noise to the input of the detector). This gives back eq. (9.220).

Observe that $S_n^{1/2}(f)|_{\rm shot}$ is flat up to the pole frequency, and then raises linearly in f. This is due to the fact that the shot noise in itself is independent of the frequency, while the transfer function, i.e. the sensitivity of a FP interferometer to GWs, degrades linearly with f beyond f_p. Inserting the numerical values we get

$$\begin{aligned} S_n^{1/2}(f)\Big|_{\rm shot} \simeq{}& 1.5\times 10^{-23}\,{\rm Hz}^{-1/2} \left(\frac{50}{\mathcal{F}}\right)\left(\frac{3\,{\rm km}}{L}\right)\left(\frac{1\,{\rm kW}}{P_{\rm bs}}\right)^{1/2} \\ &\times\sqrt{1+(f/f_p)^2}\,, \end{aligned} \tag{9.227}$$

where we set $\lambda_{\rm L} = 1\,\mu{\rm m}$, and we used reference values appropriate for the initial VIRGO. Recall that (at the initial detector stage) for VIRGO $f_p \simeq 500$ Hz and for LIGO $f_p \simeq 90$ Hz.[29]

9.4.2 Radiation pressure

Equation (9.220) indicates that, to beat the shot noise, we should increase the power $P_{\rm bs}$, either increasing the input laser power or increasing the recycling factor C. However, a beam of photons that impinges on a mirror and is reflected back exerts a pressure on the mirror itself. If this radiation pressure were constant, it could simply be compensated by the mechanism that holds the mirrors in place. However, since the number of photons arriving on the mirror fluctuates as in eq. (9.209), the radiation pressure fluctuates, too, and generates a stochastic force that shakes the mirrors. We see from eq. (9.210) that this stochastic force

---

[29] Our discussion is simplified, since we have not taken into account the effect of the phase modulation of the laser light. Numerically, this gives a strain sensitivity higher by approximately a factor of $(3/2)^{1/2}$ compared to the one obtained in eq. (9.220), see the Further Reading section.

grows as $\sqrt{P_{\rm bs}}$ while, from eq. (9.220), shot noise decreases as $1/\sqrt{P_{\rm bs}}$. If, in order to beat the shot noise, we increase the power $P_{\rm bs}$, beyond a certain limiting value the fluctuations in the radiation pressure will become important, and will dominate over the shot noise.

To compute the strain sensitivity due to radiation pressure we proceed as follows. Consider a laser beam with power P that impinges perpendicularly on a mirror. At reflection each photon changes its momentum from $+\mathbf{p}$ to $-\mathbf{p}$, so it transfers a momentum $2|\mathbf{p}|$ to the mirror. Since the photon energy is $E_\gamma = |\mathbf{p}|/c$, the force that a beam of power P exerts on the mirror is $F = 2P/c$. The rms fluctuations of the force in a time T are therefore related to the power fluctuations by $\Delta F = 2\Delta P/c$. Using eq. (9.210),

$$\Delta F = 2\sqrt{\frac{\hbar\omega_{\rm L} P}{c^2 T}}\,. \tag{9.228}$$

The fluctuation in the number of photons is independent of the frequency, so the spectral density of the force, $S_F(f)$, must be flat in frequency and, using eq. (9.225), is given by

$$S_F^{1/2} = 2\sqrt{\frac{2\hbar\omega_{\rm L} P}{c^2}}\,. \tag{9.229}$$

This stochastic force F acts on a mirror that, in the horizontal plane, is otherwise free, so we have $F = M\ddot{x}$, where M is the mass of the mirror and x its coordinate. In Fourier space, this means $\tilde{F}(f) = -M(2\pi f)^2\tilde{x}$, so the spectral density of the displacement of the mirror is[30]

$$S_x^{1/2}(f) = \frac{2}{M(2\pi f)^2}\sqrt{\frac{2\hbar\omega_{\rm L} P}{c^2}}\,. \tag{9.230}$$

Consider now what happens in an interferometer. We consider first a simple Michelson interferometer, taking the beam-splitter much heavier than the end-mirrors (so we can neglect its recoil). When a photon arrives on the beam-splitter, it is scattered randomly into one or the other arm. As a result, in each arm the distribution of photons is a Poissonian. The important point is that the distributions in the two arms are *anti-correlated.* One more photon into one arm means one less in the other. In the differential mode of the interferometer the contributions due to radiation pressure in the two arms therefore add up, so the radiation pressure in an interferometer is obtained multiplying eq. (9.230) by a factor of two (while correlated fluctuations in the two arms, such as intrinsic laser power fluctuations, cancel out).[31]

To express the result in terms of the equivalent noise spectral density, we must divide by the transfer function that relates ΔL to the GW amplitude h. For a simple Michelson interferometer, at $f \ll f_p$ we have $\Delta L = hL$, so the transfer function is simply L, and the strain sensitivity $S_n^{1/2}(f)$ due to radiation pressure is

$$S_n^{1/2}(f)\Big|_{\rm rad\ pres} = \frac{4}{ML(2\pi f)^2}\sqrt{\frac{2\hbar\omega_{\rm L} P}{c^2}}\,. \tag{9.231}$$

Consider next an interferometer with Fabry–Perot cavities. In this case the result depends on the finesse $\mathcal{F}$ of the arm cavities. Physically, this dependence can be understood observing that, in a FP cavity with finesse $\mathcal{F}$, light is performing on average $\mathcal{N} = 2\mathcal{F}/\pi$ bounces. Then each photon hits the mirrors $O(\mathcal{N})$ times, so the rms value ΔL of the length of the cavity is $O(\mathcal{N})$ times larger than the value when the light make only one bounce. Furthermore, when the cavity is at resonance, a given value of ΔL produces a phase shift in the reflected light larger by a factor $T_{\rm FP}(f) = O(\mathcal{N})$, compared to the one-bounce case. Overall, the total effect on the phase shift induced by the radiation pressure is therefore $O(\mathcal{N}^2)$. However, to compare with the effect of a GW (i.e. to refer the noise to the detector input, in the language of Chapter 7) we must divide by the transfer function of an interferometer with Fabry–Perot cavities, which is again $T_{\rm FP}(f)$, and we are left with a single factor $O(\mathcal{N})$.

In other words, a given displacement $\Delta\tilde{x}(f)$ of a mirror due to radiation pressure results in a phase shift $\Delta\phi_{\rm FP}(f)$ which is much larger than for the single-bounces case, since now the transfer function is $T_{\rm FP}(f)$, given in eq. (9.126), which is proportional to $\mathcal{F}$ or, equivalently, to the number of bounces. However, in order to refer the noise to the detector input, we must divide by the same transfer function, so the two effects cancel. The fact that each photon performs $O(\mathcal{N})$ bounces results in the fact that the power inside the cavity is larger by a factor $O(\mathcal{N})$ than the power $P_{\rm bs}$ at the beam-splitter. Indeed, from eq. (9.72), at resonance the power inside the cavity is

$$P_{\rm cav} = P_{\rm bs}\,\frac{t_1^2}{(1 - r_1 r_2)^2}\,. \tag{9.232}$$

Setting for simplicity $r_2 = 1$ and $t_1^2 = 1 - r_1^2 - p_1 \simeq 1 - r_1^2$, this gives $P_{\rm cav} = P_{\rm bs}(1 + r_1)/(1 - r_1)$ which, for r_1 close to one, can be written as

$$P_{\rm cav} \simeq P_{\rm bs}\,\frac{2\mathcal{F}}{\pi}\,. \tag{9.233}$$

Therefore a fluctuation $\Delta P_{\rm bs}$ of the light arriving on the input mirror induces a fluctuation of the field inside the cavity $\Delta P_{\rm cav} \simeq \Delta P_{\rm bs}\,(2\mathcal{F}/\pi)$. Actually, if the mirror vibrates at a frequency f, the cavity is displaced off resonance, and the power inside the cavity is reduced by a factor $[1 + (f/f_p)^2]$, as we see from eq. (9.81), together with the definitions (9.84) and (9.122). As a result (writing $\omega_{\rm L} = 2\pi c/\lambda_{\rm L}$ in eq. (9.231))

$$\boxed{S_n^{1/2}(f)\Big|_{\rm rad} = \frac{16\sqrt{2}\,\mathcal{F}}{ML(2\pi f)^2}\sqrt{\frac{\hbar}{2\pi}\,\frac{P_{\rm bs}}{\lambda_L c}}\,\frac{1}{\sqrt{1 + (f/f_p)^2}}\,.} \tag{9.234}$$

This result answers a question that might have been asked when we realized that the response to GWs of an interferometer with Fabry–Perot cavities, with arm-length L and finesse $\mathcal{F}$, is equivalent to that

---

[30] More accurately, when a suspended mirror oscillates there is a restoring force due to gravity, so it should be really treated as a harmonic oscillator, with resonance frequency ω_0 and dissipation coefficient γ (defined as in eq. (8.20)). Then the factor $(2\pi f)^2 = \omega^2$ in the denominator of eq. (9.230) must be replaced by $|\omega^2 - \omega_0^2 + i\gamma\omega_0|$, compare with eq. (8.23). However, the resonance frequency ω_0 and the dissipation coefficient γ are smaller than the frequency ω at which we are interested, and in a first approximation can be neglected.

[31] Another way to describe the same phenomenon is in terms of vacuum fluctuations of the electromagnetic field entering the interferometer from the output port, see Caves (1980, 1981).

of a simple Michelson interferometer with arm-length $(2/\pi)\mathcal{F}L$. Given that very high finesse cavities are not difficult to build (e.g. the mode cleaner has a finesse $O(10^3)$) why bother to construct a km-sized arm, with all the financial and technical problems that this implies (e.g. the very high vacuum in such a long arm, see below)? We could think that it is sufficient to build a table-top interferometer with a sufficiently large finesse.

The answer is that the response of the detector to GWs, encoded in the transfer function (9.126), is only one side of the issue. What really matters is the signal-to-noise ratio, and we must also ask how the various noise scale with $\mathcal{N}$ and L. For instance, shot noise is independent of $\mathcal{N}$. When divided by the transfer function, which is $O(\mathcal{N})$, the signal-to-noise ratio therefore scales as $1/\mathcal{N} = O(1/\mathcal{F})$. To beat down such a noise we could in principle keep L small, as long as we use a cavity with a sufficiently high finesse. However, we have seen that radiation pressure noise rather scales as $\mathcal{N}^2$, so after dividing by the transfer function we have a dependence proportional to $\mathcal{N}$, i.e. to $\mathcal{F}$. In this case a very large finesse would be harmful. Below, we will see that displacement noise, such as mirror thermal noise, scale as $\mathcal{N}$, so after dividing by the transfer function we get a the signal-to-noise ratio which is independent of $\mathcal{F}$ (but still proportional to $1/L$), so in this case a high finesse does not help to beat it down, and we need a large arm-length L. So, in general we still want to keep L as large as possible, compatibly with technological and financial constraints.

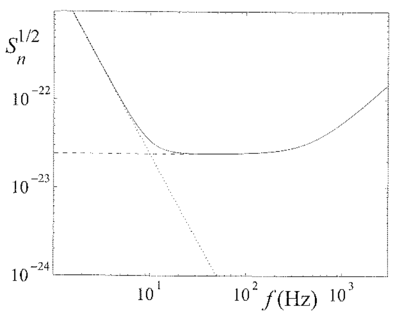

Fig. 9.26 The strain sensitivity $S_n^{1/2}(f)$ (in units $\mathrm{Hz}^{-1/2}$) due to shot noise (dashed), to radiation pressure (dotted) and the total optical read-out noise (solid line). For definiteness, we have used numerical values of the various parameters typical of the initial VIRGO interferometer.

9.4.3 The standard quantum limit

Consider now the combined effect of shot noise and radiation pressure, that we denote as *optical read-out noise*. Its spectral density is

$$S_n(f)\big|_{\rm opt} = S_n(f)\big|_{\rm shot} + S_n(f)\big|_{\rm rad}\,. \tag{9.235}$$

A plot of this expression, and of the separate shot noise and radiation pressure contributions, is shown in Fig. 9.26. The shot noise contribution is proportional to $P_{\rm bs}^{-1/2}$ while the radiation pressure to $P_{\rm bs}^{1/2}$. We see here the uncertainty principle in action. The situation is conceptually similar to the Heisenberg microscope. We are using photons to measure the position of an object. The photons impart non-deterministically a recoil to the object, here in the form of fluctuations of the radiation pressure, and this recoil disturbs the measure that we are performing. It is amazing that a quantum effect due to the uncertainty principle can be important in the measurement of the position of a macroscopic body, like the mirror of an interferometer, which typically weights $O(20)$ kg. However, for GW detection we need such an extreme accuracy in the determination of the mirror position that, as we will see in this section, the uncertainty principle can indeed become important.[32]

Using the explicit expressions and defining

$$f_0 = \frac{8\mathcal{F}}{2\pi}\sqrt{\frac{P_{\rm bs}}{\pi\lambda_{\rm L}cM}}\,, \tag{9.236}$$

---

[32] We already met a similar situation for resonant bars in Sections 8.3.3 and 8.3.4, where we found that, without quantum non-demolition techniques, the best one can do is to detect vibrations in the bar corresponding to $O(1)$ phonon. We have seen that present bar sensitivities are not that far from this limit.

eq. (9.235) can be written as

$$S_n^{1/2}(f)\Big|_{\rm opt} = \frac{1}{L\pi f_0}\sqrt{\frac{\hbar}{M}}\left[\left(1+\frac{f^2}{f_p^2}\right)+\frac{f_0^4}{f^4}\,\frac{1}{1+f^2/f_p^2}\right]^{1/2}\,. \tag{9.237}$$

For a given value of f we can minimize $S_n^{1/2}(f)|_{\rm opt}$ with respect to f_0. (In particular, f_0 is varied changing the power $P_{\rm bs}$, so this amounts to finding the optimal value of $P_{\rm bs}$.) The optimal value of f_0 is the one for which the shot noise and radiation pressure contributions are equal, and is given by

$$1+\frac{f^2}{f_p} = \frac{f_0^2}{f^2}\,. \tag{9.238}$$

The corresponding optimal value of $S_n^{1/2}(f)$ defines the *standard quantum limit* (SQL),

$$\boxed{S_{\rm SQL}^{1/2}(f) = \frac{1}{2\pi f L}\sqrt{\frac{8\hbar}{M}}\,.} \tag{9.239}$$

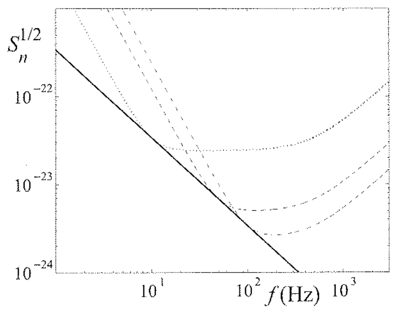

Fig. 9.27 The optical read-out strain sensitivity $S_n^{1/2}(f)|_{\rm opt}$ (in units $\mathrm{Hz}^{-1/2}$) for $f_0 = 10$ Hz (dotted line), $f_0 = 50$ Hz (dashed line) and $f_0 = 100$ Hz (dot-dashed line), compared to the SQL pseudo-spectral density (solid line). The other parameters are $L = 3$ km, $M = 20.3$ kg, $f_p = 500$ Hz.

It should be stressed that $S_{\rm SQL}(f)$, even if written as a function of f, cannot be interpreted as the minimum noise spectral density that can be reached with this type of optical read-out. In fact, the value of f_0, i.e. of the laser power, has been optimized keeping fixed the value of f. It therefore represents the minimum value of the spectral density which can be obtained (as long as only optical read-out noise is concerned) at that value of f. Once we have chosen the power so to optimize the sensitivity at a given frequency f, at all other values of the frequency we are not in the optimal situation, and the strain sensitivity is higher than the standard quantum limit. So, eq. (9.239) rather gives the envelope of the minima of the family of functions $S_n^{1/2}(f; f_0)|_{\rm opt}$, parametrized by f_0, as shown in Fig. 9.27. (For this reason, it is called a "pseudo-spectral density".)

It is useful to define the dimensionless quantity

$$\mathcal{K}(f) \equiv \frac{8\omega_{\rm L}P_{\rm bs}}{ML^2}\,\frac{1}{\omega^2(\omega_p^2+\omega^2)}\,, \tag{9.240}$$

where $\omega_p = 2\pi f_p$ and $\omega = 2\pi f$. Then eq. (9.237) can be rewritten as[33]

$$\boxed{S_n(f)\big|_{\rm opt} = \frac{1}{2}S_{\rm SQL}(f)\left[\frac{1}{\mathcal{K}(f)}+\mathcal{K}(f)\right]\,.} \tag{9.241}$$

We have seen that the existence of the limiting value $S_{\rm SQL}(f)$ is a manifestation of the Heisenberg uncertainty principle. However the uncertainty principle does not put a limit on the accuracy of measurements of position, but only on the accuracy of simultaneous measurements of conjugate variables, and it is possible to go beyond the standard quantum

---

[33] This result can also be obtained with an elegant formalism, in which radiation pressure and shot noise are related to the quantum vacuum fluctuations entering the interferometer from the output port, see Kimble, Levin, Matsko, Thorne and Vyatchanin (2000). The quantity that we denote by ω_p corresponds to γ in this reference. More precisely, $\gamma = ct_1^2/(4L)$, where t_1 is the transmissivity of the first mirror. In our computation we have assumed negligible losses, so $t_1^2 = 1 - r_1^2$, and r_1, r_2 close to one, so $\gamma \simeq \pi c/(2L\mathcal{F})$. Observe also that we have set to one the efficiency η of the photodiode and we have neglected the effect of light modulation. For instance, in the present configuration of VIRGO, this results in the replacement $1/\mathcal{K}(f) \to 3/[2\eta\mathcal{K}(f)]$ in the first term of eq. (9.241). Different modulation schemes can give rise to different numerical factor for this shot noise term.

limit using quantum non-demolition (QND) techniques. The general principles of QND measurements have already been presented in Section 8.3.4. We refer the reader to the Further Reading section for the application of these techniques to GW interferometers. These techniques can become important for advanced interferometers.

9.4.4 Displacement noise

The optical read-out noise discussed above is intrinsic to the way that we use to detect the displacement of the test masses induced by GWs, using a laser beam that bounces between them. Of course, the test masses also move because of many other effects that have nothing to do with GWs. We generically denote all these other effects as "displacement noise", and we characterize them with a strain spectral density of the displacement $S_x^{1/2}(f)$, that we denote simply as $x(f)$.

Recall that the effect of a GW on the length L of a FP cavity is to change it by the amount $\Delta L = hL$ (as long as $\omega_{\rm gw}L/c \ll 1$, i.e. as long as eq. (9.124) holds). Thus, if the length of the cavity changes by an amount Δx because of one of these displacement noise, the corresponding equivalent GW amplitude is $\Delta x/L$. So, to refer the noise at the detector input (i.e. to compute the equivalent GW that would induce the same phase shift), we must divide the strain sensitivity of the displacement by the arm-length L. The finesse of the cavity, or equivalently the number of bounces $\mathcal{N}$ performed by the laser beam inside the FP cavity, does not enter here. This can also be understood in terms of the phase shift $\Delta\phi_{\rm FP}$, observing that the phase shift induced by a GW and that induced by the displacement noise of a mirror are both multiplied by the number of bounces of the light inside the cavity, so when we refer the noise to the detector input the factor $\mathcal{N}$ cancels.

The computation of these displacement noise depends on many technical issues such as properties of materials, details of the suspension mechanisms, etc. and a complete discussion is beyond the scope of this book. We limit ourselves to mentioning the most important displacement noise below. Graphs showing their separate effect on the strain sensitivity are shown in Section 9.5 below, in Fig. 9.31 for VIRGO and in Fig. 9.32 for LIGO.

Seismic and Newtonian noise

The Earth's ground is in continual motion, with amplitudes of order a few microns. In the region 1–10 Hz this is mostly due to human activity such as local traffic, trains, etc. as well as to local phenomena such as winds. Furthermore, there is a micro-seismic background, which affects a GW interferometer mostly in the form of surface waves that shake the suspension mechanisms and, finally, the mirrors.[34] Its strain sensitivity has in general the form

$$x(f) \simeq A\left(\frac{1\,\mathrm{Hz}}{f^{\nu}}\right)\mathrm{m\,Hz}^{-1/2}\,, \qquad (9.242)$$

where (above about 1 Hz) the index $\nu \simeq 2$ while, at a typical quiet location, A can be of order 10^{-7}. Dividing $x(f)$ by the length $L =$ 3–4 km, we are left with a noise strain sensitivity at least 10 orders of magnitude larger than the values at which we are aiming. The seismic noise must therefore be attenuated by a huge factor. This is in general obtained with a set of pendulums in cascade.[35] A single pendulum with resonance frequency f_0, at frequencies $f \gg f_0$ attenuates the strain sensitivity $x(f)$ by a factor f_0^2/f^2, and a multistage filter made by N stages provides an attenuation factor $(f_0^2/f^2)^N$. Therefore one must choose f_0 much smaller than the GW frequency of interest. In practice, this means that the seismic noise can be reduced below a level interesting for GW detection only at frequencies above, say, 10 Hz. This is the main reason while a ground-based interferometer cannot search for GWs below the ~ 10 Hz region.

Newtonian noise, also known as "gravity gradient noise", is due to the Newtonian gravitational forces of objects that are moving, which results in a time-varying gravitational force.[36] The most important Newtonian effect is induced by micro-seismic noise, which produce mass density fluctuations and therefore a fluctuation of the gravitational field of the Earth, which couples directly to the test masses of the interferometer. One can get a feeling for the extreme sensitivity of a GW interferometer, when one realizes that even the changing gravitational attraction due to atmospheric turbulence gives a non-negligible contribution to the Newtonian noise below $O(1)$ Hz.

While the seismic noise can be attenuated arbitrarily (at least in principle, if one were able to build an arbitrarily good attenuator), the Newtonian noise cannot be eliminated, since the gravitational force cannot be screened. In present GW interferometers the Newtonian noise is not the dominant effect (below a few Hz it is overwhelmed by the seismic noise and above a few Hz by the pendulum thermal noise, see Fig. 9.31). However, even if one were able to push further down the seismic and thermal noise, which in principle can be done with technological improvements, still one would remain with the Newtonian noise which, for a ground-based detector, would anyway provide the ultimate limitation at low frequencies (although some noise reduction might be possible monitoring it with a complex network of accelerometers, and then subtracting it).

Thermal noise

Thermal noise induce vibrations both in the mirrors and in the suspensions. As discussed in Section 8.3.1, its effect can be computed using the fluctuation–dissipation theorem. We saw that, for a linear system subject to a force F, we can always write the equation of motion in the form

$$\tilde{F}(\omega) = -i\omega Z(\omega)\tilde{x}(\omega)\,, \qquad (9.243)$$

where $Z(\omega)$ is called the impedance. The fluctuation–dissipation theorem gives the spectral density of the force responsible for thermal fluc-

[34] This backgrounds originates mostly from atmospheric cyclonic systems over the oceans. Energy is transferred from the atmosphere to the ocean, and then to the ocean floor. From there it is transmitted through the crust for long distances, $O(10^3)$ km, mostly in the form of surface waves. Its amplitude presents a peak corresponding to the period of the ocean waves (12 s) and another one at twice this frequency, and decreases as a power law at higher frequencies. Near the costs, there is also a contribution from sea waves breaking on the shore.

[35] Such an attenuation system is in itself a remarkable technological achievement. In particular, the VIRGO superattenuator, made of 8 m tall towers, is the most performing device of this kind ever built. The construction of these towers also present non-trivial problems in material science. To get a feeling for the kind of issues involved, consider that the slippage of two grains of steel under stress releases an energy sufficient to shake the mirror at the level of 10^{-12} m, about a million times larger than the expected GW signal.

[36] Obviously, these are quasi-static gravitational fields in the near region of their sources, and are distinct from GWs, that are time-varying gravitational fields in the far region of their sources.

tuations, $S_F(\omega)$, in terms of the real part of Z, see eq. (8.125). The displacement spectral density is then given by eq. (8.128), that we write as

$$x(\omega) = \frac{1}{\omega|Z(\omega)|}\left[4kT\,\mathrm{Re}\,Z(\omega)\right]^{1/2} . \tag{9.244}$$

Therefore, $x(\omega)$ is known once we have $Z(\omega)$. This has the great advantage that we do not need to have a detailed microscopic model of the dissipation mechanism. For a simple damped harmonic oscillator, $Z(\omega)$ is given by eq. (8.126). For a more complex extended object, the impedance associated to a normal mode with frequency ω_0 can be modeled more generally as

$$Z = -\frac{im}{\omega}[\omega^2 - \omega_0^2 + i\omega^2\phi(\omega)] , \tag{9.245}$$

where the dimensionless function $\phi(\omega)$ is called the loss angle. The most important thermal noise are the following.

Suspension thermal noise. Any vibration induced in the suspension of the test masses results in a displacement noise. In particular, we have

- Pendulum thermal fluctuations. These are thermal fluctuations that induce a swinging motion in the suspensions, and therefore a horizontal displacement of the mirrors. In the present detectors this noise is the dominant one between a few Hz and $O(50)$ Hz, see Fig. 9.31.
- Vertical thermal fluctuations. Thermal noise induce also a vertical motion of the suspensions. In a GW interferometer, we are only interested in the horizontal distance between the mirrors. However, because of the curvature of the Earth, the direction of the vertical at the two mirror locations, which are separated by a distance $L = 3$–4 km, is not the same. This results in a vertical–horizontal coupling of the order of the angle $\theta = L/(2R_\oplus) \simeq 2\times 10^{-4}$.
- Violin modes. These are vibrations that can be described in terms of fluctuations of the normal modes of the wire. They are responsible for the set of spikes between 300 Hz and a few kHz in Fig. 9.31. The width of these resonances is however very narrow, so they affect the sensitivity only in very small intervals of frequencies.

Test-mass thermal noise. These are thermal fluctuations within the test masses themselves. We can distinguish the following effects.

- Brownian motion of the mirrors. The atoms of a mirror at temperature T have a Brownian motion due to their kinetic energy, which gives rise to mirror thermal noise. Just as with the violin modes, its effect can be computed performing a normal-mode decomposition. This is presently the dominant noise between a few tens and a few hundred Hz, see Fig. 9.31.

- Thermo-elastic fluctuations. These are due to the fact that, in a finite volume V, the temperature fluctuates, with a variance $(\delta T)^2 = k_B T^2/(\rho C_V V)$, where C_V is the specific heat and ρ the density of the material. These temperature fluctuations generate displacement noise through the expansion of the material. Thermo-elastic fluctuations take place both in the mirror bulk and in the mirror coatings.
- Thermo-refractive fluctuations. The refraction index of the coatings is a function of the temperature. Thus, the same temperature fluctuations responsible for the thermo-elastic noise also induce fluctuations in the refraction index of the mirrors.

Of course, thermal noise is proportional to the dissipations present in the system, which depend strongly on the material used, and therefore there is an ongoing search for materials with optimal properties.

Other noise

Beside read-out and displacement noise, other noise are relevant, and keeping them under control require advanced technologies. We mention some of them, to give a feeling for the complexity of a GW interferometer.

- The laser beam must travel in a ultra-high vacuum pipe, in order to keep the noise induced by fluctuations in the index of refraction below the design sensitivity. For the initial interferometers the pressure must be lower than 10^{-7} mbar while, for advanced interferometers, it must be lower than 10^{-9} mbar.[37] Furthermore, the residual gas must be free of condensable organic molecules (hydrocarbons), in order to keep the optical surfaces clean. It is estimated that a hydrocarbon partial pressure of 10^{-13} mbar is required if one wants to avoid the cumulative deposition of one monolayer of molecules on the optical elements in 4 years.
- To limit diffuse light scattering in the interferometer, the mirrors are polished to a rms micro-roughness of about 0.5Å, over a diameter of order 20 cm, and have losses of order a few parts per million.[38]
- Fluctuations of the laser in power and in frequency must be kept under control to great accuracy.
- Other important concerns are so-called technical noise, often related to the servo loops that keep the many degrees of freedom of an interferometer under control.
- Seismic noise can be reinjected in the detector because the enclosure walls couple to the mirror magnets both directly, because of diamagnetism, and through eddy currents.
- The suspension wires undergo creep, i.e. sudden grain-boundaries slipping, which at this sensitivity level are so frequent that they finally constitute a Gaussian noise.

---

[37] These vacuum tubes have a diameter of about 1.2 m in order to contain the diffraction-limited laser beam, and a 3- or 4-km length, resulting in a total high-vacuum volume of about 9000 m^3. For comparison, this is much larger than the vacuum volume of the LEP particle accelerator, where the ring is almost 27 kms in length, but the transverse section of the vacuum pipe was an ellipse with semiaxes of about 6 cm and 3 cm, respectively.

[38] Nevertheless, the remaining diffused light still generates important noise because it can interact with the pipe walls, thereby getting modulated by its seismic noise, and then it can be rediffused back in the beam by reflection on a mirror. Even if only a few parts per million of the circulating light is diffused, an unacceptably high noise results. For this reason, in each of the 3 km arms of VIRGO have been mounted about 100 circular rings, obtained from a conical surface, that trap and absorb most of the residual diffused light.

- Non-Gaussian noise is also present. For instance, the release of residual gas pockets from the tube walls can generate sudden bursts.

So, many subtle effects can become important at the sensitivity level at which a GW interferometer aims. In spite of the apparent simplicity of the original idea, a GW interferometer is clearly a very complex instrument.

9.5 Existing and planned detectors

9.5.1 Initial interferometers

At time of writing (2007) there are various collaborations running GW interferometers. In the US, the LIGO collaboration runs two interferometers with arms of 4 km, one in Hanford (Washington State) and one in Livingstone (Louisiana). The two detectors have been placed at a large distance (the light travel time between them is about 10 ms), so that their noise should be uncorrelated, and are used to search for coincidences. In the Hanford site there is also a second smaller interferometer, with 2 km arms, in the same vacuum system. While of course there will be correlated noise between the shorter and the longer interferometer, still the presence of the smaller interferometer gives a further handle that helps discriminating real signals from spurious noise, making use of the fact that many common noise in the two detectors are independent of L, while the effect of the GW scales with L. A view of the Hanford detector is shown in Fig. 9.28. The scientists collaborating to the project are members of the LIGO Scientific Community (LSC).

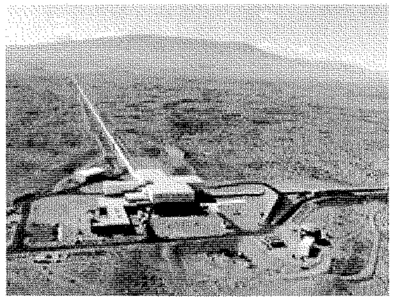

Fig. 9.28 A view of the LIGO detector in Hanford, Washington State. (Courtesy of the LIGO collaboration.)

The VIRGO interferometer, located near Pisa, Italy, is a collaboration between Italy and France, and has arms of 3 km. A view of the detector is shown in Fig. 9.29.

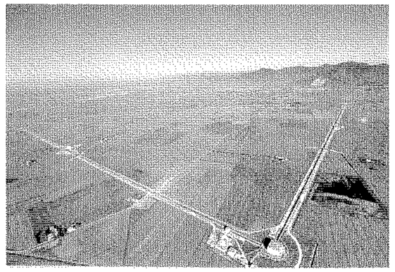

Fig. 9.29 A view of the VIRGO interferometer in Cascina, near Pisa. (Courtesy of the VIRGO collaboration.)

Beside these large GW interferometers, there are two smaller ones: GEO600, with arms of 600 m, is located near Hannover and is a German-British collaboration. GEO600 works in close collaboration with LIGO, and its members are also members of the LSC. TAMA is located in Tokyo, and has arms of 300 m. These smaller detectors are useful also for developing techniques that will be used by LIGO and VIRGO in their advanced stage.

In Fig. 9.30 we show a simplified model of the strain sensitivity of these detectors, in their initial stage. The best sensitivities are reached by the two detectors with longer arms, LIGO and VIRGO. In the low-frequency regime, the dominant noise is the seismic. For LIGO and GEO this results in a "seismic wall" below about 30–40 Hz. VIRGO has developed an advanced super-attenuator, so its target sensitivity is better at low frequencies. In the intermediate region the dominant noise is the mirror thermal noise. In this region GEO600 compensates the smaller arm length using fused silica suspensions, an advanced technique that reduces suspension thermal noise, and that will be adopted in advanced interferometers. Then, shot noise takes over and becomes the limiting noise at high frequencies. In this regime, the difference between the sensitivities of LIGO and VIRGO is due to the fact that LIGO has longer arms (4 km instead of 3 km for VIRGO) and a higher finesse ($\mathcal{F} = 200$ for LIGO and $\mathcal{F} = 50$ for VIRGO). On the one hand this means that, at $f \ll f_{\rm pole}$, the shot noise of LIGO is smaller than that of VIRGO, see eq. (9.220), which helps to give a better sensitivity in the 100 Hz region. On the other hand, we see from eq. (9.88) that the pole frequency of LIGO is smaller, $f_p \simeq 90$ Hz for LIGO and $f_p \simeq 500$ Hz for VIRGO. This means that in LIGO the shot noise curve begins to raise linearly earlier, so it finally get higher than in VIRGO.

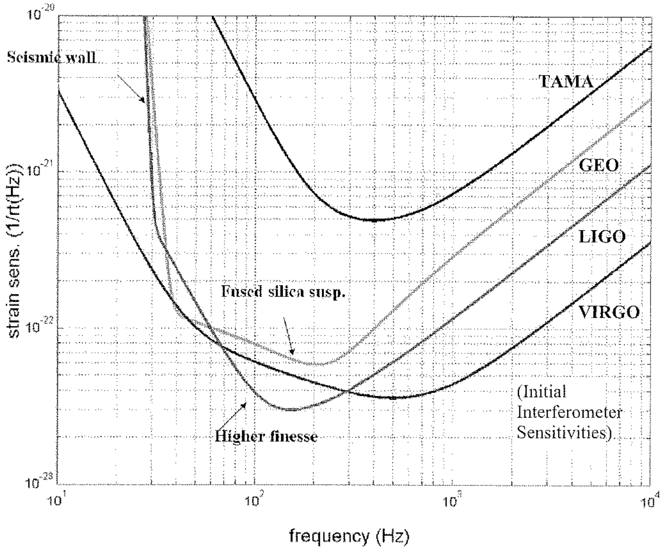

Fig. 9.30 A simplified model of the strain sensitivities of the initial interferometers.

A more accurate plot of the sensitivity, including the separate contributions from the various noise sources, is shown in Fig. 9.31 for VIRGO, while actual data from LIGO are shown in Fig. 9.32, and in Fig. 9.33 for GEO.[39]

Once we have the strain sensitivity, the signal-to-noise ratio of GW interferometers for different type of signals (coalescences, bursts, periodic signals and stochastic backgrounds) can be computed using the results of Chapter 7, similarly to what we did in Section 8.3.5 for resonant bars.

For a broadband GW detector such as an interferometer, a useful measure of the sensitivity is given in terms of the sight distance to coalescing binaries, that we introduced in Section 7.7.2. Inserting in eq. (7.182) the strain sensitivity of the initial LIGO and VIRGO one finds that, for a NS-NS binary, with NS masses $m_1 = m_2 = 1.4 M_{\odot}$, initial interferometers have a range

$$d_{\rm NS-NS} = O(20)\,{\rm Mpc}\,, \qquad (9.246)$$

---

[39] At time of writing (2007) initial LIGO has reached its target sensitivity and is completing a long science run, termed S5, with one year of coincident data between its detectors. As shown in Fig. 9.32, the noise budget is very well understood, and reproduces precisely the theoretical curves. VIRGO is presently close to reaching its target sensitivity, and is starting its first science runs. VIRGO and the LSC have signed an agreement for joint data taking and data exchange. The sensitivity of GW interferometers will probably be in rapid evolution in the near future, with various improvements and upgrades leading from the initial detectors to advanced interferometers.

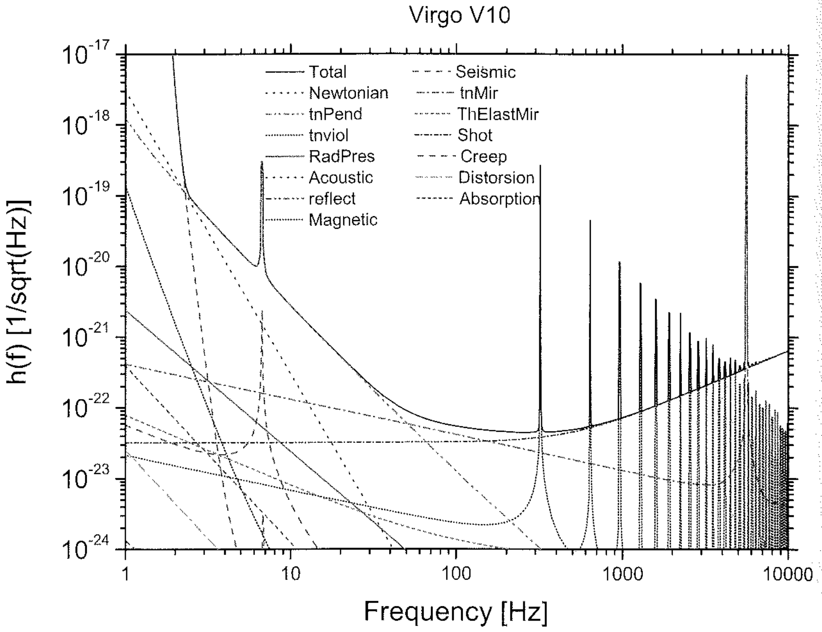

Fig. 9.31 The predicted strain sensitivity $S_n^{1/2}(f)$ (here denoted $h(f)$) of the initial VIRGO detector, and the various noise contributions. (Courtesy of the VIRGO collaboration.)

which barely includes the Virgo cluster of galaxies. For BH-BH binaries, assuming a black-hole mass of $10M_{\odot}$, as suggested by the observation of typical stellar-mass galactic black holes, gives a sight distance at initial interferometers

$$d_{\text{BH-BH}} = O(100)\,\text{Mpc}\,. \tag{9.247}$$

Estimates of the rate are uncertain and will be discussed in detail in Vol. 2, where we will see that, if our theoretical understanding of the formation and evolution of compact binaries is correct, at these distances the chances of a detection are small, with $O(10^{-4})$–$O(10^{-1})$ events per year for BH-BH coalescences, and $O(10^{-3})$–$O(10^{-2})$ for NS-NS binaries. We will see however in Section 9.5.2 that these rates improves drastically for advanced interferometer.

For burst searches, the sensitivity of a broadband detector depends strongly on where, in frequency, the burst is peaked, and on its temporal duration. Assuming for definiteness a flat spectrum over the frequency bandwidth, a burst that radiates an energy $10^{-6}M_{\odot}c^2$ in GWs would be visible, at SNR = 8 and assuming optimal orientation, up to $O(10)$ kpc.

For spinning pulsars, the sight distance is obtained from eq. (7.166) as a function of the ellipticity ϵ and of its frequency f_0.

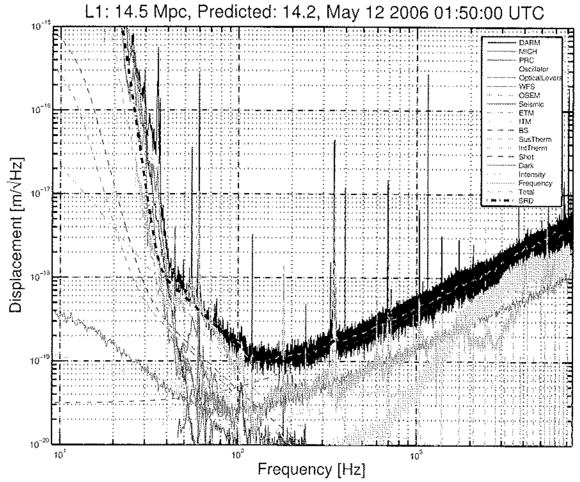

Fig. 9.32 The strain sensitivity, in $\text{m}/\sqrt{\text{Hz}}$, of the LIGO detector in Livingston. The strain sensitivity in $\text{Hz}^{-1/2}$ is obtained dividing by the arm length $L = 4000$ m. The noise budget is very well understood. (Courtesy of the LIGO collaboration.)

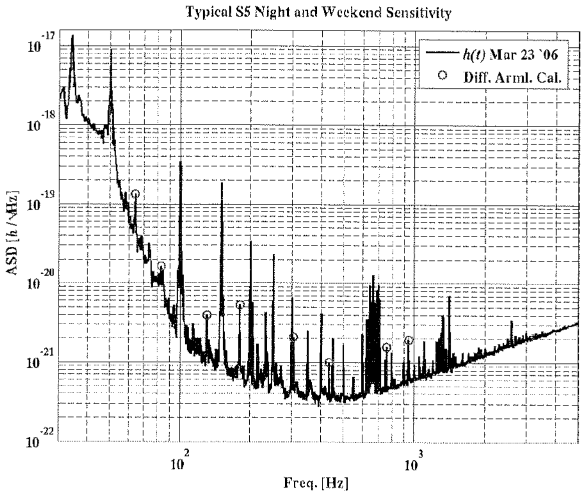

Fig. 9.33 The strain sensitivity, in $1/\sqrt{\text{Hz}}$, of the GEO detector during the S5 run. (Courtesy of the GEO collaboration.)

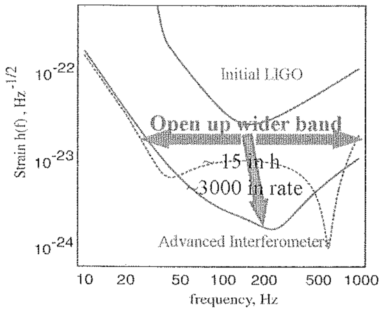

Fig. 9.34 The planned sensitivity of Advanced LIGO compared to initial LIGO. A wideband and a narrow-band configuration are shown. (Courtesy of the LIGO collaboration.)

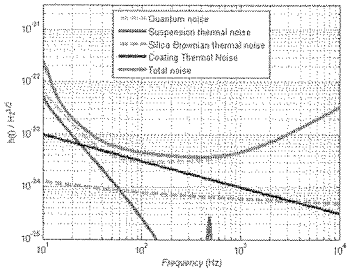

Fig. 9.35 The main noise contributions in a possible Advanced LIGO configuration. (Courtesy of the LIGO collaboration.)

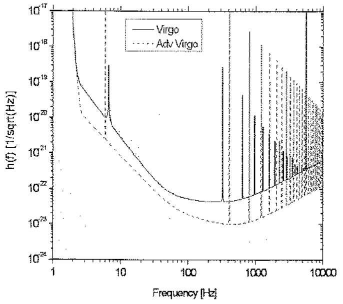

Fig. 9.36 A possible sensitivity curve of Advanced Virgo, compared to the initial Virgo. (Courtesy of the VIRGO collaboration.)

9.5.2 Advanced interferometers

Ground-based detectors

For the LIGO and VIRGO interferometers there is a well-defined plan for upgrades which should lead, in a few years, to second-generation detectors with much better sensitivities, Advanced LIGO (to which will contribute also GEO600 and the Australian consortium ACIGA) and Advanced VIRGO. GEO600 should evolve into a tunable narrow-band detector in the high-frequency region (GEO-HF), and in a facility for testing technologies for future interferometers. A cryogenic detector, LCGT, is under study in Japan, and there are plans for an interferometer in Australia, AIGO. Examples of planned sensitivities are shown in Figs. 9.34–9.36.

While a number of details might still change, the baseline for the main improvements that are planned is the following.

- An increase in the input laser power from the present value of order 10–20 W up to 100–200 W. After power recycling, this would lead to a laser power in the Fabry–Perot arm cavities of order 1 MW. This has the effect of reducing the shot noise, improving the sensitivity in the high-frequency region. Such a huge power will however induce thermal lensing in the test mass optics, due to absorption in the substrate and coatings, and compensation effects will be added.
- As discussed in Section 9.4.2, the increased laser power will produce a larger radiation pressure noise, up to the point that this becomes a dominant noise at low frequency. This is compensated increasing the mirror masses, up to about 40 kg.
- LIGO will introduce much better seismic isolation, improving the sensitivity at low frequencies and bringing the "seismic wall" from 40 Hz down to about 10 Hz. VIRGO already has a seismic isolation appropriate for an advanced interferometer.
- The test-mass suspensions, presently made of steel wires, will be replaced by silica (which has lower losses), fused to the mirror with silicate bonding to create a single monolithic object, thereby reducing suspension thermal noise. This technique has already been developed in GEO600. Further improvement can be obtained shaping the suspension fibers in the form of a ribbon. The resulting suspension thermal noise will be lower than the radiation pressure noise (in broad-band observation mode, see below), and comparable to the Newtonian background at 10 Hz.
- New mirror coatings, with lower thermal noise and lower losses (e.g. thanks to the insertion of dopants) are investigated.

The basic optical configuration is still a power-recycled interferometer with Fabry–Perot cavities in the arms. To this configuration is added *signal recycling*. This consists of adding a new mirror, the signal-recycling mirror, at the output port of the interferometer, i.e. between the beam-splitter and the photodetectors in Fig. 9.25. As in our discussion of the power recycling cavity, the addition of this mirror creates a new cavity, the signal-recycling cavity, composed by the "effective interferometer mirror" and the signal-recycling mirror.

Recall from Section 9.2.2 that a GW of frequency $\omega_{\rm gw}$ generates in the interferometer sidebands at $\omega_{\rm L} \pm \omega_{\rm gw}$. If the signal-recycling cavity is tuned in resonance with a sideband corresponding to some given value of $\omega_{\rm gw}$, the sensitivity of the interferometer for this GW frequency is enhanced, at the cost of the bandwidth. This enhancement depends on the finesse of the signal-recycling cavity. If the signal-recycling cavity is tuned to anti-resonance, the sidebands are extracted and the bandwidth of the detector is increased, with respect to the case where no signal-recycling cavity is present. This technique is know as *resonant sideband extraction*. As a result, with tiny adjustments of the position of the signal-recycling mirror, of order of fractions of $\lambda_{\rm L}$, we can either tune the interferometer to some specific source or increase the bandwidth. These two options are illustrated in Fig. 9.34. The signal-recycling technique is already implemented in GEO600, although without Fabry–Perot cavities in the arms.

Thanks to these and to other improvements, an advanced interferometer in wideband mode will be limited, over a bandwidth from about 10 Hz to a few kHz, mostly by the optical read-out noise, as we see from Fig. 9.35, and therefore by the quantum limit. In the signal-recycling configuration it is however possible to perform quantum non-demolition measurements, hence going beyond the standard quantum limit, with a simple modification of the input–output optics, see Fig. 9.37 and the papers by Buonanno and Chen in the Further Reading section.

With the strain sensitivity of an advanced interferometer, the perspective for detection and for opening the field of GW astrophysics are quite good. A detailed discussion of the sources and their strength will be the subject of Vol. 2. Here we observe that the sight distance to NS-NS binaries becomes

$$d_{\rm NS-NS} = O(300)\,{\rm Mpc}\,. \tag{9.248}$$

At this distance, the expected rate is between $O(10)$ per year and $O(100)$ per year. For BH-BH with masses $10M_{\odot}$, the sight distance becomes

$$d_{\rm BH-BH} = O(1.5)\,{\rm Gpc}\,, \tag{9.249}$$

and expected rates are between one signal per year and $O(500)$ per year.[40] For BH-NS binaries,

$$d_{\rm BH-NS} = O(750)\,{\rm Mpc}\,, \tag{9.250}$$

with an expected rate between one signal per year and $O(30)$ per year.

Looking further ahead, there are ideas for "third generation" interferometers. Among the features that are being considered, is the possibility of building an underground detector. As discussed in Section 9.4.4 (compare with Note 34 on page 524) the micro-seismic noise is mostly propagated through surface waves, so underground it is sensibly reduced, which also results in a reduction of the Newtonian noise induced by the

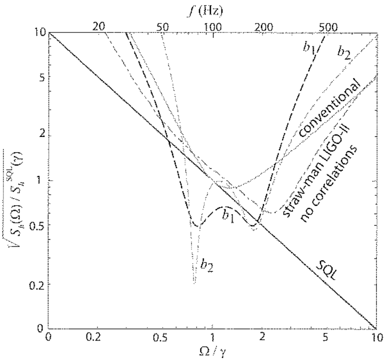

Fig. 9.37 Plot of $\sqrt{S_n(\Omega)/S_n^{\rm SQL}(\gamma)}$ (where $\Omega = 2\pi f$ and $\gamma = 2\pi f_{\rm pole}$) as a function of Ω/γ, for different optical configurations. Reprinted with permission from Buonanno and Chen, *Class. Quantum Grav.* **18** L95 (2001b).

---

[40] A major source of theoretical uncertainty is related to the fact that the potential progenitors of a BH-BH system can go through a phase of common envelope evolution, that can lead to the merging of the progenitor stars rather than to the formation of a BH-BH binary. See Belczynski, Taam, Kalogera, Rasio and Bulik (2006) for a discussion of these rates and of their theoretical uncertainties.

micro-seismic motion. Another third-generation feature could be the use of cryogeny. A Japanese collaboration, building on the experience gained with TAMA, has proposed the realization of the LCGT detector, made of two independent underground interferometers in the same vacuum system, with 3 kms arms and cryogenic mirrors, cooled at 20 K, to be located at Kamioka, an old mine transformed in an underground physics laboratory. This site is about 1000 m below the top of a mountain, and provides a very stable seismic and temperature environment. A prototype, CLIO, has already been installed and is under development.

Interferometers in space

The region below about 10 Hz is unaccessible to ground-based interferometers, because of the wall due to seismic and Newtonian noise. Still, we will see in Vol. 2 that the mHz region is potentially very rich in GW sources, including particularly fascinating objects such as supermassive black holes. The only way to detect them is to go in space, where the seismic noise is absent. One such project is LISA. The LISA mission is a collaboration between the European Space Agency (ESA) and NASA. The concept of the LISA mission is quite impressive. It consists of three spacecrafts, separated by 5 million kms, in a equilateral triangle configuration, orbiting the Sun. The center of the triangle should be at a distance of about 50 million kms (i.e. about 20° degrees along the orbit) behind the Earth. The size of the arms is chosen to optimize the sensitivity for GWs in the 10 mHz region, and in general LISA would be sensitive to GW frequencies in the range 0.1 mHz–0.1 Hz.

For a detailed description of the mission concept we refer the reader to the Further Reading section. Here we briefly mention some aspects of this remarkable experiment.

- Inside each spacecraft there will be two test masses (one for each arm), freely floating. The spacecraft is kept centered on the test masses using a *drag free* technique, in which the position of the masses is sensed, and the spacecraft adjusts its position with respect to them, using micro-thrusters. The thrusts necessary to maintain drag-free operation are extremely small, less than 100 μN, and the required recoil is obtained emitting in space just a handful of fast ions. This compensates for external influences such as solar winds, micro-meteorites, etc. that in the long term would sensibly alter the nominal position of the spacecraft. The LISA Pathfinder is a ESA mission to demonstrate the drag-free control technique at the required accuracy.
- The free masses exchange among them laser signals. Over a distance of 5 million kms, reflection is impossible because of power losses due to diffraction; after a travel of 5 million kms, the laser beam is spread over a surface of radius 20 kms. So LISA uses a laser transponding scheme in which the incoming laser light is sensed, and another laser is phase-locked to it and sends back another beam.

- LISA has unequal arms, with arm-lengths known to ±20 m from the measurement of the round-trip time. Then, contrary to what happens in a Michelson interferometer with equal arms, laser frequency fluctuations do not cancel out when taking the difference between two arms. For this reason, the LISA concept uses time-delay interferometry, in which the outputs of the two arms are recombined with a time delay that takes care of the arm difference. In the process, laser frequency noise is canceled (while the signal from GWs with frequencies in the mHz region is unaffected).
- After minimizing spurious forces on test masses, the other most important issue is the need to keep the temperature distribution in the spacecraft as constant as possible, since the mass displacements due local temperature fluctuations would induce changes in the Newtonian gravitational forces on the test mass, as well as accelerations of the test masses due to thermal radiation pressure.

Clearly, LISA would be an extremely impressive instrument and its scientific achievements could be truly spectacular.

A number of other space missions are currently discussed, such as DECIGO, a Japanese space project with arm-lengths shorter than LISA, to bridge the gap between LISA and the ground-based detectors; and ASTROD, a Chinese space project with arm-lengths longer than LISA which, among other relativity experiments, would extend the search for GWs to lower frequencies. Follows-up to the LISA mission, such as the Big-Bang Observer (BBO), are also being investigated.

Further reading

- For a lively discussion of the history of gravitational-wave research, as well as the development of GW interferometers, see the popular book Thorne (1994). See also the review Thorne (1987).
- A textbook devoted to the interferometric detection of GWs is Saulson (1994). For reviews, see also Giazotto (1989), Drever (1991), and Ju, Blair and Zhao (2000). A large bibliography on GW interferometers can be found in the review by Rowan and Hough (2000).
- A detailed discussion of the optics of GW interferometers is the "VIRGO Physics Book, Optics and related Topic", available at http://wwwcascina.virgo.infn.it/vpb/. The effect of scattered light in interferometers is discussed in Vinet, Visson and Braccini (1996) and Vinet *et al.* (1997). Mesa beams are proposed in Bondarescu and Thorne (2006).
- Computations of the sensitivities to GWs of Fabry–Perot cavities in various configurations can be found in Vinet, Meers, Man and Brillet (1988) and Meers (1988, 1989).
- A pedagogical discussion of lock-in detection is given in Black and Gutenkunst (2003). A nice discussion of null instrument is given in Saulson (1994), Chapter 10. For a discussion of Pound–Drever–Hall locking see Saulson (1994), Section 12.5, and Black (2001). A discussion of the global control of the VIRGO detector can be found in Arnoud *et al.* (2005). For resonant sideband extraction see Mizuno *et al.* (1993).
- Shot noise in modulated interferometers is discussed in Niebauer, Schilling, Danzmann, Rüdiger and Winkler (1991) and Bondu (2003). Radiation pressure is discussed in Edelstein, Hough, Pugh and Martin (1978) and Caves (1980, 1981).

- For quantum non-demolition measurements see Caves, Thorne, Drever, Sandberg and Zimmermann (1980) and Braginsky and Kalili (1992). For application to advanced interferometers see Kimble, Levin, Matsko, Thorne and Vyatchanin (2000) and Buonanno and Chen (2001a, 2001b, 2002). For a review of quantum noise in GW interferometers see Corbitt and Mavalvala (2004).
- The effect of seismic noise in GW interferometers is discussed in Saulson (1994), Chapter 8. Newtonian noise are studied in Saulson (1984) and Beccaria *et al.* (1998). Our discussion of thermal noise followed the internal VIRGO note Flaminio *et al.* (2005), where calculations of the various thermal noise are performed in detail. Thermo-elastic noise is discussed in Braginsky and Vyatchanin (2003).
- Updated information on the existing GW interferometers, as well as technical documents, PhD theses, etc. can be found at
  http://www.ligo.caltech.edu/ (LIGO)
  http://wwwcascina.virgo.infn.it/ (VIRGO)
  http://www.geo600.uni-hannover.de/ (GEO600)
  http://tamago.mtk.nao.ac.jp/ (TAMA)
- A detailed description of the LISA mission can be found in the LISA Pre-Phase A Report (1998). See also the reviews Bender (2001), Danzmann and Rüdiger (2003), and the web site http://lisa.jpl.nasa.gov.
- For lack of space, we have not discussed experiments searching for GWs using the Doppler tracking of spacecraft. For a recent review, see Armstrong (2006).

Bibliography

Abbott, B. *et al.* [LIGO Science Community, LSC] (2004a). *Phys. Rev. D* **69**, 082004.
Abbott, B. *et al.* [LSC] (2004b). *Phys. Rev. D* **69**, 102001.
Abbott, B. *et al.* [LSC] (2004c). *Phys. Rev. D* **69**, 122001.
Abbott, B. *et al.* [LSC] (2004d). *Phys. Rev. D* **69**, 122004.
Abbott B. *et al.* [LSC] (2005a). *Phys. Rev. D* **72**, 082001.
Abbott, B. *et al.* [LSC] (2005b). *Phys. Rev. Lett.* **94** 181103.
Abbott, B. *et al.* [LSC] (2005c). *Phys. Rev. Lett.* **95**, 221101.
Abramowitz, M. and I. A. Stegun (1972). *Handbook of Mathematical Functions*, Dover, New York.
Aguiar, O. D. *et al.* (2004). *Class. Quant. Grav.* **21**, S457.
Allen, Z. A. *et al.* [IGEC] (2000). *Phys. Rev. Lett.* **85**, 5046 .
Allen, B. and J. D. Romano (1999). *Phys. Rev. D* **59**, 102001.
Anderson, W. G. and R. Balasubramanian (1999). *Phys. Rev. D* **60**, 102001.
Anderson, W. G., P. R. Brady, J. D. E. Creighton and E. E. Flanagan (2001). *Phys. Rev. D* **63**, 042003.
de Andrade, V. C., L. Blanchet and G. Faye (2001). *Class. Quant. Grav.* **18**, 753.
Apostolatos, T. A., C. Cutler, G. J. Sussman and K. S. Thorne (1994). *Phys. Rev. D* **49**, 6274.
Arnaud, N. *et al.* (2005). *Nucl. Instr. Meth. A* **550**, 467.
Arnowitt, R., S. Deser and C. W. Misner (1961). *Phys. Rev.* **121**, 1556.
Arkani-Hamed, N., H. Georgi and M. D. Schwartz (2003). *Ann. Phys.* **305**, 96.
Arkani-Hamed, N., H. C. Cheng, M. A. Luty and S. Mukohyama (2004). *JHEP* **0405**, 074.
Armstrong, J. W. (2006). *Living Rev. Relativity* **9**, 1. Online article http://www.livingreviews.org/lrr-2006-1.
Arun, K. G., L. Blanchet, B. R. Iyer and M. S. Qusailah (2004). *Class. Quant. Grav.* **21**, 3771. [Erratum-ibid. **22**, (2005) 3115].
Ashby, N. and J. Dreitlein (1975). *Phys. Rev. D* **12**, 336.
Astone, P., *et al.* [ROG] (1997b). *Astroparticle Phys.* **7**, 231.
Astone, P., *et al.* [ROG] (2002). *Phys. Rev. D* **65**, 022001.
Astone, P., *et al.* [IGEC] (2003a). *Phys. Rev. D* **68**, 022001
Astone, P., *et al.* [IGEC-2] (2007). arXiv:0705.0688[gr-qc].
Astone, P., *et al.* [ROG] (2003b). *Phys. Rev. Lett.* **91**, 111101.
Backer, D. C. and R. W. Hellings (1986). *Ann. Rev. Astron. Astrophys.*